Project 09-815

A New 2D-Transport, 1D-Diffusion Approximation of the Boltzmann Transport Equation

Integrated University Programs

Dr. Edward W. Larsen
University of Michigan

In collaboration with:
Argonne National Laboratory

James Sterbentz, Technical POC

National Nuclear Security Administration

Final Report

DOE Contract Number: DE-AC07-05ID14517

Project Number: NEUP 09-815

A New 2D-Transport, 1D-Diffusion Approximation of the Boltzmann Transport Equation

Edward W. Larsen
Department of Nuclear Engineering and Radiological Sciences
University of Michigan
Ann Arbor, Michigan 48109-2104 USA
edlarsen@umich.edu

(a) ABSTRACT

The work performed in this project consisted of the derivation, implementation, and testing of a new, computationally advantageous approximation to the 3D Boltzmann transport equation. The solution of the Boltzmann equation is the neutron flux in nuclear reactor cores and shields, but solving this equation is difficult and costly. The new "2D/1D" approximation takes advantage of a special geometric feature of typical 3D reactors to approximate the neutron transport physics in a specific (axial) direction, but not in the other two (radial) directions. The resulting equation is much less expensive to solve computationally, and its solutions are expected to be sufficiently accurate for many practical problems. In this project we formulated the new equation, discretized it using standard methods, developed a stable iteration scheme for solving the equation, implemented the new numerical scheme in the MPACT code, and tested the method on several realistic problems. All the hoped-for features of this new approximation were seen. For large, difficult problems, the resulting 2D/1D solution is highly accurate, and is calculated about 100 times faster than a 3D discrete ordinates simulation.

(b) OBJECTIVES AND ACCOMPLISHMENTS

The overall objective of this project was to develop, implement, and test a mathematically consistent and implementationally superior version of the "2D/1D" method in the DeCART code, written about 10 years ago as an INERI project involving Argonne National Laboratory (ANL) and the Korea Atomic Energy Research Institute (KAERI). The original 2D/1D method in DeCART simulated 3D transport problems in typical light water reactors (LWRs) by using a clever approximation based on a special feature of the geometry of LWRs: the spatial dependence of the cross sections in LWRs is very strong in the *radial* directions x and y, but typically is weak in the *axial* direction z. DeCART took advantage of this by means of a numerical method that utilized (i) the correct (but expensive) transport physics in the radial directions, and (ii) an approximate (but simpler and less expensive) diffusion solver in the axial direction. The resulting code worked well for problems having an optically thick axial grid ($\Delta z > 6$ inches).

At the time this NEUP project was initiated, the CASL project (centered at Oak Ridge National Laboratory) had begun, and the CASL staff were using an early version of DeCART (based here at the University of Michigan) to perform certain 3D reactor core simulations. It was discovered that this version of DeCART failed

to converge for problems with small axial grids. Because of this, it was not possible to refine the DeCART spatial grids axially to obtain detailed solutions. Moreover, because the numerical method in DeCART used one type of transport physics for the radial spatial variables and an approximate type of transport physics (diffusion) for the axial variable, it was not evident *what* the DeCART solution would converge to even if the code did iteratively converge.

The objective of this project was to develop a new, mathematically consistent 2D/1D methodology in which these deficiencies (lack of iterative convergence for small Δz, lack of a theoretical understanding of what the solution should converge to for small spatial grids) were overcome. Overall, we proposed that the 2D/1D methodology should be modified and put on a sound mathematical footing, that mathematically consistent discretization and iteration strategies be developed, and that the resulting method should be implemented and tested.

The central idea that allowed us to accomplish this task was the realization that the new 2D/1D computational method should be derived from a fundamentally new "2D/1D" approximation to the 3D Boltzmann transport equation. This new 3D equation should be intermediate in accuracy between 3D transport and 3D diffusion. Specifically, it should preserve transport physics in the radial directions x and y, and use diffusion physics in the axial direction z. If this equation were formulated, and if it could be shown to have a unique solution, then in principle both of the major objections to the 2D/1D method in DeCART could be overcome. (The new 2D/1D equation could be consistently discretized, using standard methods, and iteration methods to solve the discrete equations could be studied by a standard Fourier analysis. In principle, the Fourier analysis would predict which iteration methods would be stable, and which would not be stable. Also, in the limit of small spatial grids, the numerical solution would converge to the analytic solution of the 2D/1D equation.)

All this, including the implementation and testing of the new method, and the publication of preliminary results, has been accomplished. The list of specific objectives, with a discussion of the effort performed and the accomplishments achieved, is given next.

1. ITERATION METHODOLOGIES

Very early in this work, we realized that the Coarse Mesh Finite Difference (CMFD) iteration method was being used in DeCART, and we also knew that CMFD had been used with success in other reactor physics codes during the past 20 years. CMFD had been systematically linearized and Fourier-analyzed, to theoretically assess its range of stability, but this method had not been shown

to be related to another method in use, Diffusion Synthetic Acceleration (DSA). In our theoretical investigation of CMFD, we discovered that when this method is linearized, it becomes algebraically equivalent to a "coarse mesh" version of DSA. This clarified the (surprising) theoretical relationship between CMFD and DSA, and it made it possible for us to think of using these methods somewhat interchangeably, i.e. we could use one where it was advantageous, and the other where it was advantageous, and we knew that the methods would perform in the same way. (Previously, most researchers were unaware that DSA and CMFD were related in any way.)

We also developed and tested (in 1D) a new acceleration method for domain-decomposed transport problems. The idea here was to design a CMFD-based method in which individual computer processors could be assigned an individual assembly of a reactor, and the acceleration method would take the results from the individual (coarse grid) assemblies and efficiently produce a global fine grid solution. Our intent was to use this method for the eventual implementation of the new 2D/1D method.

These two tasks were successfully completed, and they led to two conference papers presented at the 2012 PHYSOR conference [1, 2].

2. THE 2D/1D EQUATION: THEORY

Concurrent with the work on iteration methods described above, we also worked on the definition and theoretical basis of the new 2D/1D equation. The detailed derivation of this equation is given in an attached conference paper [3]. We will just state the results here.

The 3D Boltzmann transport equation for monoenergetic, isotropically-scattering problems can be written as

$$\boxed{\sqrt{1-\mu^2}\left(\cos\omega\frac{\partial\psi}{\partial x}+\sin\omega\frac{\partial\psi}{\partial y}\right)+\mu\frac{\partial\psi}{\partial z}+\Sigma_t\psi=\frac{1}{4\pi}\Big(\Sigma_s\phi+Q\Big)}\,, \qquad (1)$$

where the notation is standard:

$$\psi(x,y,z,\mu,\omega) = \text{ angular flux }, \qquad (2)$$

$$\phi(x,y,z)=\int_{-1}^{1}\int_{0}^{2\pi}\psi(x,y,z,\mu',\omega')d\mu'd\omega' = \text{ scalar flux }. \qquad (3)$$

In the problems under consideration, the cross sections are assumed to be strong functions of the radial variables x and y, and weak functions of the axial variable z. The solution ψ is also assumed to have the same properties.

In the 2D/1D approximation, the (weak) axial derivative in Eq. (1) is replaced using a 1D diffusion approximation, resulting in:

$$\boxed{\sqrt{1-\mu^2}\left(\cos\omega\frac{\partial\psi}{\partial x}+\sin\omega\frac{\partial\psi}{\partial y}\right)-\frac{\partial}{\partial z}\frac{D}{4\pi}\frac{\partial\phi}{\partial z}+\Sigma_t\psi=\frac{1}{4\pi}\Big(\Sigma_s\phi+Q\Big)}\ . \quad (4)$$

This is the new "2D/1D" equation on which our work is based. Again, the derivation of Eq. (4) and its boundary conditions is discussed in greater detail in [3].

In the standard 3D diffusion equation, *all* the derivatives in Eq. (1) are replaced using their 1D diffusion approximation. The resulting equation is integrated over μ and ω, yielding:

$$\boxed{-\frac{\partial}{\partial x}D\frac{\partial\phi}{\partial x}-\frac{\partial}{\partial y}D\frac{\partial\phi}{\partial y}-\frac{\partial}{\partial z}D\frac{\partial\phi}{\partial z}+\Sigma_t\psi=\Sigma_s\phi+Q}\ . \quad (5)$$

In 3D problems having no z-dependence, the 2D/1D Eq. (4) and the Boltzmann Eq. (1) become identical. (This is not true for the 3D diffusion equation.) For this reason, it is expected that the solution of Eq. (4), if it exists, should be intermediate in both accuracy and cost between the 3D Boltzmann Eq. (1) and the 3D diffusion Eq. (5).

The proposed 2D/1D Eq. (4) does not have a standard mathematical form, and we have not been able to reformulate this equation as an integral equation for which an existence proof could be easily derived. Consequently, we have been unable to mathematically prove that Eq. (4) with suitable boundary conditions has a solution. We can, however, prove that if a solution of Eq. (4) exists, it is unique. In all our subsequent work, we have *assumed* that a (unique) solution of the 2D/1D equation exists; nothing in our experience suggests that this assumption is incorrect.

After formulating the 2D/1D equation and boundary conditions, we began the process of systematically discretizing this equation. First, we discretized the new (diffusion) axial derivative term, using a standard 1D diffusion discretization in which the unknowns are the cell-averaged flux. The resulting discrete-in-z equation is a 2D transport equation defined on each axial "slice," coupled in a simple way with the directly-above and directly-below slices. These 2D equations were then discretized in x, y, μ, and ω using the standard 2D Method of Characteristics (MOC).

Next, we began formulating and studying (by Fourier analysis) iteration methods for solving the axially-discrete equations. We first considered a method

that was similar to that used in the original DeCART, and we showed that it was unstable for small Δz (in agreement with observations). However, we also showed that a straightforward relaxation method was capable of stabilizing the scheme for arbitrarily small Δz. We also considered more elaborate (and faster-converging) schemes using CMFD, and we showed theoretically that these methods would rapidly converge for large Δz, but would be unstable for small Δz. However, a straightforward relaxation again stabilized the CMFD method, producing faster convergence than the relaxed method without CMFD.

The basic theoretical work had thus been done: the 2D/1D equation had been (i) formulated, (ii) shown to have desirable accuracy properties, and (iii) systematically discretized; and (iv) theoretically stable, efficient iteration schemes had been developed for solving the discrete equations. (Again, see [3] for details.) It remained to implement and test the new method.

3. THE 2D/1D EQUATION: IMPLEMENTATION AND TESTING

Partly because of the difficulties encountered with DeCART, the CASL research group here at UM decided to build a new reactor physics code to (eventually) replace DeCART for CASL applications. The new code would employ the new 2D/1D method – which was theoretically shown to be accurate, stable, and to converge with sufficient efficiency. Graduate student Blake Kelley, who did much of the 2D/1D work, was part of the team that built new code (called MPACT). Blake spent considerable time working on basic features of the code that had to be in place before his 2D/1D method could be implemented. Finally, in January 2013, Blake began implementing 2D/1D. His implementation was able to solve simple problems by the end of February 2013, and in May 2013 it was solving some standard 3D benchmark problems.

The numerical results seen from the new MPACT code are fully consistent with the pre-existing theories. The iteration scheme encoded in MPACT converges just as the theory predicts, and the 2D/1D solutions generated by MPACT converge for all choice of spatial grids. These 2D/1D solutions are surprisingly accurate for many 3D problems. (As expected, the weaker the z-dependence, the more accurate is the 2D/1D solution.) For complex 3D problems, the cost of solving the 2D/1D equations is about a factor of 100 less than the cost of solving 3D discrete ordinates calculations. Early numerical results from February 2013 are described in the attached conference paper [4].

Finally, we wish to emphasize that the work performed in this NEUP project has been extremely important for the neutronics portion of the CASL

project. The new 2D/1D method was not implemented in a small, limited test code; it was implemented in MPACT – a new, 3D, multigroup code capable of solving realistic problems of interest to CASL. The encoded new 2D/1D method will be used by CASL staff at several universities, national laboratories, and commercial vendors for much of the 3D neutronics CASL simulations. (This is discussed in further detail in Section (d) below.)

(c) PUBLICATIONS

Thus far, five publications have been generated by this work. The first two were full-length conference papers (and presentations) given at the 2012 American Nuclear Society PHYSOR conference in Knoxville, TN. These papers were concerned with the first "iteration" part of the project. The third and fourth papers were connected full-length conference papers (and presentations) given at the 2013 American Nuclear Society Mathematics and Computation Topical Conference in Sun Valley, Idaho. These papers both dealt with the theory and implementation of the new 2D/1D equation. The fifth paper is an expanded version of the first paper on the relationship between DSA and CMFD; it was recently submitted to the journal *Nuclear Science and Engineering*. During the next year, after Blake completes his PhD dissertation, we plan to publish several other journal articles on the new 2D/1D method.

[1] E.W. Larsen and B.W. Kelley, "CMFD and Coarse-Mesh DSA," *Proc. PHYSOR 2012, Advances in Reactor Physics Linking Research, Industry, and Education*, Knoxville, Tennessee, April 15-20, 2012, on CD-ROM, American Nuclear Society, LaGrange Park, IL (2012).

[2] B.W. Kelley and E.W. Larsen, "CMFD Acceleration of Spatial Domain-Decomposed Neutron Transport Problems," *Proc. PHYSOR 2012, Advances in Reactor Physics Linking Research, Industry, and Education*, Knoxville, Tennessee, April 15-20, 2012, on CD-ROM, American Nuclear Society, LaGrange Park, IL (2012).

[3] B.W. Kelley and E.W. Larsen, "2D/1D Approximations to the 3D Neutron Transport Equation. I: Theory," *Proc. Int. Conf. on Math. & Comp. Methods Applied to Nucl. Sci. & Eng.*, Sun Valley, Idaho, May 5-9, 2013, on CD-ROM, American Nuclear Society, Lagrange Park, IL (2013).

[4] W. Kelley, B. Collins, and E.W. Larsen, "2D/1D Approximations to the 3D Neutron Transport Equation. I: Theory," *Proc. Int. Conf. on Math. & Comp.*

Methods Applied to Nucl. Sci. & Eng., Sun Valley, Idaho, May 5-9, 2013, on CD-ROM, American Nuclear Society, Lagrange Park, IL (2013).

[5] E.W. Larsen and B.W. Kelley, "The Relationship Between the CMFD and the Coarse-Mesh DSA Methods," *Nucl. Sci. Eng.*, submitted.

(d) OTHER RELATED INFORMATION

The NEUP project that supported this work ended in December 2012, but because of the work's importance to CASL, it has been continued, and it will be continued beyond the filing of this report. Currently, graduate student Blake Kelley is implementing several theoretically-improved variants of the "basic" 2D/1D method now in MPACT. We expect this work to continue for several more months, and for Blake to defend his PhD thesis during the latter part of the fall semester, 2013. After that, Blake is expected to stay on at UM as a postdoc, to implement several other refinements in the 2D/1D method that should significantly enhance the method, but that go beyond the work necessary for his PhD dissertation.

In recent years, KAERI and ANL have generated a new version of DeCART, and currently, ANL is writing a new PROTEUS code. Both codes use the 2D/1D concept, but with certain refinements. For example, the new DeCART uses a Simplified P3 approximation for the axial derivative, rather than P1 (diffusion). Also, the codes use a form of CMFD iteration that is reported to be more stable than the original DeCART. However, the existing documentation of all this work is very sketchy. Based on what is available, it is not possible to tell whether (i) the new CMFD-based iteration scheme is theoretically stable, or (ii) the solution of the discrete equations has a proper limit as the spatial grid is refined.

In conclusion, we believe that the new 2D/1D method developed in this project represents an advantageous and mathematically consistent way to simulate realistic 3D light water reactors. Also, we anticipate that a significant amount of future research – aimed at refining the "diffusion" approximation to the axial derivative – will be undertaken.

(e) APPENDIX

In the remainder of this report, we include copies of the five publications that have thus far arisen from this NEUP project.

PHYSOR 2012 Advances in Reactor Physics Linking Research, Industry, and Education
Knoxville, Tennessee, USA, April 15-20, 2012, on CD-ROM, American Nuclear Society, LaGrange Park, IL (2012)

CMFD AND COARSE-MESH DSA

Edward W. Larsen and Blake W. Kelley
Department of Nuclear Engineering and Radiological Sciences
University of Michigan
Ann Arbor, Michigan 48109-2104 USA
edlarsen@umich.edu; kelleybl@umich.edu

ABSTRACT

The Coarse Mesh Finite Difference (CMFD) and Diffusion Synthetic Acceleration (DSA) methods are two widely-used, independently-developed acceleration methods for iteratively solving deterministic particle transport simulations. In this paper we show that these methods are related in the following way: if the standard notion of DSA as a "fine mesh" method is generalized to that of a coarse mesh method, then *the linearized form of CMFD is algebraically equivalent to a coarse mesh form of DSA*. Also, we demonstrate theoretically (via Fourier analysis) and computationally that CMFD and coarse mesh DSA have nearly the same convergence properties.

Key Words: Deterministic Transport, Iteration Methods, Acceleration Methods

1. INTRODUCTION

For many years, deterministic neutral particle transport codes have used the Source Iteration (SI) method with an acceleration scheme to iteratively converge the numerical solution [1]. Early acceleration methods included Fine and Coarse-Mesh Rebalance; these were later superseded by various forms of Diffusion Synthetic Acceleration (DSA) [1–5]. Still later, the Coarse Mesh Finite Difference (CMFD) method was independently developed [6–9]. In this paper, we show that the DSA and CMFD methods have a surprisingly close theoretical relationship.

Outwardly, the DSA and CMFD methods are similar. In both, a single iteration consists of a "high order" transport sweep followed by a "low-order" diffusion calculation. However, the diffusion calculations in the two methods are fundamentally different. DSA is usually implemented as a "fine grid" method (the spatial grids for the transport and diffusion calculations are the same), whereas CMFD is usually implemented as a "coarse grid" method (the spatial grid for the diffusion equation is coarser than the spatial grid for the transport equation). Also, the DSA diffusion calculation is linear and the resulting solution is an additive correction to the most recent fine-grid scalar flux estimate; the CMFD diffusion calculation is nonlinear and the resulting solution is a coarse-grid scalar flux estimate.

In 2003, Cho and Park showed by a linearized Fourier analysis and numerical experiments that the CMFD method converges rapidly when the coarse cells are less than one mean free path thick; but as the coarse cells become thicker, the method quickly degrades in performance and then diverges [8]. Cho and Park commented that this qualitatively describes the convergence properties of an "inconsistent" DSA method, in which (i) the transport and diffusion grids are the same, and (ii) a standard discretization of the diffusion equation, not chosen to be "consistent" with the transport discretization, is used [1, 4].

In this paper we make use of these various ideas and show that the DSA and CMFD methods have the following relationship:

1. The linearized form of CMFD is algebraically equivalent to a "coarse mesh DSA" (or CMDSA) method.
2. A Fourier analysis accurately predicts the convergence properties of the CMDSA method. (This extends the previous work by Cho and Park [8].)
3. In numerical simulations, the (linear) CMDSA and (nonlinear) CMFD methods have nearly the same convergence properties. Thus, the Fourier analysis results accurately describe both the linear CMDSA and the nonlinear CMFD methods.

Therefore, rather than being two unrelated methods, DSA and CMFD have close theoretical ties. Of course, the methods have differences. Because of its nonlinearities, CMFD is easier than DSA to apply to the outer iterations of eigenvalue problems (an advantage); but CMFD can fail to converge if any angular flux iterate becomes negative (a disadvantage). However, for problems on which both methods can be successfully used, our theory predicts – and our numerical results confirm – that the two methods have nearly the same convergence properties.

The remainder of this paper is organized as follows. In Section II a 1-D S_N fixed-source problem is described, and for this problem the (linear) CMDSA and (nonlinear) CMFD methods are formulated. In Sec. III the CMFD method is linearized, and the resulting "linearized CMFD" (LCMFD) equations are shown to be algebraically equivalent to the CMDSA equations. Section IV presents the results of numerical experiments showing that the (linear) CMDSA and (nonlinear) CMFD methods have nearly the same convergence properties. Section V concludes this paper with a brief discussion.

2. THE CMFD AND CMDSA METHODS

Here we describe the CMFD and CMDSA methods for a planar geometry fixed-source problem on the system $0 \leq x \leq X$:

$$\mu \frac{\partial \psi}{\partial x}(x,\mu) + \sigma_t(x)\psi(x,\mu) = \frac{\sigma_s(x)}{2}\int_{-1}^{1} \psi(x,\mu')d\mu' + \frac{q(x)}{2} \ , \tag{1a}$$

$$\psi(0,\mu) = \psi^b(\mu) \ , \quad 0 < \mu \leq 1 \ , \tag{1b}$$

$$\psi(X,\mu) = \psi^b(\mu) \ , \quad -1 \leq \mu < 0 \ . \tag{1c}$$

Using the familiar discrete ordinates approximation in angle and an arbitrary weighted diamond approximation in space, we discretize Eqs. (1) as follows:

$$\frac{\mu_n}{h_j}\left(\psi_{n,j+1/2} - \psi_{n,j-1/2}\right) + \sigma_{t,j}\psi_{n,j} = \frac{\sigma_{s,j}}{2}\sum_{m=1}^{N}\psi_{m,j}w_m + \frac{q_j}{2} \ , \tag{2a}$$

$$\psi_{n,j} = \left(\frac{1+\alpha_{n,j}}{2}\right)\psi_{n,j+1/2} + \left(\frac{1-\alpha_{n,j}}{2}\right)\psi_{n,j-1/2} \ , \tag{2b}$$

$$\psi_{n,1/2} = \psi_n^b \ , \quad \mu_n > 0 \ , \tag{2c}$$

$$\psi_{n,J+1/2} = \psi_n^b \ , \quad \mu_n < 0 \ . \tag{2d}$$

The notation in Eqs. (1) and (2) is standard. The subscript j, running from $1 \leq j \leq J$, denotes the (fine) spatial cell, which has width h_j, cross sections $\sigma_{t,j}$ and $\sigma_{s,j}$, and constant internal source q_j. The subscript n, running from $1 \leq n \leq N$, denotes the direction cosine of flight. The constants $\alpha_{n,j}$ determine the specific spatial discretization method, e.g.

$$\alpha_{n,j} = \begin{cases} 0 & , \quad \text{Diamond Difference} , \\ \frac{1+e^{-\sigma_{t,j}h_j/\mu_n}}{1-e^{-\sigma_{t,j}h_j/\mu_n}} - \frac{2\mu_n}{\sigma_{t,j}h_j} & , \quad \text{Step Characteristic} . \end{cases} \tag{3}$$

The CMFD and CMDSA methods begin each iteration with a standard fine-mesh transport sweep. At the beginning of the ℓ^{th} iteration, the fine-mesh cell-averaged scalar fluxes

$$\phi_{0,j}^{(\ell)} = \sum_{n=1}^{N} \psi_{n,j}^{(\ell)} w_n \ , \quad 1 \leq j \leq J \tag{4}$$

are assumed known, either from the previous iteration or from the initial guess if $\ell = 0$. Then the following version of Eqs. (2):

$$\frac{\mu_n}{h_j}\left(\psi_{n,j+1/2}^{(\ell+1/2)} - \psi_{n,j-1/2}^{(\ell+1/2)}\right) + \sigma_{t,j}\psi_{n,j}^{(\ell+1/2)} = \frac{\sigma_{s,j}}{2}\phi_{0,j}^{(\ell)} + \frac{q_j}{2} \ , \tag{5a}$$

$$\psi_{n,j}^{(\ell+1/2)} = \left(\frac{1+\alpha_{n,j}}{2}\right)\psi_{n,j+1/2}^{(\ell+1/2)} + \left(\frac{1-\alpha_{n,j}}{2}\right)\psi_{n,j-1/2}^{(\ell+1/2)} \ , \tag{5b}$$

$$\psi_{n,1/2}^{(\ell+1/2)} = \psi_n^b \ , \quad \mu_n > 0 \ , \tag{5c}$$

$$\psi_{n,J+1/2}^{(\ell+1/2)} = \psi_n^b \ , \quad \mu_n < 0 \ , \tag{5d}$$

is solved by a standard transport sweep for the $\psi^{(\ell+1/2)}$ unknowns. During this sweep, the cell-averaged fluxes and (for CMFD) the cell-edge currents are computed and stored:

$$\phi_{0,j}^{(\ell+1/2)} = \sum_{n=1}^{N} \psi_{n,j}^{(\ell+1/2)} w_n \ , \tag{6a}$$

$$\phi_{1,j+1/2}^{(\ell+1/2)} = \sum_{n=1}^{N} \mu_n \psi_{n,j+1/2}^{(\ell+1/2)} w_n \ . \tag{6b}$$

In the classic Source Iteration (SI) method, the fine-mesh scalar fluxes for iteration $\ell + 1$ are defined simply from Eqs. (6) by

$$\phi_{0,j}^{(\ell+1)} = \phi_{0,j}^{(\ell+1/2)} \ , \quad 1 \leq j \leq J \ . \tag{7}$$

However, this method is very slowly converging for problems in which the system is optically thick and highly scattering. The CMDSA and CMFD methods retain Eqs. (5) and (6), but Eq. (7) is replaced by a more sophisticated calculation that can greatly reduce the total number of iterations.

To proceed, we introduce the notation for the coarse spatial grid. This grid contains $K \leq J$ disjoint "coarse" spatial cells, each consisting of a contiguous union of fine-mesh cells. If

$p_k =$ the number of fine cells in coarse cell k (ordered from left to right as k increases), then for $0 \leq k \leq K$:

$$P_0 = 0 \ , \tag{8a}$$

$$P_k = \sum_{k'=1}^{k} p_{k'} = \text{the number of fine cells in the first } k \text{ coarse cells} \ , \tag{8b}$$

$$P_K = J = \text{the total number of fine cells} \ , \tag{8c}$$

and

$$\begin{aligned} X_{k+1/2} &= x_{P_k+1/2} \\ &= \text{the right edge of the } k^{th} \text{ coarse cell} \\ &= \text{the left edge of the } (k+1)^{st} \text{ coarse cell} \ . \end{aligned} \tag{9}$$

The fine and coarse spatial cells are depicted in Figure 1:

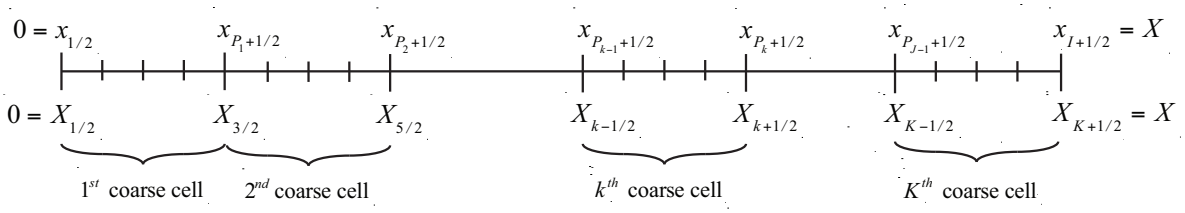

Figure 1. Fine and Coarse Spatial Grids

Next, we introduce the notation:

$$\sum_{j \in k} = \sum_{j=P_{k-1}+1}^{P_k} = \text{the sum over all fine cells } j \text{ in coarse cell } k \ , \tag{10}$$

and for $1 \leq k \leq K$ we define the coarse cell quantities:

$$\Delta_k = \sum_{j \in k} h_j = \text{width of coarse cell } k \ , \tag{11a}$$

$$\Phi_{0,k} = \frac{1}{\Delta_k} \sum_{j \in k} \phi_{0,j} h_j = \text{volume-averaged scalar flux in coarse cell } k \ , \tag{11b}$$

$$Q_k = \frac{1}{\Delta_k} \sum_{j \in k} q_j h_j = \text{volume-averaged source in coarse cell } k \ , \tag{11c}$$

$$\Phi_{1,k+1/2} = \phi_{1,P_k+1/2} = \text{current on the right edge of coarse cell } k \ , \tag{11d}$$

$$\begin{aligned} \Sigma_{u,k} &= \frac{1}{\Delta_k} \sum_{j \in k} \sigma_{u,j} h_j \\ &= \text{volume-averaged cross section in coarse cell } k \quad (u = t, s, \gamma) \ , \end{aligned} \tag{11e}$$

$$\begin{aligned} \Sigma_{u,k}^{(\ell+1/2)} &= \frac{\sum_{j \in k} \sigma_{u,j} \phi_{0,j}^{(\ell+1/2)} h_j}{\sum_{j \in k} \phi_{0,j}^{(\ell+1/2)} h_j} \\ &= \text{flux-weighted cross section in coarse cell } k \quad (u = t, s, \gamma) \ . \end{aligned} \tag{11f}$$

In these definitions, fine-cell quantities are denoted by lower-case letters; coarse-cell quantities are denoted by upper-case letters.

2.1. The Coarse Mesh Finite Difference (CMFD) Method

To derive the CMFD method, we operate on Eq. (5a) by $\sum_{n=1}^{N}(\cdot)w_n$ and get

$$\frac{1}{h_j}\left(\phi_{1,j+1/2}^{(\ell+1/2)}-\phi_{1,j-1/2}^{(\ell+1/2)}\right)+\sigma_{t,j}\phi_{0,j}^{(\ell+1/2)}=\sigma_{s,j}\phi_{0,j}^{(\ell)}+q_j\ . \tag{12}$$

Next we operate on Eq. (12) by $\sum_{j\in k}(\cdot)h_j$. Using the definitions (11), we obtain for each coarse cell k:

$$\Phi_{1,k+1/2}^{(\ell+1/2)}-\Phi_{1,k-1/2}^{(\ell+1/2)}+\Sigma_{t,k}^{(\ell+1/2)}\Phi_{0,k}^{(\ell+1/2)}\Delta_k=\Sigma_{s,k}^{(\ell)}\Phi_{0,k}^{(\ell)}\Delta_k+Q_k\Delta_k\ . \tag{13}$$

Also, we define $\hat{D}_{k+1/2}^{(\ell+1/2)}$ at each interior coarse cell edge $(1\le k\le K-1)$ by:

$$\Phi_{1,k+1/2}^{(\ell+1/2)}=-\frac{2}{3}\left(\frac{\Phi_{0,k+1}^{(\ell+1/2)}-\Phi_{0,k}^{(\ell+1/2)}}{\Sigma_{t,k+1}^{(\ell+1/2)}\Delta_{k+1}+\Sigma_{t,k}^{(\ell+1/2)}\Delta_k}\right)+\hat{D}_{k+1/2}^{(\ell+1/2)}\left(\Phi_{0,k+1}^{(\ell+1/2)}+\Phi_{0,k}^{(\ell+1/2)}\right)\ . \tag{14}$$

(Note that $\hat{D}_{k+1/2}^{(\ell+1/2)}$ *is a transport correction to Fick's Law*.) In addition, at the left edge of the system, we define $B_{1/2}^{(\ell+1/2)}$ by

$$\begin{aligned}2\Phi_{1,1/2}^{+}&=2\sum_{\mu_n>0}\mu_n\psi_n^b w_n=\sum_{n=1}^{N}\left(\mu_n+|\mu_n|\right)\psi_{n,1/2}^{(\ell+1/2)}w_n\\&=\Phi_{1,1/2}^{(\ell+1/2)}+\left(\frac{\sum_{n=1}^{N}|\mu_n|\psi_{n,1/2}^{(\ell+1/2)}w_n}{\sum_{n=1}^{N}\Psi_{n,1}^{(\ell+1/2)}w_n}\right)\Phi_{0,1}^{(\ell+1/2)}\\&=\Phi_{1,1/2}^{(\ell+1/2)}+\left(B_{1/2}^{(\ell+1/2)}\right)\Phi_{0,1}^{(\ell+1/2)}\ ,\end{aligned} \tag{15a}$$

and at the right edge of the system, we define $B_{K+1/2}^{(\ell+1/2)}$ by

$$\begin{aligned}2\Phi_{1,K+1/2}^{+}&=2\sum_{\mu_n<0}|\mu_n|\psi_n^b w_n=\sum_{n=1}^{N}\left(-\mu_n+|\mu_n|\right)\psi_{n,J+1/2}^{(\ell+1/2)}w_n\\&=-\Phi_{1,K+1/2}^{(\ell+1/2)}+\left(\frac{\sum_{n=1}^{N}|\mu_n|\psi_{n,J+1/2}^{(\ell+1/2)}w_n}{\sum_{n=1}^{N}\Psi_{n,K}^{(\ell+1/2)}w_n}\right)\Phi_{0,K}^{(\ell+1/2)}\\&=-\Phi_{1,K+1/2}^{(\ell+1/2)}+\left(B_{K+1/2}^{(\ell+1/2)}\right)\Phi_{0,K}^{(\ell+1/2)}\ .\end{aligned} \tag{15b}$$

At the conclusion of the transport sweep, (i) the $\psi^{(\ell+1/2)}$ quantities have been determined, (ii) Eqs. (13) are satisfied for each coarse cell k, (iii) Eq. (14) defines $\hat{D}_{k+1/2}^{(\ell+1/2)}$ at interior coarse cell edge, and (iv) Eqs. (15) define $B_{1/2}^{(\ell+1/2)}$ and $B_{K+1/2}^{(\ell+1/2)}$ at the left and right edges of the system. It is now possible to define, in terms of these equations, *acceleration* equations for the coarse cell-averaged scalar fluxes and the coarse cell-edge currents.

In the CMFD method, $\Phi_{0,k}^{(\ell+1)}$ and $\Phi_{1,k+1/2}^{(\ell+1)}$ are defined to be the solution of the following altered versions of Eqs. (13)-(15):

$$\Phi_{1,k+1/2}^{(\ell+1)} - \Phi_{1,k-1/2}^{(\ell+1)} + \Sigma_{t,k}^{(\ell+1/2)} \Phi_{0,k}^{(\ell+1)} \Delta_k = \Sigma_{s,k}^{(\ell+1/2)} \Phi_{0,k}^{(\ell+1)} \Delta_k + Q_k \Delta_k \ , \tag{16a}$$

$$\Phi_{1,k+1/2}^{(\ell+1)} = -\frac{2}{3} \left(\frac{\Phi_{0,k+1}^{(\ell+1)} - \Phi_{0,k}^{(\ell+1)}}{\Sigma_{t,k+1}^{(\ell+1/2)} \Delta_{k+1} + \Sigma_{t,k}^{(\ell+1/2)} \Delta_k} \right) + \hat{D}_{k+1/2}^{(\ell+1/2)} \left(\Phi_{0,k+1}^{(\ell+1)} + \Phi_{0,k}^{(\ell+1)} \right) \ , \tag{16b}$$

$$2\Phi_{1,1/2}^{+} = \Phi_{1,1/2}^{(\ell+1)} + \left(B_{1/2}^{(\ell+1/2)} \right) \Phi_{0,1}^{(\ell+1)} \ , \tag{16c}$$

$$2\Phi_{1,K+1/2}^{+} = -\Phi_{1,K+1/2}^{(\ell+1)} + \left(B_{K+1/2}^{(\ell+1/2)} \right) \Phi_{0,J}^{(\ell+1)} \ . \tag{16d}$$

The coarse cell-edge currents in these equations, $\Phi_{1,k+1/2}^{(\ell+1)}$, can be algebraically eliminated, yielding a tri-diagonal system of K equations for the coarse cell-averaged scalar fluxes $\Phi_{0,k}^{(\ell+1)}$, $1 \leq k \leq K$. After $\Phi_{0,k}^{(\ell+1)}$ are obtained, the accelerated fine-cell scalar fluxes are defined as

$$\phi_{0,j}^{(\ell+1)} = \phi_{0,j}^{(\ell+1/2)} \left(\frac{\Phi_{0,k}^{(\ell+1)}}{\Phi_{0,k}^{(\ell+1)}} \right) \ , \quad j \in k \ , \quad 1 \leq k \leq K \ . \tag{17}$$

This completes the description of the CMFD method.

2.2. The Coarse Mesh Diffusion Synthetic Acceleration (CMDSA) Method

To derive the CMDSA method, we define the exact fine-mesh iteration errors after the ℓ^{th} transport sweep:

$$f_{1,j+1/2} = \phi_{1,j+1/2} - \phi_{1,j+1/2}^{(\ell+1/2)} \ , \tag{18a}$$

$$f_{0,j} = \phi_{0,j} - \phi_{0,j}^{(\ell+1/2)} \ . \tag{18b}$$

These can easily be shown, using Eq. (12), to satisfy:

$$\frac{1}{h_j} \left(f_{1,j+1/2} - f_{1,j-1/2} \right) + \sigma_{a,j} f_{0,j} = \sigma_{s,j} \left(\phi_{0,j}^{(\ell+1/2)} - \phi_{0,j}^{(\ell)} \right) \ , \ \ 1 \leq k \leq K \ .$$

Equivalently, for each $j \in k$,

$$\frac{1}{h_j} \left(f_{1,j+1/2} - f_{1,j-1/2} \right) + \Sigma_{a,k} f_{0,j} = \sigma_{s,j} \left(\phi_{0,j}^{(\ell+1/2)} - \phi_{0,j}^{(\ell)} \right) + \left(\Sigma_{a,k} - \sigma_{a,j} \right) f_{0,j} \ . \tag{19}$$

Operating on this result by $\sum_{j \in k} (\cdot) h_j$ and defining the coarse cell quantities

$$F_{0,k} = \frac{1}{\Delta_k} \sum_{j \in k} f_{0,j} h_j \ , \tag{20a}$$

$$F_{1,k+1/2} = f_{1,P_k+1/2} \ , \tag{20b}$$

we get:

$$F_{1,k+1/2} - F_{1,k-1/2} + \Sigma_{a,k} F_{0,k} \Delta_k = \sum_{j \in k} \sigma_{s,j} \left(\phi_{0,j}^{(\ell+1/2)} - \phi_{0,j}^{(\ell)} \right) h_j + \sum_{j \in k} \left(\Sigma_{a,k} - \sigma_{a,j} \right) f_{0,j} h_j \ . \tag{21}$$

Eqs. (21) are K equations for the $2K+1$ quantities $F_{0,k}$ and $F_{1,k+1/2}$. (Also, the fine-mesh quantities $f_{0,j}$ on the right side of these equations are not known.)

In the CMDSA method, $F_{0,k}^{(\ell+1)}$ and $F_{1,k+1/2}^{(\ell+1)}$ are determined by the following approximation to Eqs. (21):

$$F_{1,k+1/2}^{(\ell+1)} - F_{1,k-1/2}^{(\ell+1)} + \Sigma_{a,k} F_{0,k}^{(\ell+1)} \Delta_k = \sum_{j \in k} \sigma_{s,j} \left(\phi_{0,j}^{(\ell+1/2)} - \phi_{0,j}^{(\ell)} \right) h_j \ , \quad 1 \le k \le K \ , \tag{22a}$$

together with the "diffusion" assumptions:

$$F_{1,k+1/2}^{(\ell+1)} = -\frac{2}{3} \left(\frac{F_{0,k+1}^{(\ell+1)} + F_{0,k}^{(\ell+1)}}{\Sigma_{t,k+1} \Delta_{k+1} + \Sigma_{t,k} \Delta_k} \right) \quad , \quad 1 \le k \le K-1 \ , \tag{22b}$$

$$0 = F_{1,1/2}^{(\ell+1)} + \beta F_{0,1}^{(\ell+1)} \ , \tag{22c}$$

$$0 = -F_{1,K+1/2}^{(\ell+1)} + \beta F_{0,K}^{(\ell+1)} \ , \tag{22d}$$

where

$$\beta \equiv \frac{1}{2} \left(\sum_{n=1}^{N} |\mu_n| w_n \right) \approx \frac{1}{2} \ . \tag{23}$$

The cell-edge current corrections $F_{1,k+1/2}^{(\ell+1)}$ in Eqs. (22) can be algebraically eliminated, yielding a tridiagonal system of K equations for $F_{0,k}^{(\ell+1)}$, $1 \le k \le K$. After these quantities are calculated, the accelerated fine-cell scalar fluxes are defined as

$$\phi_{0,j}^{(\ell+1)} = \phi_{0,j}^{(\ell+1/2)} + F_{0,k}^{(\ell+1)} \ , \quad j \in k \ , \quad 1 \le k \le K \ . \tag{24}$$

This completes the description of the CMDSA method.

3. THE LINEARIZED COARSE MESH FINITE DIFFERENCE (LCMFD) METHOD

To describe the new linearization procedure, we consider the transport problem defined by Eqs. (2), with

$$q_j = \Sigma_{a,j} \Lambda + \varepsilon \tilde{q}_j \ , \tag{25a}$$

$$\psi_n^b = \frac{\Lambda}{2} + \varepsilon \tilde{\psi}_n^b \ , \tag{25b}$$

where Λ is an arbitrary constant and $\varepsilon \ll 1$. For $\varepsilon = 0$, the resulting problem has the exact "flat" solution

$$\psi_{n,j} = \psi_{n,j+1/2} = \frac{\Lambda}{2} \ .$$

If we set

$$\psi_{n,j} = \frac{\Lambda}{2} + \varepsilon\tilde{\psi}_{n,j} \ , \tag{26a}$$

$$\psi_{n,j+1/2} = \frac{\Lambda}{2} + \varepsilon\tilde{\psi}_{n,j+1/2} \ , \tag{26b}$$

then Eqs. (2) for $\psi_{n,j}$ and $\psi_{n,j+1/2}$ easily reduce to

$$\frac{\mu_n}{h_j}\left(\tilde{\psi}_{n,j+1/2} - \tilde{\psi}_{n,j+1/2}\right) + \sigma_{t,j}\tilde{\psi}_{n,j} = \frac{\sigma_{s,j}}{2}\sum_{m=1}^{N}\tilde{\psi}_{m,j}w_m + \frac{\tilde{q}_j}{2} \ , \tag{27a}$$

$$\tilde{\psi}_{n,j} = \left(\frac{1+\alpha_{n,j}}{2}\right)\tilde{\psi}_{n,j+1/2} + \left(\frac{1-\alpha_{n,j}}{2}\right)\tilde{\psi}_{n,j-1/2} \ , \tag{27b}$$

$$\tilde{\psi}_{n,1/2} = \tilde{\psi}^b_n \ , \quad \mu_n > 0 \ , \tag{27c}$$

$$\tilde{\psi}_{n,J+1/2} = \tilde{\psi}^b_n \ , \quad \mu_n < 0 \ . \tag{27d}$$

These equations are identical to (2), except that ψ and q have been replaced by $\tilde{\psi}$ and $\tilde{q}$. (Of course, this happens because Eqs. (2) are linear.)

Because the CMDSA method is linear, the CMDSA equations obtained by introducing Eqs. (25) and (26) are also the same as the original equations, but with ψ's, ϕ's, and q's replaced by $\tilde{\psi}$'s, $\tilde{\phi}$'s, and $\tilde{q}$'s. Explicitly, the fine-mesh transport sweep (5) becomes:

$$\frac{\mu_n}{h_j}\left(\tilde{\psi}^{(\ell+1/2)}_{n,j+1/2} - \tilde{\psi}^{(\ell+1/2)}_{n,j-1/2}\right) + \sigma_{t,j}\tilde{\psi}^{(\ell+1/2)}_{n,j} = \frac{\Sigma_{s,j}}{2}\tilde{\phi}^{(\ell)}_{0,j} + \frac{\tilde{q}_j}{2} \ , \tag{28a}$$

$$\tilde{\psi}^{(\ell+1/2)}_{n,j} = \left(\frac{1+\alpha_{n,j}}{2}\right)\tilde{\psi}^{(\ell+1/2)}_{n,j+1/2} + \left(\frac{1-\alpha_{n,j}}{2}\right)\tilde{\psi}^{(\ell+1/2)}_{n,j-1/2} \ , \tag{28b}$$

$$\tilde{\psi}^{(\ell+1/2)}_{n,1/2} = \tilde{\psi}^b_n \ , \quad \mu_n > 0 \ , \tag{28c}$$

$$\tilde{\psi}^{(\ell+1/2)}_{n,J+1/2} = \tilde{\psi}^b_n \ , \quad \mu_n < 0 \ , \tag{28d}$$

the "updated" scalar fluxes are:

$$\tilde{\phi}^{(\ell+1/2)}_{0,j} = \sum_{n=1}^{N}\tilde{\psi}^{(\ell+1/2)}_{n,j}w_n \ , \tag{29}$$

the low-order coarse-grid "diffusion" Eqs. (22) (with $\tilde{F} = \varepsilon F$) become:

$$\tilde{F}^{(\ell+1)}_{1,k+1/2} - \tilde{F}^{(\ell+1)}_{1,k-1/2} + \Sigma_{a,k}\tilde{F}^{(\ell+1)}_{0,k}\Delta_k = \sum_{j\in k}\sigma_{s,j}\left(\tilde{\phi}^{(\ell+1/2)}_{0,j} - \tilde{\phi}^{(\ell)}_{0,j}\right)h_j \ ,$$

$$1 \le k \le K \ , \tag{30a}$$

$$\tilde{F}^{(\ell+1)}_{1,k+1/2} = -\frac{2}{3}\left(\frac{\tilde{F}^{(\ell+1)}_{0,k+1} - \tilde{F}^{(\ell+1)}_{0,k}}{\Sigma_{t,k+1}\Delta_{k+1} + \Sigma_{t,k}\Delta_k}\right) \ , \quad 1 \le k \le K-1 \ , \tag{30b}$$

$$0 = \tilde{F}^{(\ell+1)}_{1,1/2} + \beta\tilde{F}^{(\ell+1)}_{0.1} \ , \tag{30c}$$

$$0 = -\tilde{F}^{(\ell+1)}_{1,K+1/2} + \beta\tilde{F}^{(\ell+1)}_{0,K} \ , \tag{30d}$$

and the fine-grid, accelerated scalar flux equation (24) becomes:

$$\tilde{\phi}_{0,j}^{(\ell+1)} = \tilde{\phi}_{0,j}^{(\ell+1/2)} + \tilde{F}_{0,k}^{(\ell+1)} \ , \quad j \in k \ , \quad 1 \le k \le K \ . \tag{31}$$

To repeat, these equations are identical to the original equations, except that all quantities scaled by ε now have a tilde. This occurs because, like the original transport problem, the CMDSA equations are linear.

The CMFD method however is nonlinear, and this method is altered when Eqs. (25) and (26) are introduced and the resulting equations are expanded in powers of ε. For the CMFD method, the (linear) fine-mesh transport sweep and "update" equations are the same as with CMDSA, and are described by Eqs. (28) and (29).

Introducing Eqs. (25) and (26) into (16) and expanding in ε, we obtain a different set of low-order diffusion equations for $\tilde{\Phi}_{0,k}^{(\ell+1)}$. A key identity is:

$$\begin{aligned}
\Sigma_{a,k}^{(\ell+1/2)}\Phi_{0,k}^{(\ell+1)} &= \frac{\sum_{j\in k}\sigma_{a,j}\left(\Lambda+\varepsilon\tilde{\phi}_{0,j}^{(\ell+1/2)}\right)h_j}{\sum_{j\in k}\left(\Lambda+\varepsilon\tilde{\phi}_{0,j}^{(\ell+1/2)}\right)h_j}\left[\Lambda+\varepsilon\tilde{\Phi}_{0,k}^{(\ell+1)}\right] \\
&= \frac{\Lambda\Sigma_{a,k}\Delta_k+\varepsilon\sum_{j\in k}\sigma_{a,j}\tilde{\phi}_{0,j}^{(\ell+1/2)}h_j}{\Lambda\Delta_k+\varepsilon\sum_{j\in k}\tilde{\phi}_{0,j}^{(\ell+1/2)}h_j}\left[\Lambda+\varepsilon\tilde{\Phi}_{0,k}^{(\ell+1)}\right] \\
&= \cdots \\
&= \Sigma_{a,k}\Lambda+\varepsilon\left[\frac{1}{\Delta_k}\sum_{j\in k}(\sigma_{a,j}-\Sigma_{a,k})\tilde{\phi}_{0,j}^{(\ell+1/2)}h_j+\Sigma_{a,k}\tilde{\Phi}_{0,k}^{(\ell+1)}\right] \ .
\end{aligned} \tag{32}$$

Eq. (16a) becomes:

$$\tilde{\Phi}_{1,k+1/2}^{(\ell+1)}-\tilde{\Phi}_{1,k-1/2}^{(\ell+1)}+\Sigma_{a,k}\tilde{\Phi}_{0,k}^{(\ell+1)}\Delta_k=\tilde{Q}_k\Delta_k+\sum_{j\in k}\left(\Sigma_{a,k}-\sigma_{a,j}\right)\tilde{\phi}_{0,j}^{(\ell+1/2)}h_j \ . \tag{33}$$

Also, Eq. (14) for $\hat{D}_{k+1/2}^{(\ell+1/2)}$ yields

$$\hat{D}_{k+1/2}^{(\ell+1/2)}=\frac{\varepsilon}{2\Lambda}\left[\tilde{\Phi}_{1,k+1/2}^{(\ell+1/2)}+\frac{2}{3}\left(\frac{\tilde{\Phi}_{0,k+1}^{(\ell+1/2)}-\tilde{\Phi}_{0,k}^{(\ell+1/2)}}{\Sigma_{t,k+1}\Delta_{k+1}+\Sigma_{t,k}\Delta_k}\right)\right]+O(\varepsilon^2) \ . \tag{34}$$

Using this result in Eq. (16b), we obtain for $1 \le k \le K-1$:

$$\tilde{\Phi}_{1,k+1/2}^{(\ell+1)}=-\frac{2}{3}\left(\frac{\tilde{\Phi}_{0,k+1}^{(\ell+1)}-\tilde{\Phi}_{0,k}^{(\ell+1)}}{\Sigma_{t,k+1}\Delta_{k+1}+\Sigma_{t,k}\Delta_k}\right)+\tilde{\Phi}_{1,k+1/2}^{(\ell+1/2)}+\frac{2}{3}\left(\frac{\tilde{\Phi}_{0,k+1}^{(\ell+1/2)}-\tilde{\Phi}_{0,k}^{(\ell+1/2)}}{\Sigma_{t,k+1}\Delta_{k+1}+\Sigma_{t,k}\Delta_k}\right) \ . \tag{35}$$

Introducing Eqs. (25) and (26) into Eq. (16c), we get

$$2\sum_{\mu_n>0}\mu_n\left(\frac{\Lambda}{2}+\varepsilon\tilde{\psi}_n^b\right)w_n=\varepsilon\tilde{\Phi}_{1,1/2}^{(\ell+1)}+\frac{\sum_{n=1}^{N}|\mu_n|\left(\frac{\Lambda}{2}+\varepsilon\tilde{\psi}_{n,1/2}^{(\ell+1/2)}\right)w_n}{\Lambda+\varepsilon\tilde{\Phi}_{0,1}^{(\ell+1/2)}}\left(\Lambda+\varepsilon\tilde{\Phi}_{0,1}^{(\ell+1)}\right) \ .$$

Expanding this equation in ε and discarding the $O(\varepsilon^2)$ terms, we obtain

$$\tilde{\Phi}_{1,1/2}^{(\ell+1)} + \beta\tilde{\Phi}_{0,1}^{(\ell+1)} = \tilde{\Phi}_{1,1/2}^{(\ell+1/2)} + \beta\tilde{\Phi}_{0,1}^{(\ell+1/2)} \ . \tag{36a}$$

At the right edge of the system, a similar result holds:

$$-\tilde{\Phi}_{1,K+1/2}^{(\ell+1)} + \beta\tilde{\Phi}_{0,J}^{(\ell+1)} = -\tilde{\Phi}_{1,K+1/2}^{(\ell+1/2)} + \beta\tilde{\Phi}_{0,K}^{(\ell+1/2)} \ . \tag{36b}$$

Finally, the fine-grid acceleration Eq. (17) becomes, for $j \in k$:

$$\Lambda + \varepsilon\tilde{\phi}_{0,j}^{(\ell+1)} = \left(\Lambda + \varepsilon\tilde{\phi}_{0,j}^{(\ell+1/2)}\right)\left(\frac{\Lambda + \varepsilon\tilde{\Phi}_{0,k}^{(\ell+1)}}{\Lambda + \varepsilon\tilde{\Phi}_{0,k}^{(\ell+1/2)}}\right) \ . \tag{37}$$

Expanding this result in powers of ε and dropping terms of $O(\varepsilon^2)$, we obtain

$$\tilde{\phi}_{0,j}^{(\ell+1)} = \tilde{\phi}_{0,j}^{(\ell+1/2)} + \left(\tilde{\Phi}_{0,k}^{(\ell+1)} - \tilde{\Phi}_{0,k}^{(\ell+1/2)}\right) , \quad j \in k \ , \quad 1 \le k \le K \ . \tag{38}$$

To summarize, the linearized CMFD method is defined by:

1. Transport sweep: Eqs. (28)
2. Updated scalar flux: Eq. (29)
3. Low-order coarse-grid diffusion equation: Eqs. (33), (35), (36)
4. Accelerated fine-grid scalar fluxes: Eq. (38)

The first two (transport sweep) steps [Eqs. (28) and (29)] are identical for the CMDSA and LCMFD methods. The low-order CMDSA Eqs. (22) and (24) are for $\tilde{F}_{0,k}^{(\ell+1)}$ and $\tilde{F}_{1,k+1/2}^{(\ell+1)}$, while the low-order LCMFD Eqs. (33), (35), (36), and (38) are for $\tilde{\Phi}_{0,k}^{(\ell+1)}$ and $\tilde{\Phi}_{1,k+1/2}^{(\ell+1)}$. The low-order LCMFD equations are equivalent to the low-order CMDSA equations if:

$$\tilde{F}_{0,k}^{(\ell+1)} = \tilde{\Phi}_{0,k}^{(\ell+1)} - \tilde{\Phi}_{0,k}^{(\ell+1/2)} \ , \tag{39a}$$

$$\tilde{F}_{1,k+1/2}^{(\ell+1)} = \tilde{\Phi}_{1,k+1/2}^{(\ell+1)} - \tilde{\Phi}_{1,k+1/2}^{(\ell+1/2)} \ . \tag{39b}$$

To confirm these identities, we show that by assuming them, the low-order LCMFD equations (which contain $\tilde{F}^{(\ell+1)}$) become algebraically equivalent to the low-order CMDSA equations (which contain $\tilde{\Phi}^{(\ell+1)}$).

At the conclusion of a transport sweep, Eq. (28a) holds, so

$$\frac{1}{h_j}\left(\tilde{\phi}_{1,j+1/2}^{(\ell+1/2)} - \tilde{\phi}_{1,j-1/2}^{(\ell+1/2)}\right) + \sigma_{t,j}\tilde{\phi}_{0,j}^{(\ell+1/2)} = \sigma_{s,j}\tilde{\phi}_{0,j}^{(\ell)} + \tilde{q}_j \ .$$

Equivalently,

$$\frac{1}{h_j}\left(\tilde{\phi}_{1,j+1/2}^{(\ell+1/2)} - \tilde{\phi}_{1,j-1/2}^{(\ell+1/2)}\right) + \Sigma_{a,k}\tilde{\phi}_{0,j}^{(\ell+1/2)} = \sigma_{s,j}\left(\tilde{\phi}_{0,j}^{(\ell)} - \tilde{\phi}_{0,j}^{(\ell+1/2)}\right) + \tilde{q}_j + \left(\Sigma_{a,k} - \sigma_{a,j}\right)\tilde{\phi}_{0,j}^{(\ell+1/2)} \ . \tag{40}$$

Operating on this result by $\sum_{j\in k}(\cdot)h_j$, we obtain

$$\tilde{\Phi}^{(\ell+1/2)}_{1,k+1/2} - \tilde{\Phi}^{(\ell+1/2)}_{1,k-1/2} + \Sigma_{a,k}\tilde{\Phi}^{(\ell+1/2)}_{0,k}\Delta_k = \sum_{j\in k}\sigma_{s,j}\left(\tilde{\phi}^{(\ell)}_{0,j} - \tilde{\phi}^{(\ell+1/2)}_{0,j}\right)h_j + \tilde{Q}_k\Delta_k + \sum_{j\in k}\left(\Sigma_{a,k} - \sigma_{a,j}\right)\tilde{\phi}^{(\ell+1/2)}_{0,j}h_j \ . \tag{41}$$

Subtracting Eq. (41) from the LCMFD balance Eq. (33) and using the definitions (39), we get

$$\tilde{F}^{(\ell+1)}_{1,k+1/2} - \tilde{F}^{(\ell+1)}_{1,k-1/2} + \Sigma_{a,k}\tilde{F}^{(\ell+1)}_{0,k}\Delta_k = \sum_{j\in k}\sigma_{s,j}\left(\tilde{\phi}^{(\ell+1/2)}_{0,j} - \tilde{\phi}^{(\ell)}_{0,j}\right)h_j \ . \tag{42}$$

This is the CMDSA balance Eq. (30a).

Next, Eqs. (35) and (39) immediately give

$$\tilde{F}^{(\ell+1)}_{1,k+1/2} = -\frac{2}{3}\left(\frac{\tilde{F}^{(\ell+1)}_{0,k+1/2} - \tilde{F}^{(\ell+1)}_{0,k}}{\Sigma_{t,k+1}\Delta_{k+1} + \Sigma_{t,k}\Delta_k}\right) \ . \tag{43}$$

This is the CMDSA Fick's Law, Eq. (30b).

Next, Eqs. (36) and (39) immediately give

$$0 = \tilde{F}^{(\ell+1)}_{1,1/2} + \beta\tilde{F}^{(\ell+1)}_{0,1} \ , \tag{44a}$$

$$0 = -\tilde{F}^{(\ell+1)}_{1,K+1/2} + \beta\tilde{F}^{(\ell+1)}_{0,K} \ . \tag{44b}$$

These are the CMDSA boundary conditions, Eqs. (30c) and (30d).

Finally, Eqs. (38) and (39) become

$$\tilde{\phi}^{(\ell+1)}_{0,j} = \tilde{\phi}^{(\ell+1/2)}_{0,j} + \tilde{F}^{(\ell+1)}_{0,k} \ , \quad j\in k \ , \quad 1\le k\le K \ . \tag{45}$$

This is the CMDSA acceleration Eq. (31).

Eqs. (42)-(45) confirm that *the LCMFD and CMDSA methods are algebraically equivalent*.

Previously, linearizations of nonlinear transport acceleration methods have been obtained only for homogeneous systems with flat sources and uniform grids [8, 10–13]. In the more general linearization performed in this paper, the physical system does not need to be homogeneous, the sources do not need to be flat, and the spatial grid does not need to be uniform. This establishes a much closer theoretical link between the nonlinear CMFD and the linear CMDSA methods – these methods are nearly equivalent over a larger class of problems.

The details of the CMDSA discretization method discussed in this paper were chosen to exactly match the linearized CMFD discretization method. However, there are choices in how these discretizations can be done (particularly in the choice of boundary conditions), and these choices determine whether there is exact algebraic equivalence between the LCMFD and CMDSA methods. The main theme of this paper is that for any specific CMFD method, the linearization of this method (in the manner shown above) is algebraically equivalent to a specific CMDSA method.

4. NUMERICAL RESULTS

We have performed a Fourier analysis of the LCMFD and CMDSA methods, but we do not present this work here because of its similarity to the previous work of Cho and Park [8]. However, we do include several figures depicting spectral radii obtained by (i) Fourier analysis predictions, and (ii) direct numerical simulations of the CMFD and CMDSA methods.

The planar geometry problem for measuring the spectral radius of the CMDSA method has a vacuum boundary on the left edge and a reflecting boundary on the right edge with no interior source. The solution of this problem is $\psi = 0$. We initialize the iterative CMDSA method with a step function (to seed a large number of Fourier modes) and observe the solution's convergence to zero. For this problem, the *spectral radius* (defined as the asymptotic rate of convergence) is estimated as:

$$\rho = \frac{\left|\left|\phi^{(\ell+1)}\right|\right|}{\left|\left|\phi^{(\ell)}\right|\right|} \ . \tag{46}$$

If $\rho \geq 1$, the method diverges; but if $\rho < 1$, the method converges, and the smaller the value of ρ, the faster the convergence.

Unfortunately, this problem cannot measure the spectral radius of CMFD because the lack of an interior and boundary source causes the low-order problem to produce the correct zero solution in a single iteration. Instead, we choose the same boundary conditions but with a step function source within the system. The CMFD spectral radius can then be estimated as:

$$\rho = \frac{\left|\left|\phi^{(\ell+1)} - \phi^{(\ell)}\right|\right|}{\left|\left|\phi^{(\ell)} - \phi^{(\ell-1)}\right|\right|} \ . \tag{47}$$

The following figures present theoretical and experimental estimates of ρ for various coarse cell optical thicknesses, scattering ratios, and numbers of fine cells per coarse cell.

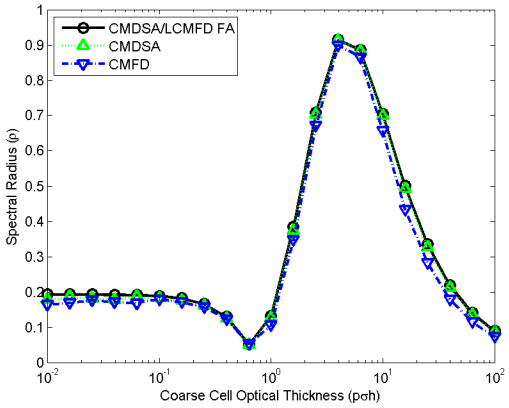

Figure 2. $p = 1$ and $c = 0.9$

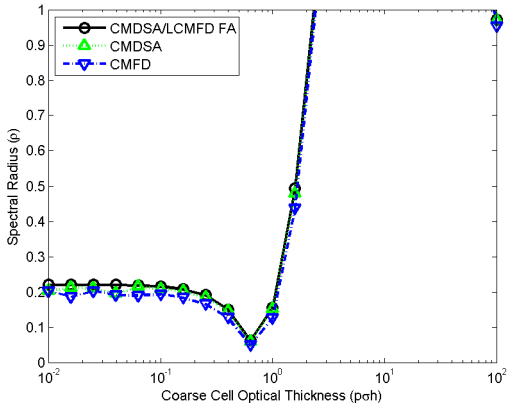

Figure 3. $p = 1$ and $c = 0.99$

Figures 2 and 3 describe *fine mesh acceleration* (each coarse spatial cell contains $p = 1$ fine spatial cell). In this case, the CMDSA method is the same as the standard DSA method. For small scattering ratios c, the CMDSA and CMFD methods are seen to be stable for all coarse spatial cells and efficient for most coarse spatial cells. However, as c increases, the methods become

unstable for coarse spatial cells greater than about one mean free path thick. The CMDSA and CMFD methods have almost identical spectral radii, and the agreement between theory (Fourier analysis) and experiment (numerical simulation) is seen to be excellent.

Figures 4 and 5 describe *coarse mesh acceleration* in which each coarse spatial cell contains $p = 2$ fine mesh cells. Qualitatively, the results are similar to fine mesh acceleration: the CMDSA and CMFD methods converge rapidly for coarse spatial cells less than about one mean free path thick, but for scattering ratios near unity, the methods become unstable for coarse spatial cells greater than about one mean free path. The $p = 2$ spectral radii are higher than the $p = 1$ spectral radii, as should be expected because the same coarse mesh calculation is now accelerating twice as many fine-mesh unknowns. As before, the CMDSA and CMFD methods have almost the same spectral radii; the agreement between theory and experiment is excellent.

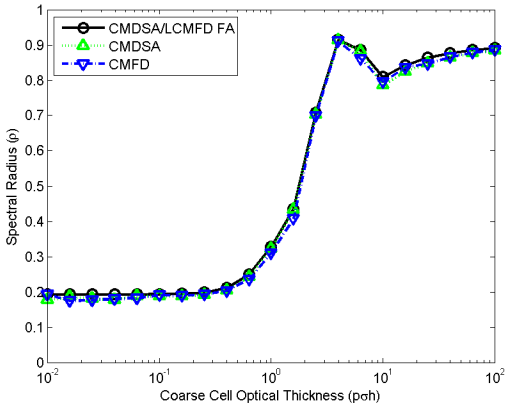

Figure 4. $p = 2$ and $c = 0.9$

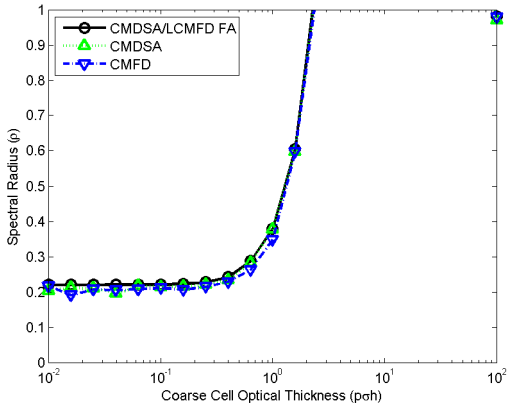

Figure 5. $p = 2$ and $c = 0.99$

Figures 6 and 7 describe coarse mesh acceleration with $p = 4$ fine cells per coarse spatial cell. The trends noted previously are continued in these figures, including the excellent agreement between theory and experiment.

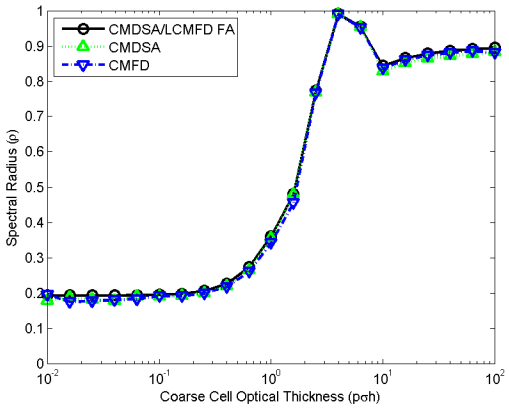

Figure 6. $p = 4$ and $c = 0.9$

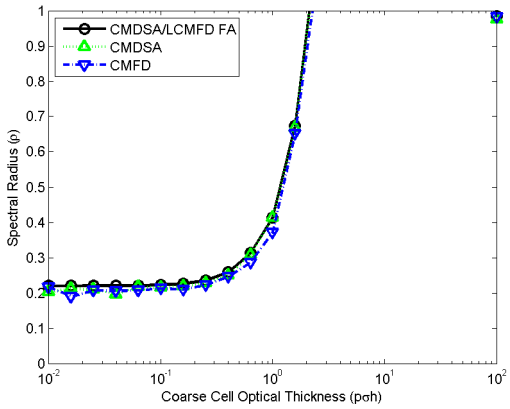

Figure 7. $p = 4$ and $c = 0.99$

Finally, we note that our numerical results are consistent with the results obtained previously by Cho and Park [8].

5. CONCLUSIONS

We have shown and demonstrated numerically a close theoretical relationship between the DSA and CMFD methods for accelerating the iterative convergence of particle transport calculations. These two iteration methods were developed independently and have been used for many years in production neutron transport codes.

To the reader who has patiently followed the detailed mathematics in the earlier part of this paper, a reasonable question is: why does the algebraic equivalence hold between CMFD and CMDSA? The answer is that the two methods are, at their root, sufficiently similar. Both methods employ a fine grid transport sweep, a low-order diffusion equation containing "consistency" terms from the transport sweep, and an update equation in which the low-order solution is used to improve the fine-grid scalar fluxes. The basic difference between the two methods (CMFD is nonlinear, DSA is linear) has obfuscated the two methods' otherwise close theoretical relationship.

To the reader who is familiar with the history of DSA and the long (and only partly successful) effort to derive unconditionally stable versions of this method for specified transport discretization schemes, another natural question is: if CMFD is stable only for coarse spatial cells less than about one mean free path thick, then how could this method be so successful (i.e. stable) in practical problems? The answer seems to have two parts:

1. For practical multigroup problems, CMFD is observed to be more stable than for one-group problems; the "practical" borderline of instability becomes 2-3 mean free paths [14].
2. In practice, CMFD is used to accelerate the convergence of multigroup reactor core simulations in which a coarse spatial cell is chosen to be a single pin cell – which is roughly 1-2 mean free paths across, and hence within multigroup CMFD's "practical" range of stability. The fine spatial cells (within a coarse cell) are used to resolve the fuel, cladding, and moderator regions inside a pin cell. CMFD has been highly successful for reactor physics problems in which a coarse cell is a *single* pin cell, but it is not widely understood that if the coarse grid is sufficiently enlarged to include *multiple* pin cells, the method will become divergent.

The results in this paper facilitate the following prediction: if a CMDSA method were implemented to accelerate the *inner* iterations of a k-eigenvalue problem (in which the fission source and eigenvalue estimate are fixed), it would have the same convergence properties as CMFD for problems in which CMFD converges. However, if CMFD fails to converge the inner iterations because the inner iterations produce a negative estimate of the scalar flux en route to convergence, the CMDSA method will converge. Thus: CMDSA, because of its linearity, should be advantageous for accelerating the inner iterations, while CMFD, because of its nonlinearity, should be advantageous for accelerating the outer iterations. We plan to test this prediction in future work.

ACKNOWLEDGEMENTS

We gratefully acknowledge support of this research through the U.S. Department of Energy NEUP grant DE-AC07-05ID14517.

REFERENCES

[1] M.L. Adams and E.W. Larsen, "Fast Iterative Methods for Discrete-Ordinates Particle Transport Calculations," *Prog. Nucl. Energy,* **40**, 3 (2002).

[2] H.J. Kopp, "Synthetic Method Solution of the Transport Equation," *Nucl. Sci. Eng.,* **17**, 65 (1963).

[3] R. Alcouffe, "Diffusion Synthetic Acceleration Methods for the Diamond-Differenced Discrete-Ordinates Equations," *Nucl. Sci. Eng.,* **64**, 344 (1977).

[4] E.W. Larsen, "Unconditionally Stable Diffusion-Synthetic Acceleration Methods for the Slab Geometry Discrete-Ordinates Equations. Part I: Theory," *Nucl. Sci. Eng.,* **82**, 47 (1982).

[5] D.R. McCoy and E.W. Larsen, "Unconditionally Stable Diffusion-Synthetic Acceleration Methods for the Slab Geometry Discrete-Ordinates Equations. Part II: Numerical Results," *Nucl. Sci. Eng.,* **82**, 64 (1982).

[6] K. Smith, "Nodal Method Storage Reduction by Nonlinear Iteration," *Trans. Am. Nucl. Soc.,* **44**, 265 (1983).

[7] K. Smith, "Assembly Homogenization Techniques for Light Water Reactor Analysis," *Prog. Nucl. Energy,* **17**, 303 (1986).

[8] N.Z. Cho and C.J. Park, "A Comparison of Coarse Mesh Rebalance and Coarse Mesh Finite Difference Accelerations for the Neutron Transport Calculations," *Proc. Conf. Nuclear, Mathematical, and Computational Sciences: a Century in Review, a Century Anew*, Gatlinburg, Tennessee, April 6-11, 2003, American Nuclear Society (2003). [CD-ROM]

[9] Z. Zhong, T.J. Downar, Y. Xu, M.D. DeHart, and K.T. Clarno, "Implementation of Two-Level Coarse-Mesh Finite Difference Acceleration in an Arbitrary Geometry, Two-Dimensional Discrete Ordinates Transport Method," *Nucl. Sci. Eng.,* **158**, 289 (2008).

[10] G.R. Cefus and E.W. Larsen, "Stability Analysis of Coarse Mesh Rebalance," *Nucl. Sci. Eng.,* **105**, 31 (1990).

[11] G.R. Cefus and E.W. Larsen, "Stability Analysis of the Quasidiffusion and Second Moment Methods for Iteratively Solving Discrete-Ordinates Problems," *Transport Theory Statist. Phys.,* **18**, 493 (1990).

[12] Y.R. Park and N.Z. Cho, "Coarse-Mesh Angular Dependent Rebalance Acceleration of the Discrete Ordinates Transport Calculations," *Nucl. Sci. Eng.,* **148**, 355 (2004).

[13] Y.R. Park and N.Z. Cho, "Coarse-Mesh Angular Dependent Rebalance Acceleration of the Method of Characteristics in x-y Geometry," *Nucl. Sci. Eng.,* **158**, 154 (2008).

[14] K. Smith, personal communication.

PHYSOR 2012 Advances in Reactor Physics Linking Research, Industry, and Education
Knoxville, Tennessee, USA, April 15-20, 2012, on CD-ROM, American Nuclear Society, LaGrange Park, IL (2012)

CMFD ACCELERATION OF SPATIAL DOMAIN-DECOMPOSED NEUTRON TRANSPORT PROBLEMS

Blake W. Kelley and Edward W. Larsen
Department of Nuclear Engineering and Radiological Sciences
University of Michigan
Ann Arbor, Michigan 48109-2104 USA
kelleybl@umich.edu; edlarsen@umich.edu

ABSTRACT

A significant limitation to parallelizing the solution of neutron transport problems is the need for sweeps across the entirety of the problem domain. Angular domain decomposition is common practice, as the equations for each direction are independent aside from their shared scattering/fission source. Accordingly, spatial domain decomposition does not naturally arise in the transport equations and is therefore less frequent in practice. In this paper, we show that a neutron transport domain can be straightforwardly divided into independent, parallelizable sweep regions, globally linked with the standard CMFD method, with an additional update equation. We verify, theoretically (via Fourier analysis) and computationally, that the convergence properties of this method are stable and nominally as rapid as standard CMFD.

Key Words: CMFD, spatial domain decomposition, Fourier Analysis

1. INTRODUCTION

High performance computing requires that algorithms be parallel. For the method of characteristics and discrete ordinates, it is standard practice to parallelize the angular modes of the sweeps using multiple threads and message passing. However, this is often done such that each distributed memory process has to retain information about the global problem. By decomposing in space, it is possible to distribute rather than replicate the problem information over distributed memory architectures.

Azmy [1] parallelizes the whole-core sweeps by distributing computation effort following a wave-front sweeping progression; this method still requires that some of the sub-domain sweeps must be solved sequentially. Meanwhile, Van Criekingen [2] parallelizes the sweeps by implementing overlapping domain decomposition on the even parity transport equations; however, the overlapping domain decomposition repeats problem information in the sub-domains and has no explicit acceleration other than the overlapping regions.

Adams [3] and Zhang [4] both implement domain decomposition through algebraic means, while Santandrea [5] does this by making careful approximations to the sub-domain boundaries. Previously, Yavuz and Larsen [6] implemented a non-overlapping spatial domain decomposition for transport problems in which the scattering source and sub-domain boundary quantities were accelerated with DSA [7–11]; unfortunately, DSA is only well-suited for problems with a rectilinear mesh and cannot *directly* accelerate eigenvalue problems.

In this paper we introduce an algorithm based on the well known CMFD method [12–15] with slight modifications for effectively sweeping and accelerating MOC and S_N methods on parallel frameworks. We provide experimental and theoretical estimates of the spectral radius to verify these claims.

2. THE SPATIAL DOMAIN DECOMPOSITION CMFD (SDD-CMFD) METHOD

Here we describe the SDD-CMFD method for a planar geometry fixed-source problem on the system $0 \leq x \leq X$, with a vacuum boundary condition on the left side of the problem and a reflecting boundary condition on the right side:

$$\mu \frac{\partial \psi}{\partial x}(x,\mu) + \sigma_t(x)\psi(x,\mu) = \frac{\sigma_s(x)}{2}\int_{-1}^{1}\psi(x,\mu')d\mu' + \frac{q(x)}{2}\ , \tag{1a}$$

$$\psi(0,\mu) = 0\ ,\quad 0 < \mu \leq 1\ , \tag{1b}$$

$$\psi(X,\mu) = \psi(X,-\mu)\ ,\quad -1 \leq \mu < 0\ . \tag{1c}$$

Before discretizing the system, we wish to orient the reader with the three levels of spatial discretization referred to in the paper. At the broadest level are the *sweep regions*–these can be thought of as having dimensions like an assembly. Zooming in on a sweep region reveals several *coarse cells*–these can be thought of as having dimensions like a pin cell or quarter pin cell. Zooming in on a coarse cell reveals several *fine cells*–these can be thought of as having dimensions to describe the material regions within a pin cell. This is illustrated below in Fig. (1).

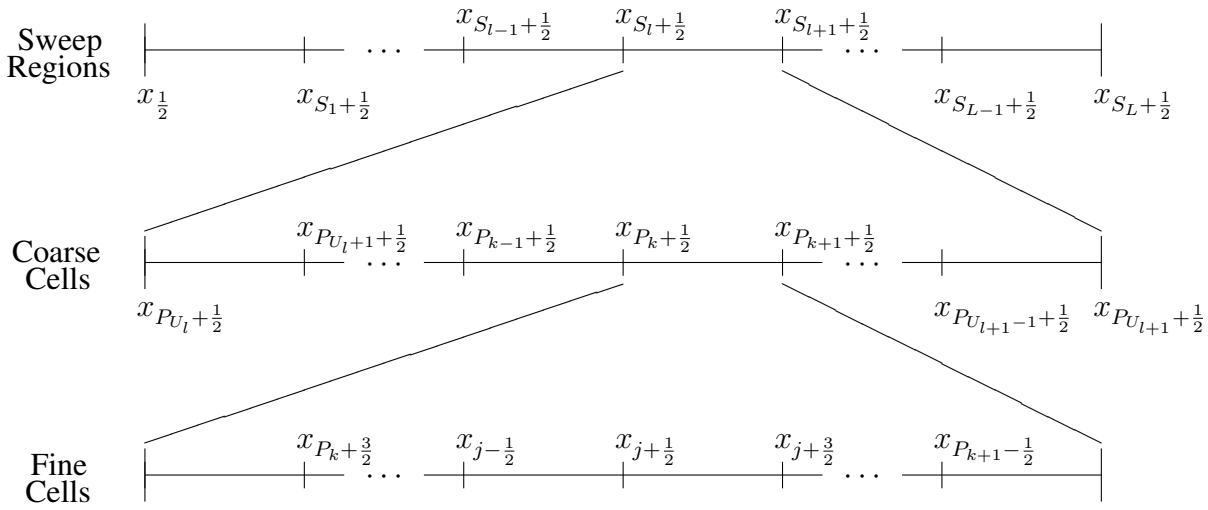

Figure 1: **Geometry Scales used for SDD-CMFD**

The algorithm begins with independent transport sweeps over the L spatially decoupled sweep regions. These sweeps generate fine cell-averaged scalar fluxes, coarse cell-edge partial currents, and angular fluxes on the sweep region boundaries–these are the primary unknowns in the discrete problem. This information is used to develop the coarse cell-homogenized coefficients for the CMFD solution. The CMFD acceleration occurs on the global system and provide updates to both the fine cell-averaged scalar fluxes and the angular fluxes on the sweep region boundaries. In this system, there are J fine cells, $K \leq J$ coarse cells, and $L \leq K$ sweep regions. Each coarse

cell $1 \leq k \leq K$ contains p_k fine cells. Each sweep region $1 \leq l \leq L$ contains u_l coarse cells and s_l fine cells. To relate the indices we use the conventions:

$$U_0 = S_0 = P_0 = 0 \ , \tag{2a}$$

$$U_l = \sum_{l'=1}^{l} u_{l'} = \text{the number of coarse cells in the first } l \text{ sweep regions} \ , \tag{2b}$$

$$S_l = \sum_{l'=1}^{l} s_{l'} = \text{the number of fine cells in the first } l \text{ sweep regions} \ , \tag{2c}$$

$$P_k = \sum_{k'=1}^{k} p_{k'} = \text{the number of fine cells in the first } k \text{ coarse cells} \ , \tag{2d}$$

$$U_L = K = \text{the total number of coarse cells} \ , \tag{2e}$$

$$S_L = P_K = J = \text{the total number of fine cells} \ . \tag{2f}$$

Using the familiar discrete ordinates approximation in angle and an arbitrary weighted diamond approximation in space on the fine cells, we discretize Eqs. (1) as follows:

$$\frac{\mu_n}{h_j}\left(\psi_{n,j+1/2} - \psi_{n,j-1/2}\right) + \sigma_{t,j}\psi_{n,j} = \frac{\sigma_{s,j}}{2}\sum_{m=1}^{N}\psi_{m,j}w_m + \frac{q_j}{2} \ , \tag{3a}$$

$$\psi_{n,j} = \left(\frac{1+\alpha_{n,j}}{2}\right)\psi_{n,j+1/2} + \left(\frac{1-\alpha_{n,j}}{2}\right)\psi_{n,j-1/2} \ , \tag{3b}$$

$$\psi_{n,1/2} = 0 \ , \quad \mu_n > 0 \ , \tag{3c}$$

$$\psi_{n,J+1/2} = \psi_{n',J+1/2} \ , \quad -\mu_{n'} = \mu_n < 0 \ . \tag{3d}$$

The notation in Eqs. (3) is standard. The subscript j, running from $1 \leq j \leq J$, denotes the (fine) spatial cell, which has width h_j, cross sections $\sigma_{t,j}$ and $\sigma_{s,j}$, and constant internal source q_j. The subscript n, running from $1 \leq n \leq N$, denotes the direction cosine of flight. The constants $\alpha_{n,j}$ determine the specific discretization method, e.g.

$$\alpha_{n,j} = \begin{cases} 0 & , \ \text{Diamond Difference} \ , \\ \coth\left(\frac{\sigma_{t,j}h_j}{2\mu_n}\right) - \left(\frac{\sigma_{t,j}h_j}{2\mu_n}\right)^{-1} & , \ \text{Step Characteristic} \ . \end{cases} \tag{4}$$

The SDD-CMFD method begins each iteration with L independent parallel transport sweeps within each sweep region. At the beginning of the ℓ^{th} iteration, the fine-mesh cell-averaged scalar fluxes $\phi_{0,j}^{(\ell)}$ and sweep region boundary angular fluxes $\Psi_{n,l+1/2}^{(\ell)}$ are assumed to be known, either from the previous iteration or from the initial guess if $\ell = 0$. Then the following version of Eqs. (3):

$$\begin{aligned}
&\frac{\mu_n}{h_j}\left(\psi_{n,j+1/2}^{(\ell+1/2)} - \Psi_{n,l-1/2}^{(\ell)}\right) + \sigma_{t,j}\psi_{n,j}^{(\ell+1/2)} = \frac{\sigma_{s,j}}{2}\phi_{0,j}^{(\ell)} + \frac{q_j}{2} \ , \quad \begin{cases} \mu_n > 0 \ , j = S_{l-1}+1 \ , \\ 2 \leq l \leq L \ , \end{cases} \\
&\frac{\mu_n}{h_j}\left(\Psi_{n,l+1/2}^{(\ell)} - \psi_{n,j-1/2}^{(\ell+1/2)}\right) + \sigma_{t,j}\psi_{n,j}^{(\ell+1/2)} = \frac{\sigma_{s,j}}{2}\phi_{0,j}^{(\ell)} + \frac{q_j}{2} \ , \quad \begin{cases} \mu_n < 0 \ , j = S_l \ , \\ 1 \leq l \leq L-1 \ , \end{cases} \\
&\frac{\mu_n}{h_j}\left(\psi_{n,j+1/2}^{(\ell+1/2)} - \psi_{n,j-1/2}^{(\ell+1/2)}\right) + \sigma_{t,j}\psi_{n,j}^{(\ell+1/2)} = \frac{\sigma_{s,j}}{2}\phi_{0,j}^{(\ell)} + \frac{q_j}{2} \ , \quad \begin{cases} \text{otherwise} \ , \end{cases}
\end{aligned} \tag{5a}$$

$$\psi_{n,j}^{(\ell+1/2)} = \left(\frac{1+\alpha_{n,j}}{2}\right)\psi_{n,j+1/2}^{(\ell+1/2)} + \left(\frac{1-\alpha_{n,j}}{2}\right)\Psi_{n,l-1/2}^{(\ell)} \ , \quad \begin{cases}\mu_n > 0 \ , j = S_{l-1}+1 \ , \\ 2 \leq l \leq L \ ,\end{cases}$$

$$\psi_{n,j}^{(\ell+1/2)} = \left(\frac{1+\alpha_{n,j}}{2}\right)\Psi_{n,l+1/2}^{(\ell)} + \left(\frac{1-\alpha_{n,j}}{2}\right)\psi_{n,j-1/2}^{(\ell+1/2)} \ , \quad \begin{cases}\mu_n < 0 \ , j = S_l \ , \\ 1 \leq l \leq L-1 \ ,\end{cases} \tag{5b}$$

$$\psi_{n,j}^{(\ell+1/2)} = \left(\frac{1+\alpha_{n,j}}{2}\right)\psi_{n,j+1/2}^{(\ell+1/2)} + \left(\frac{1-\alpha_{n,j}}{2}\right)\psi_{n,j-1/2}^{(\ell+1/2)} \ , \quad \begin{cases}\text{otherwise} \ ,\end{cases}$$

$$\psi_{n,1/2}^{(\ell+1/2)} = 0 \ , \quad \mu_n > 0 \ , \tag{5c}$$

$$\psi_{n,J+1/2}^{(\ell+1/2)} = \psi_{n',J+1/2}^{(\ell+1/2)} \ , \quad -\mu_{n'} = \mu_n < 0 \ , \tag{5d}$$

is solved by L independent, parallel transport sweeps for the $\psi^{(\ell+1/2)}$ unknowns. During these sweeps, the sweep region boundary angular fluxes $\psi_{n,S_l+1/2}^{(\ell+1/2)}$, cell-averaged fluxes and cell-edge currents are computed and stored:

$$\phi_{0,j}^{(\ell+1/2)} = \sum_{n=1}^{N} \psi_{n,j}^{(\ell+1/2)} w_n \ , \tag{6a}$$

$$\phi_{1,P_k+1/2}^{(\ell+1/2)} = \sum_{n=1}^{N} \mu_n \psi_{n,P_k+1/2}^{(\ell+1/2)} w_n \ . \tag{6b}$$

If we choose to implement no acceleration scheme, we implement a spatially-decomposed source iteration (SI) with the update equations:

$$\phi_{0,j}^{(\ell+1)} = \phi_{0,j}^{(\ell+1/2)} \ , \tag{7a}$$

$$\Psi_{n,l+1/2}^{(\ell+1)} = \psi_{n,S_l+1/2}^{(\ell+1/2)} \ . \tag{7b}$$

Later, we show that this method has convergence properties that are *at best* like SI (i.e. not rapid, but unconditionally stable). Instead, the method greatly benefits from the CMFD acceleration scheme. In fact, we can define our low-order equation identically to standard CMFD. To proceed, we introduce the notation

$$\sum_{j\in k} = \sum_{j=P_{k-1}+1}^{P_k} = \text{the sum over all fine cells } j \text{ in coarse cell } k \ , \tag{8}$$

and we define the coarse cell quantities:

$$H_k = \sum_{j\in k} h_j = \text{width of coarse cell } k \ , \tag{9a}$$

$$\Phi_{0,k} = \frac{1}{H_k}\sum_{j\in k} \phi_{0,j} h_j = \text{volume-averaged scalar flux in coarse cell } k \ , \tag{9b}$$

$$Q_k = \frac{1}{H_k}\sum_{j\in k} q_j h_j = \text{volume-averaged source in coarse cell } k \ , \tag{9c}$$

$$\Phi_{1,k+1/2} = \phi_{1,P_k+1/2} = \text{current on the right edge of coarse cell } k \ , \tag{9d}$$

$$\Sigma_{(\cdot),k} = \frac{1}{H_k}\sum_{j\in k}\sigma_{(\cdot),j}h_j = \text{volume-averaged cross section in coarse cell } k \ , \tag{9e}$$

$$\Sigma^{(\ell+1/2)}_{(\cdot),k} = \frac{\sum\limits_{j\in k}\sigma_{(\cdot),j}\phi^{(\ell+1/2)}_{0,j}h_j}{\sum\limits_{j\in k}\phi^{(\ell+1/2)}_{0,j}h_j} = \text{flux-weighted cross section in coarse cell } k \ . \tag{9f}$$

The coarse cell balance equation is:

$$\Phi^{(\ell+1)}_{1,k+1/2} - \Phi^{(\ell+1)}_{1,k-1/2} + \Sigma^{(\ell+1/2)}_{a,k}\Phi^{(\ell+1)}_{0,k}H_k = Q_kH_k \ . \tag{10}$$

The relation between the edge current and coarse cell fluxes is:

$$\Phi^{(\ell+1)}_{1,k+1/2} = -\tilde{D}^{(\ell+1/2)}_{k+1/2}\left(\Phi^{(\ell+1)}_{0,k+1} - \Phi^{(\ell+1)}_{0,k}\right) + \hat{D}^{(\ell+1/2)}_{k+1/2}\left(\Phi^{(\ell+1)}_{0,k+1} + \Phi^{(\ell+1)}_{0,k}\right) \ , \tag{11a}$$

$$\tilde{D}^{(\ell+1/2)}_{k+1/2} = \frac{2}{3\left(\Sigma^{(\ell+1/2)}_{t,k+1}H_{k+1} + \Sigma^{(\ell+1/2)}_{t,k}H_k\right)} \ , \tag{11b}$$

$$\hat{D}^{(\ell+1/2)}_{k+1/2} = \frac{\Phi^{(\ell+1/2)}_{1,k+1/2} + \tilde{D}^{(\ell+1/2)}_{k+1/2}\left(\Phi^{(\ell+1/2)}_{0,k+1} - \Phi^{(\ell+1/2)}_{0,k}\right)}{\Phi^{(\ell+1/2)}_{0,k+1} + \Phi^{(\ell+1/2)}_{0,k}} \ . \tag{11c}$$

The boundary conditions for this system are:

$$\Phi^{(\ell+1)}_{1,1/2} = -\tilde{D}^{(\ell+1/2)}_{1/2}\Phi^{(\ell+1)}_{0,1} + \hat{D}^{(\ell+1/2)}_{1/2}\Phi^{(\ell+1)}_{0,1} \ , \tag{12a}$$

$$\tilde{D}^{(\ell+1/2)}_{1/2} = \frac{2}{3\Sigma^{(\ell+1/2)}_{t,1}H_1 + 4} \ , \tag{12b}$$

$$\hat{D}^{(\ell+1/2)}_{1/2} = \frac{\Phi^{(\ell+1/2)}_{1,1/2} + \tilde{D}^{(\ell+1/2)}_{1/2}\Phi^{(\ell+1/2)}_{0,1}}{\Phi^{(\ell+1/2)}_{0,1}} \ , \tag{12c}$$

$$\Phi^{(\ell+1)}_{1,K+1/2} = 0 \ . \tag{12d}$$

With the standard CMFD implementation, the only change is now in the update equation. The update for the coarse cell is the standard update, but an additional update is defined for the sweep region boundaries:

$$\phi^{(\ell+1)}_{0,j} = \phi^{(\ell+1/2)}_{0,j}\left(\frac{\Phi^{(\ell+1)}_{0,k}}{\Phi^{(\ell+1/2)}_{0,k}}\right) \ , \ \ \forall\, j\in k, \ \ 1\le k\le K \ , \tag{13a}$$

$$\Psi^{(\ell+1)}_{n,l+1/2} = \psi^{(\ell+1/2)}_{n,S_l+1/2}\left(\frac{\Phi^{(\ell+1)}_{0,U_l+1/2} + 3\mu_n\Phi^{(\ell+1)}_{1,U_l+1/2}}{\Phi^{(\ell+1/2)}_{0,U_l+1/2} + 3\mu_n\Phi^{(\ell+1/2)}_{1,U_l+1/2}}\right) \ , \ \ 1\le l\le L-1 \ . \tag{13b}$$

Here, the coarse cell edge scalar fluxes are approximated from the coarse cell scalar fluxes in a sensible manner. The choice of the update ratio comes from the fact that the angular flux will have a P_1-like distribution in angle for diffusive problems. Alternative update options would include simply scaling with the scalar flux, or scaling with the appropriate partial current for left or right-going directions of flight.

3. LINEARIZATION AND FOURIER ANALYSIS

The method outlined in the previous section is non-linear and therefore cannot be Fourier analyzed directly. To determine the theoretical convergence properties of the method, it is necessary to first linearize it. We perform the linearization with the assumption of an infinite homogeneous system with the isotropic flat solution $\psi(x,\mu)=\frac{\Lambda}{2}$. The linearization terms are then:

$$\sigma_{t,j}\rightarrow\sigma\ ,\quad \sigma_{s,j}\rightarrow c\sigma\ ,\quad q_j\rightarrow\sigma_a\Lambda+\varepsilon q_j$$
$$\psi_{n,j+1/2}\rightarrow\frac{\Lambda}{2}+\varepsilon\psi_{n,j+1/2}\ ,\quad \psi_{n,j}\rightarrow\frac{\Lambda}{2}+\varepsilon\psi_{n,j}$$
$$\phi_{0,j}\rightarrow\Lambda+\varepsilon\phi_{0,j}\ ,\quad \Phi_{0,k}\rightarrow\Lambda+\varepsilon\Phi_{0,k}\ ,\quad \Phi_{1,k}\rightarrow\varepsilon\Phi_{1,k}$$

Applying this to Eqs.(5a,5b,10,11,13), and choosing a uniform spatial grid (for the Fourier analysis),

$$h_j\rightarrow h\ ,\quad u_l\rightarrow u\ ,\quad s_l\rightarrow s\ ,\quad p_k\rightarrow p\ ,$$

results in the following linearized form of the method:

$$\begin{aligned}
&\mu_n\left(\psi^{(\ell+1/2)}_{n,j+1/2}-\Psi^{(\ell)}_{n,l-1/2}\right)+\sigma h\psi^{(\ell+1/2)}_{n,j}=\frac{c\sigma h}{2}\phi^{(\ell)}_{0,j}+\frac{q_j}{2}\ ,\quad \begin{cases}\mu_n>0\ ,\\ j=s(l-1)+1\ ,\end{cases}\\
&\mu_n\left(\Psi^{(\ell)}_{n,l+1/2}-\psi^{(\ell+1/2)}_{n,j-1/2}\right)+\sigma h\psi^{(\ell+1/2)}_{n,j}=\frac{c\sigma h}{2}\phi^{(\ell)}_{0,j}+\frac{q_j}{2}\ ,\quad \begin{cases}\mu_n<0\ ,\\ j=sl\ ,\end{cases}\\
&\mu_n\left(\psi^{(\ell+1/2)}_{n,j+1/2}-\psi^{(\ell+1/2)}_{n,j-1/2}\right)+\sigma h\psi^{(\ell+1/2)}_{n,j}=\frac{c\sigma h}{2}\phi^{(\ell)}_{0,j}+\frac{q_j}{2}\ ,\quad \begin{cases}\text{otherwise}\ ,\end{cases}
\end{aligned}\tag{14a}$$

$$\begin{aligned}
&\psi^{(\ell+1/2)}_{n,j}=\left(\frac{1+\alpha_n}{2}\right)\psi^{(\ell+1/2)}_{n,j+1/2}+\left(\frac{1-\alpha_n}{2}\right)\Psi^{(\ell)}_{n,l-1/2}\ ,\quad \begin{cases}\mu_n>0\ ,\\ j=s(l-1)+1\ ,\end{cases}\\
&\psi^{(\ell+1/2)}_{n,j}=\left(\frac{1+\alpha_n}{2}\right)\Psi^{(\ell)}_{n,l+1/2}+\left(\frac{1-\alpha_n}{2}\right)\psi^{(\ell+1/2)}_{n,j-1/2}\ ,\quad \begin{cases}\mu_n<0\ ,\\ j=sl\ ,\end{cases}\\
&\psi^{(\ell+1/2)}_{n,j}=\left(\frac{1+\alpha_n}{2}\right)\psi^{(\ell+1/2)}_{n,j+1/2}+\left(\frac{1-\alpha_n}{2}\right)\psi^{(\ell+1/2)}_{n,j-1/2}\ ,\quad \begin{cases}\text{otherwise}\ ,\end{cases}
\end{aligned}\tag{14b}$$

$$\begin{aligned}
&-\frac{1}{3p\sigma h}\left(\delta\Phi^{(\ell+1)}_{0,k+1}-2\delta\Phi^{(\ell+1)}_{0,k}+\delta\Phi^{(\ell+1)}_{0,k-1}\right)+(1-c)\,p\sigma h\delta\Phi^{(\ell+1)}_{0,k}\\
&\qquad=c\sigma h\sum_{j\in k}\left(\phi^{(\ell+1/2)}_{0,j}-\phi^{(\ell)}_{0,j}\right)+\Upsilon^{+}_{k}+\Upsilon^{-}_{k}\ ,
\end{aligned}\tag{14c}$$

$$\Upsilon^{+}_{k}=\begin{cases}\displaystyle\sum_{\mu_n>0}|\mu_n|\left(\psi^{(\ell+1/2)}_{n,(s-1)l+1/2}-\Psi^{(\ell)}_{n,l-1/2}\right)w_n & ,\ k=u(l-1)+1\ ,\\ 0 & ,\ \text{otherwise}\ ,\end{cases}\tag{14d}$$

$$\Upsilon^{-}_{k}=\begin{cases}\displaystyle\sum_{\mu_n<0}|\mu_n|\left(\psi^{(\ell+1/2)}_{n,sl+1/2}-\Psi^{(\ell)}_{n,l+1/2}\right)w_n & ,\ k=ul\ ,\\ 0 & ,\ \text{otherwise}\ ,\end{cases}\tag{14e}$$

$$\phi_{0,j}^{(\ell+1)} = \phi_{0,j}^{(\ell+1/2)} + \delta\Phi_{0,k}^{(\ell+1)} \ , \ \ \forall\, j \in k, \ \ 1 \le k \le K \ , \tag{14f}$$

$$\Psi_{n,l+1/2}^{(\ell+1)} = \psi_{n,sl+1/2}^{(\ell+1/2)} + \frac{1}{2}\left(\delta\Phi_{0,U_l+1/2}^{(\ell+1)} + 3\mu_n\delta\Phi_{1,U_l+1/2}^{(\ell+1)}\right) \ , \ \ 1 \le l \le L-1 \ , \tag{14g}$$

where the sweep region edge acceleration terms are:

$$\Phi_{0,U_l+1/2}^{(\ell+1)} = \frac{1}{2}\left(\Phi_{0,U_l+1}^{(\ell+1)} + \Phi_{0,U_l}^{(\ell+1)}\right) \ , \ \ \Phi_{1,U_l+1/2}^{(\ell+1)} = -\frac{1}{3\sigma hp}\left(\Phi_{0,U_l+1}^{(\ell+1)} - \Phi_{0,U_l}^{(\ell+1)}\right) \ .$$

We choose the following ansatz, which eliminates aliasing between the fine cell and coarse cell modes and results in a system of equations with substantially fewer exponential terms. Let j' denote the (integer) label for any cell in the infinite system; $-\infty < j' < \infty$. Also, let j be a positive integer satisfying $1 \le j \le p$, let k be a positive integer satisfying $1 \le k \le u$, and let l be an integer such that

$$j' = (k'-1)\,p + j \ ,$$
$$k' = (l-1)\,u + k \ .$$

Then for each j', (i) j, k, and l are unique, (ii) l labels the sweep region and k labels the coarse cell within which cell j' resides, and (iii) j labels the position within coarse cell k and sweep region l at which fine cell j' resides. The Fourier ansatz can now be stated as:

$$\begin{aligned}
q_j &= 0 \ , \\
\psi_{n,j'+1/2}^{(\ell+1/2)} &= \omega^\ell d_{n,j+(k-1)p} e^{i\lambda\sigma x_l} \ , \mu_n > 0 \ , \\
\psi_{n,j'-1/2}^{(\ell+1/2)} &= \omega^\ell d_{n,j+(k-1)p} e^{i\lambda\sigma x_l} \ , \mu_n < 0 \ , \\
\psi_{n,j'}^{(\ell+1/2)} &= \omega^\ell a_{n,j+(k-1)p} e^{i\lambda\sigma x_l} \ , \\
\phi_{0,j'}^{(\ell)} &= \omega^\ell g_{j+(k-1)p} e^{i\lambda\sigma x_l} \ , \\
\Psi_{n,l+1/2}^{(\ell)} &= \omega^\ell D_n e^{i\lambda\sigma x_l} \ , \mu_n < 0 \ , \\
\Psi_{n,l-1/2}^{(\ell)} &= \omega^\ell D_n e^{i\lambda\sigma x_l} \ , \mu_n > 0 \ , \\
\delta\Phi_{0,k'}^{(\ell+1)} &= \omega^\ell F_k e^{i\lambda\sigma x_l} \ ,
\end{aligned}$$

Inserting this ansatz into Eqs. (14), we obtain:

$$\begin{aligned}
\mu_n\left(d_{n,j} - D_n\right) + \sigma h a_{n,j} &= \frac{c\sigma h}{2} g_j \ , \ \ \mu_n > 0 \ , \ \ j = 1 \ , \\
\mu_n\left(D_n - d_{n,j}\right) + \sigma h a_{n,j} &= \frac{c\sigma h}{2} g_j \ , \ \ \mu_n < 0 \ , \ \ j = s \ , \\
\mu_n\left(d_{n,j+1} - d_{n,j}\right) + \sigma h a_{n,j} &= \frac{c\sigma h}{2} g_j \ , \ \ 1 \le j \le s-1 \ ,
\end{aligned} \tag{15a}$$

$$\begin{aligned}
a_{n,j} &= \left(\frac{1+\alpha_n}{2}\right) d_{n,j} + \left(\frac{1-\alpha_n}{2}\right) D_n \ , \ \ \mu_n > 0 \ , \ \ j = 1 \ , \\
a_{n,j} &= \left(\frac{1+\alpha_n}{2}\right) D_n + \left(\frac{1-\alpha_n}{2}\right) d_{n,j} \ , \ \ \mu_n < 0 \ , \ \ j = s \ , \\
a_{n,j} &= \left(\frac{1+\alpha_n}{2}\right) d_{n,j+1} + \left(\frac{1-\alpha_n}{2}\right) d_{n,j} \ , \ \ 1 \le j \le s-1 \ ,
\end{aligned} \tag{15b}$$

$$-\frac{1}{3p\sigma h}\left((1-\delta_{k,u})F_{k+1}+\delta_{k,u}F_1e^{i\lambda s\sigma h}-2F_k+(1-\delta_{k,1})F_{k-1}+\delta_{k,1}F_ue^{-i\lambda s\sigma h}\right)$$
$$+(1-c)\,p\sigma hF_k=c\sigma h\sum_{j=p(k-1)+1}^{pk}\left(\sum_{n=1}^{N}w_na_{n,j}-g_j\right) \tag{15c}$$
$$+\delta_{k,1}\sum_{\mu_n>0}|\mu_n|\left(d_{n,s}e^{-i\lambda s\sigma h}-D_n\right)w_n+\delta_{k,u}\sum_{\mu_n<0}|\mu_n|\left(d_{n,1}e^{i\lambda s\sigma h}-D_n\right)w_n\ .$$

Here, $\delta_{k,k'}$ is the Kronecker delta. The Fourier modes of the update equation are:

$$\omega g_j=\sum_{n=1}^{N}w_na_{n,j}+F_k\ ,\quad p(k-1)+1\le j\le pk,\quad 1\le k\le u\ , \tag{15d}$$

$$\omega D_n=d_{n,s}e^{-i\lambda s\sigma h}+\frac{1}{2}\left(\frac{F_1+F_ue^{-i\lambda s\sigma h}}{2}-\frac{\mu_n}{p\sigma h}\left(F_1-F_ue^{-i\lambda s\sigma h}\right)\right)\ ,\quad \mu_n>0\ , \tag{15e}$$

$$\omega D_n=d_{n,1}e^{i\lambda s\sigma h}+\frac{1}{2}\left(\frac{F_1e^{i\lambda s\sigma h}+F_u}{2}-\frac{\mu_n}{p\sigma h}\left(F_1e^{i\lambda s\sigma h}-F_u\right)\right)\ ,\quad \mu_n<0\ . \tag{15f}$$

The eigenvalues $1\le\omega_t\le s+N$ of this system of equations are solved numerically; the spectral radius is then calculated as

$$\rho=\sup_{\lambda}\sup_{1\le t\le s+N}\left|\omega_t(\lambda)\right|\ . \tag{16}$$

4. RESULTS

The following figures show the spectral radius as determined by Fourier Analysis and numerical implementation of the method. Figures (2)-(4) show that without SDD-CMFD acceleration, this style of spatial domain decomposition is as rapid as source iteration *at best*.

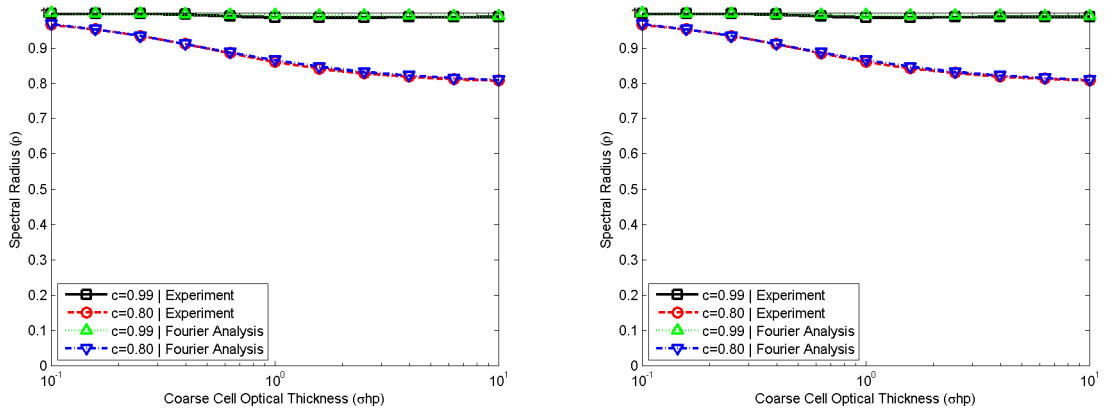

(a) $p=1$ (b) $p=2$

Figure 2: Spectral Radius of SDD-SI with $u=1$

The spectral radius is estimated experimentally by fitting a trend-line to the residuals of a few iterates after the initial estimate.

From the results shown in Fig. (2), it is clear that this kind of spatial domain decomposition requires acceleration of not only the scattering source but also the sweep region boundary fluxes. When the sweep regions are optically thick, the scattering source is the iteration bottleneck, whereas when they are optically thin, the sweep region boundary fluxes limit the convergence rate. We also note that the Fourier Analysis matches the computational results very well.

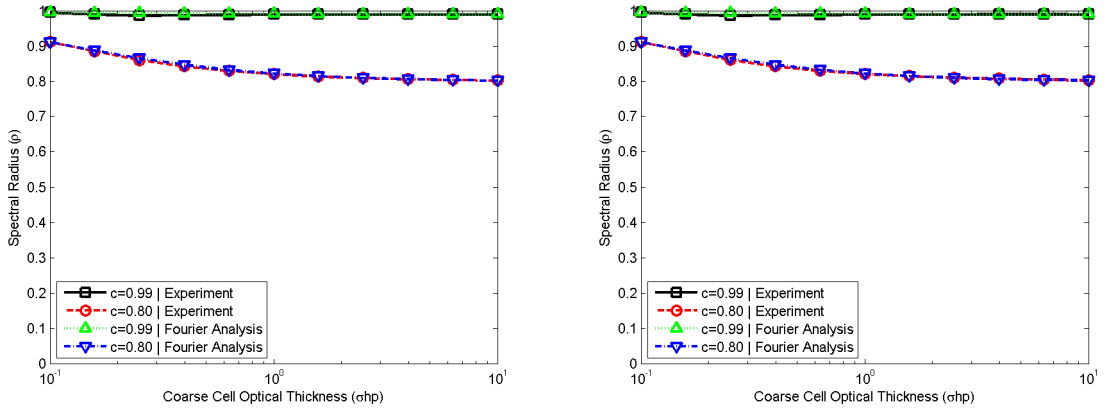

(a) $p = 1$ (b) $p = 2$

Figure 3: Spectral Radius of SDD-SI with $u = 4$

Here, we see that by increasing the number of coarse cells in a sweep region (and thereby the optical thickness), the sweep region boundaries become less dominant as the iterative quantity limiting convergence.

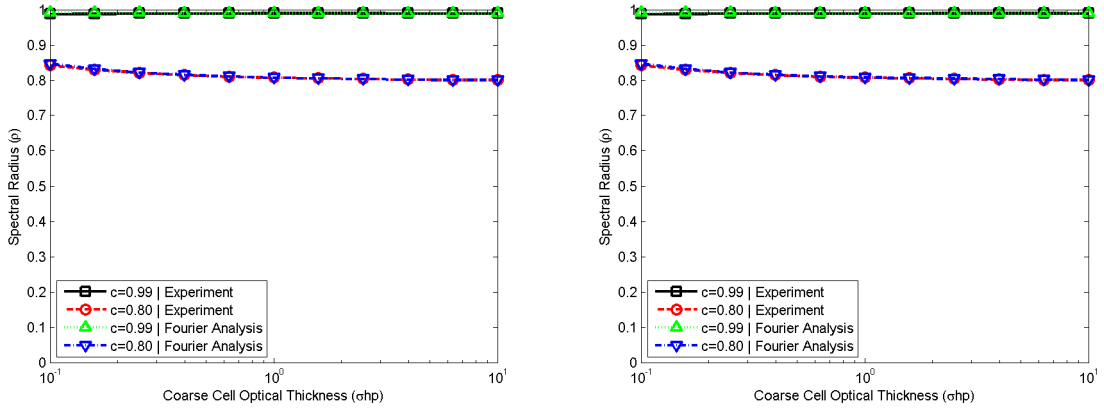

(a) $p = 1$ (b) $p = 2$

Figure 4: Spectral Radius of SDD-SI with $u = 16$

Again increasing u reduces the spectral radius when the sweep region boundaries limit convergence.

In Figures (5) - (9), SDD-CMFD is enabled, including the sweep region boundary angular flux update of Eq. (13b). Although not required, this update does reduce the spectral radius of the method by a value of about 0.1 when the coarse cells are less than one mean free path thick. For brevity, we do not include plots of the spectral radius with the scattering source acceleration enabled and the sweep region boundary angular flux acceleration disabled.

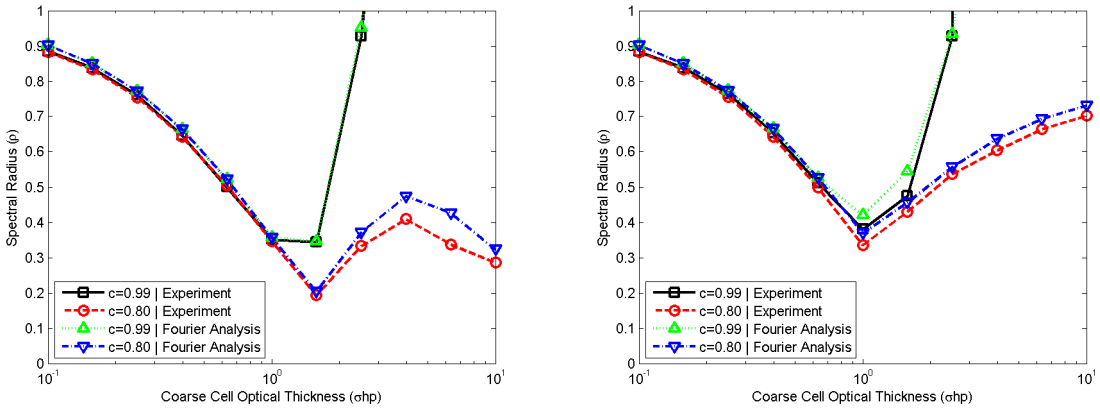

(a) $p = 1$ (b) $p = 2$

Figure 5: Spectral Radius of SDD-CMFD with $u = 1$

With SDD-CMFD enabled, the problems converge at a substantially improved rate. When the coarse cells are at least one mean free path thick, the convergence rate of the method is essentially identical to CMFD. However, when optically thin, the fluxes on the sweep boundaries limit the rapidity of convergence. The Fourier Analysis adequately predicts the convergence properties; the experimental estimates are smaller than the theoretical estimates of the spectral radius due to both finite problem size and the solution not quite reaching the asymptotic mode of convergence.

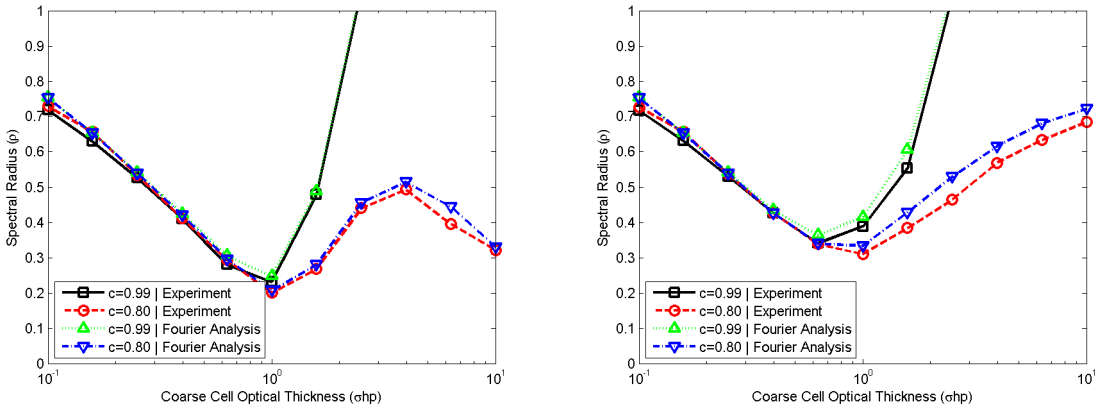

(a) $p = 1$ (b) $p = 2$

Figure 6: Spectral Radius of SDD-CMFD with $u = 4$

By increasing the number of coarse cells in a sweep region for a given coarse cell optical thickness, we automatically increase the sweep region optical thickness. This has the effect of increasing the spectral radius when the sweep region boundary fluxes limit the convergence.

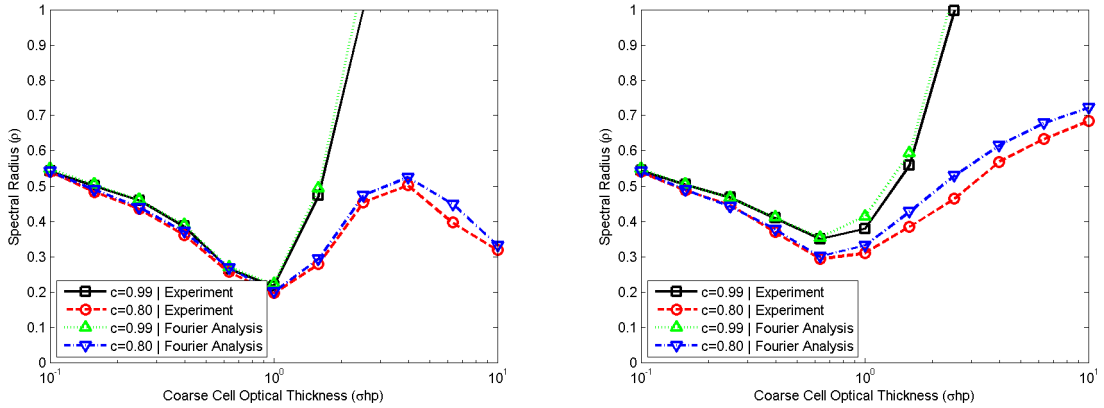

(a) $p = 1$ (b) $p = 2$

Figure 7: Spectral Radius of SDD-CMFD with $u = 16$

Once more, increasing u decreases the spectral radius when the coarse cells are optically thin. Some of the computational spectral radii are estimated as being larger than the Fourier Analysis estimates, but this is again due to the means of estimated the spectral radius described earlier.

From the results thus far presented, it is clear that the method performs well when the coarse cells do not exceed one mean free path, and it performs best when the sweep region is optically thick. The following figures show that the benefits of increasing the sweep region optical thickness reach an asymptotic limit.

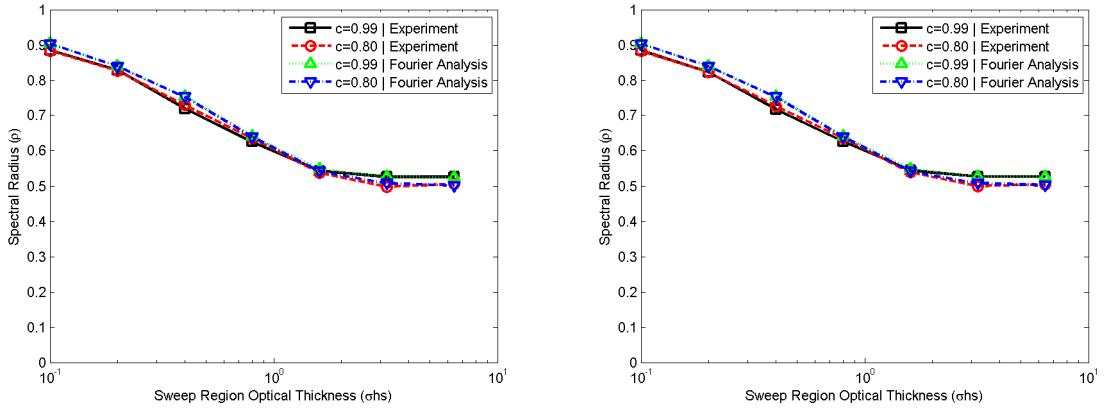

(a) $p = 1$ (b) $p = 2$

Figure 8: Spectral Radius of SDD-CMFD with $\sigma hp = 0.1$

According to these results, the SDD-CMFD method reaches an asymptotic spectral radius when the sweep region optical thickness is at least approximately two mean free paths.

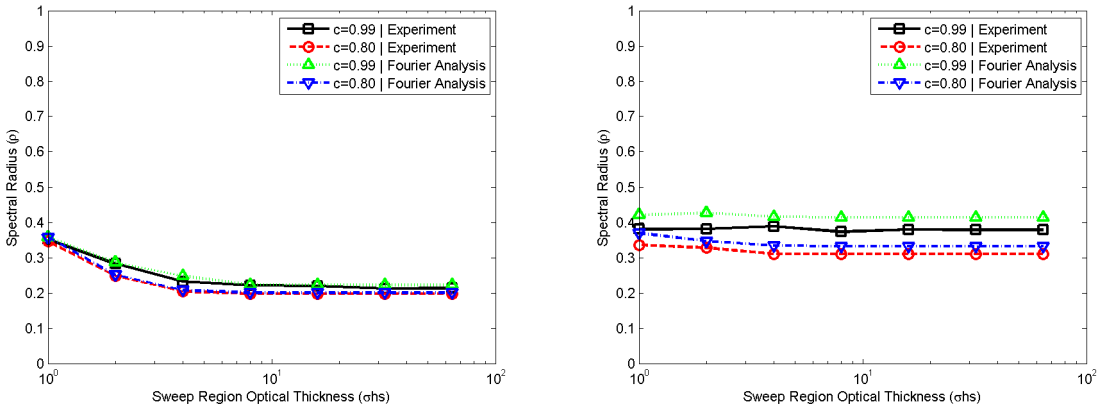

(a) $p = 1$ (b) $p = 2$

Figure 9: Spectral Radius of SDD-CMFD with $\sigma hp = 1.0$

Again, a sweep region of two mean free paths or larger yields the best results. In comparison, standard CMFD has rapid convergence if the coarse cells are less than one mean free path thick. The SDD-CMFD method has the same rapid convergence rate as standard CMFD if coarse cells are also less than one mean free path thick and, additionally, the sweep regions are greater than two mean free paths thick. In practice, SDD-CMFD will converge if a coarse cell is a pin cell or quarter pin cell and the sweep regions contain two or more pin cells.

5. CONCLUSIONS

In this paper, we have presented a spatial domain decomposition method that utilizes CMFD to accelerate both the scattering source and sub-domain boundary angular fluxes. We have analyzed this method both theoretically and computationally to determine that it is an efficient acceleration method (similar to standard CMFD) with the added benefit of a clear path to introduce parallelism to the sweeping process. Like standard CMFD, this method is non-linear and can be adapted to solve eigenvalue problems in addition to fixed source problems. In contrast, this method requires the additional storage of angular fluxes on sub-domain boundaries. However, on a distributed memory system (to take advantage of the parallelism) this should be a minor issue.

The SDD-CMFD method can also be expanded upon by allowing for internal acceleration on each of the sweep regions. This would further improve parallelization by minimizing message passing for the global problem. For multi-group problems, this approach would also help independently converge the energy spectrum locally. Our future work includes implementing this method in a three-dimensional, multi-group framework for realistic reactor problems.

ACKNOWLEDGEMENTS

We gratefully acknowledge support of this research through the U.S. Department of Energy NEUP grant DE-AC07-05ID14517.

REFERENCES

[1] J.W. Fischer, Y.Y. Azmy, "Comparison via parallel performance models of angular and spatial domain decompositions for solving neutral particle transport problems," *Progress in Nuclear Energy*, **49**, pp. 37-60 (2007).

[2] S. Van Criekingen, F. Nataf, P. Havé, "PARAFISH: A parallel FE-P_N neutron transport solver based on domain decomposition," *Annals of Nuclear Energy*, **38**, pp. 145-150 (2011).

[3] M.L. Adams, W.R. Martin, "Boundary Projection Acceleration: A New Approach to Synthetic Acceleration of Transport Calculations," *Nuclear Science and Engineering*, **100**, pp. 177-189 (1988).

[4] H. Zhang, H. Wu, L. Cao, "An Acceleration Technique for 2D MOC based on Krylov Subspace and Domain Decomposition Methods," *Annals of Nuclear Energy*, **38**, pp. 2742-2751 (2011).

[5] S. Santandrea, "An Integral Multidomain DP_N Operator as Acceleration Tool for the Method of Characteristics in Unstructured Meshes," *Nuclear Science and Engineering*, **155**, pp. 223-235 (2007).

[6] M. Yavuz, E.W. Larsen, "Spatial Domain Decomposiition for Neutron Transport Problems," *Transport Theory and Statistical Physics*, **18**, pp. 205-219 (1989).

[7] M.L. Adams and E.W. Larsen, "Fast Iterative Methods for Discrete-Ordinates Particle Transport Calculations," *Progress in Nuclear Energy*, **40**, pp. 3-159 (2002).

[8] H.J. Kopp, "Synthetic Method Solution of the Transport Equation," *Nuclear Science and Engineering*, **17**, p. 65 (1963).

[9] R. Alcouffe, "Diffusion Synthetic Acceleration Methods for the Diamond-Differenced Discrete-Ordinates Equations," *Nuclear Science and Engineering*, **64**, p. 344 (1977).

[10] E.W. Larsen, "Unconditionally Stable Diffusion-Synthetic Acceleration Methods for the Slab Geometry Discrete-Ordinates Equations. Part I: Theory," *Nuclear Science and Engineering*, **82**, p. 47 (1982).

[11] D.R. McCoy and E.W. Larsen, "Unconditionally Stable Diffusion-Synthetic Acceleration Methods for the Slab Geometry Discrete-Ordinates Equations. Part II: Numerical Results," *Nuclear Science and Engineering*, **82**, p. 64 (1982).

[12] K. Smith, "Nodal Method Storage Reduction by Nonlinear Iteration," *Transactions of the American Nuclear Society*, **44**, p. 265 (1983).

[13] K. Smith, "Assembly Homogenization Techniques for Light Water Reactor Analysis," *Progress in Nuclear Energy*, **17**, pp. 303-335 (1986).

[14] N.Z. Cho and C.J. Park, "A Comparison of Coarse Mesh Rebalance and Coarse Mesh Finite Difference Accelerations for the Neutron Transport Calculations," *Proceedings of the Conference on Nuclear, Mathematical, and Computational Sciences: a Century in Review, a Century Anew*, Gatlinburg, Tennessee, April 6-11, 2003, American Nuclear Society (2003). [CD-ROM]

[15] Z. Zhong, T.J. Downar, Y. Xu, M.D. DeHart, and K.T. Clarno, "Implementation of Two-Level Coarse-Mesh Finite Difference Acceleration in an Arbitrary Geometry, Two-Dimensional Discrete Ordinates Transport Method," *Nuclear Science and Engineering*, **158**, p. 289 (2008).

2D/1D APPROXIMATIONS TO THE 3D NEUTRON TRANSPORT EQUATION. I: THEORY

Blake W. Kelley and Edward W. Larsen
Department of Nuclear Engineering and Radiological Sciences
University of Michigan, Ann Arbor, MI 48109
kelleybl@umich.edu; edlarsen@umich.edu

ABSTRACT

A new class of "2D/1D" approximations is proposed for the 3D linear Boltzmann equation. These approximate equations preserve the exact transport physics in the radial directions x and y and diffusion physics in the axial direction z. Thus, the 2D/1D equations are more accurate approximations of the 3D Boltzmann equation than the conventional 3D diffusion equation. The 2D/1D equations can be systematically discretized, to yield accurate simulation methods for 3D reactor core problems. The resulting solutions will be more accurate than 3D diffusion solutions, and less expensive to generate than standard 3D transport solutions. In this paper, we (i) show that the simplest 2D/1D equation has certain desirable properties, (ii) systematically discretize this equation, and (iii) derive a stable iteration scheme for solving the discrete system of equations. In a companion paper [1], we give numerical results that confirm the theoretical predictions of accuracy and iterative stability.

Key Words: 3D neutron transport simulations, diffusion approximation, Fourier analysis

1. INTRODUCTION

The term "2D/1D" has been used to describe recently-developed computational methods for solving 3D whole-core neutronics problems in which the (1D) axial and (2D) radial derivative terms are approximated differently. These methods were originally proposed and implemented by two groups in Korea during 2002-2007 [2–12]. One group, located at KAIST (N.Z. Cho, G.S. Lee, C.J. Park, and colleagues), developed the "2D/1D Fusion" method for the CRX code [3–5, 8, 9, 12]. In this method, the 3D Boltzmann transport equation is solved by discretizing the radial derivative terms on a "fine" radial grid and the axial derivative term on a "coarse" radial grid. The other group, located at at KAERI (J.Y. Cho, H.G. Joo, K.S. Kim, and S.Q. Zee and colleagues), developed a different "planar MOC solution-based 3D heterogeneous core method" for the DeCART code [2, 6, 10, 11]. This method also discretizes the axial derivative term using a "coarse" radial grid, but most importantly, it simplifies this term in a way that (i) is accurate for problems in which the axial leakage can be represented by Fick's Law, and (ii) offers major advantages for parallel-architecture computers. In some publications, the KAERI method was simply called "2D/1D" [6]. In the present paper, we refer to the KAIST method in CRX by its original "2D/1D Fusion" name, and we refer to the KAERI method in DeCART by its abbreviated "2D/1D" name. The purpose of this paper is to outline a systematic mathematical theory for the 2D/1D methodology developed at KAERI for DeCART.

DeCART (Deterministic Core Analysis Based on Ray Tracing) was originally developed under an I-NERI project between KAERI and ANL. An early version of DeCART was acquired by the University of Michigan (UM), where it has been extensively used in the DOE CASL project. This version has certain deficiencies – in particular, a failure to converge for small axial cell widths Δ_z. In more recent versions of DeCART, the staff at KAERI and ANL have "suppressed" these instabilities. However, in these revisions, the cause of the original iterative instabilities and other basic questions were not answered.

The use of (the UM version of) DeCART has demonstrated that for problems in which DeCART converges, it has major computational advantages over other 3D Discrete Ordinates (DO) or Method of

Characteristics (MOC) codes. Unfortunately, the failure of DeCART to converge for small Δ_z and the lack of a mathematical foundation for the 2D/1D methodology have been major concerns. Nonetheless, discussions took place at UM on the desirability of developing a new 3D reactor physics code that would employ a more robust (but then nonexistent) 2D/1D methodology. To accomplish this, we decided to try to develop a mathematical foundation for the 2D/1D methodology in DeCART – in order to better understand this methodology, and to suggest systematic ways to improve it. This paper is the first public statement of our results – for monoenergetic problems in classically "diffusive" media. (Our theoretical results cover a wider and more interesting range of lattice problems. However, our implementation and testing of the 2D/1D method in the new MPACT (Michigan Parallel Characteristics Transport Code) code [13] is ongoing. In the present paper, we only discuss problems for which numerical results can now be given; these results are presented in a companion paper [1].)

Our goal in this paper and [1] is to demonstrate that stable and accurate 2D/1D methods similar to the DeCART method can be systematically derived from a new second-order, integrodifferential "2D/1D equation." The proposed 2D/1D equation and the classic 3D diffusion equation have a similar status: both approximate (simplify) the 3D linear Boltzmann equation. The 2D/1D equation is (i) less expensive to solve than the 3D transport equation, (ii) more complicated and expensive to solve than the 3D diffusion equation, and (iii) well-approximates the 3D Boltzmann equation over a much larger range of problems than the diffusion equation. Specifically: *the 2D/1D equation preserves exact transport physics in the radial directions (x and y), but it uses approximate diffusion physics in the axial direction z.*

We systematically discretize the 2D/1D equation to obtain a system of discrete equations whose solution converges to the exact 2D/1D solution as the grid (of all independent variables) becomes increasingly fine. We also derive iterative methods for solving the discrete system and analyze these methods by Fourier analysis techniques. This analysis makes it possible to predict the performance of an iterative method before it is implemented, and to avoid iteration methods that are unstable.

In this paper, we (i) derive the "simplest" 2D/1D equation, (ii) systematically discretize this equation in a straightforward manner, and (iii) develop a simple stable iteration strategy for solving the discretized equations. (All aspects of the work presented here are as "simple" as possible.) In our companion paper, we present numerical results that validate the theoretical predictions, and that demonstrate the accuracy of the 2D/1D solutions by comparing them to 3D transport and 3D diffusion solutions [1].

The remainder of this paper is organized as follows. In Section 2 we propose several 2D/1D equations that approximate the linear Boltzmann equation in a manner consistent with the spirit of the method in DeCART. In Section 3 we show some basic properties of this "simplest" 2D/1D equation.

In Section 4 we systematically discretize the simplest 2D/1D equation, and in Section 5 we propose an iteration method to solve the discrete equations. This method is related to the original iterative method in DeCART, but the new method has a modification that renders it stable. Section 6 concludes this paper with a discussion, covering (i) the generalization of the "simplest" 2D/1D equation discussed here to more accurate approximations, (ii) the generalization of 2D/1D equations to realistic reactor core lattices, and finally, (iii) the relationship between the "KAERI-like" 2D/1D methods described in this paper and the KAIST 2D/1D Fusion method implemented in CRX.

2. THE 2D/1D EQUATION

The derivation of the 2D/1D equation begins with the linear 3D Boltzmann transport equation formulated on a "cylindrical" system V, consisting of points $\boldsymbol{x} = (x, y, z)$ with the *radial* variables $(x, y) \in R$ (a convex 2D region), and the *axial* variable z in the interval $0 \leq z \leq Z$. (Aside from being convex, R is

arbitrary; in [1], R is taken to be a square.)

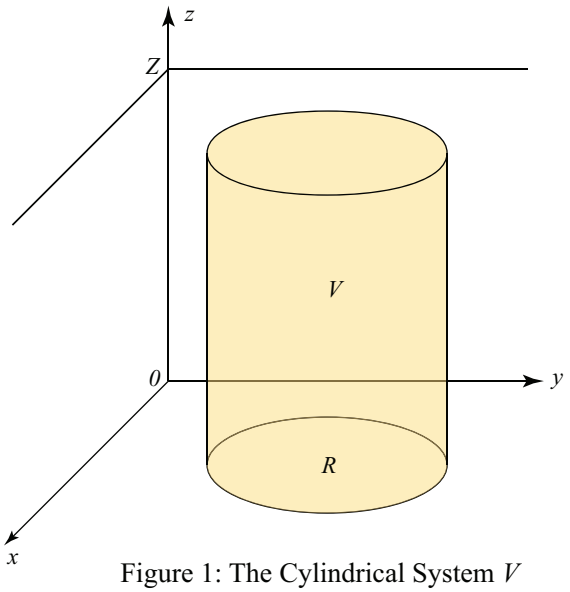

Figure 1: The Cylindrical System V

For simplicity, we assume monoenergetic transport with isotropic scattering and vacuum boundaries. Using the standard notation:

$$\boldsymbol{\Omega} = (\Omega_x, \Omega_y, \Omega_z) = (\sqrt{1-\mu^2}\cos\omega, \sqrt{1-\mu^2}\sin\omega, \mu) \ , \tag{1}$$

we have the fixed-source transport equation:

$$\boldsymbol{\Omega}\cdot\boldsymbol{\nabla}\psi(\boldsymbol{x},\boldsymbol{\Omega}) + \Sigma_t(\boldsymbol{x})\psi(\boldsymbol{x},\boldsymbol{\Omega}) = \frac{\Sigma_s(\boldsymbol{x})}{4\pi}\int_{4\pi}\psi(\boldsymbol{x},\boldsymbol{\Omega}')d\Omega' + \frac{Q(\boldsymbol{x})}{4\pi} \ , \quad \boldsymbol{x}\in V \ , \ \boldsymbol{\Omega}\in 4\pi \ , \tag{2a}$$

with the vacuum boundary condition:

$$\psi(\boldsymbol{x},\boldsymbol{\Omega}) = 0 \ , \quad \boldsymbol{x}\in\partial V \ , \ \boldsymbol{\Omega}\cdot\boldsymbol{n} < 0 \ . \tag{2b}$$

In typical light water reactors, the cross sections are highly complicated functions of the radial variables x and y, but are relatively simple (almost constant) functions of the axial variable z. *This suggests that the z-dependence of ψ is weak, and that the axial leakage term $\mu\partial\psi/\partial z$ in Eq. (2a) can be approximated advantageously, with a minimal loss of accuracy.* Thus, we write Eq. (2a) as:

$$\sqrt{1-\mu^2}\left(\cos\omega\frac{\partial\psi}{\partial x} + \sin\omega\frac{\partial\psi}{\partial y}\right) + \frac{\partial F}{\partial z} + \Sigma_t\psi = \frac{1}{4\pi}\big(\Sigma_s\phi + Q\big) \ , \tag{3}$$

where

$$F(\boldsymbol{x},\boldsymbol{\Omega}) = \mu\psi(\boldsymbol{x},\boldsymbol{\Omega}) \ , \tag{4a}$$

$$\phi(\boldsymbol{x}) = \int_{4\pi}\psi(\boldsymbol{x},\boldsymbol{\Omega}')d\Omega' \ , \tag{4b}$$

and we consider various approximations to F.

If ψ on the right side of Eq. (4a) is approximated by its classic diffusion approximation, the axial leakage term becomes:

$$\frac{\partial F}{\partial z} \approx \frac{\partial}{\partial z}\frac{\mu}{4\pi}\left[\phi - \frac{1}{\Sigma_t}\left(\Omega_x\frac{\partial\phi}{\partial x} + \Omega_y\frac{\partial\phi}{\partial y} + \mu\frac{\partial\phi}{\partial z}\right)\right] \ . \tag{5a}$$

In a simpler approximation, the radial derivative terms in Eq. (5a) are discarded, yielding:

$$\frac{\partial F}{\partial z} \approx \frac{\partial}{\partial z}\frac{\mu}{4\pi}\left(\phi - \frac{\mu}{\Sigma_t}\frac{\partial \phi}{\partial z}\right) \ . \tag{5b}$$

In an even simpler approximation, the right side of Eq. (5b) is replaced by its zero-th angular moment, giving:

$$\frac{\partial F}{\partial z} \approx -\frac{\partial}{\partial z}\frac{D}{4\pi}\frac{\partial \phi}{\partial z} \ , \tag{5c}$$

where $D = 1/3\Sigma_t$. The progression from Eq. (5a) to Eq. (5b) to Eq. (5c) becomes increasingly simple and (presumably) less accurate. In this paper we consider the simplest of these approximations, Eq. (5c). Using this in Eq. (3), we obtain the following "simplest" 2D/1D equation:

$$\boxed{\sqrt{1-\mu^2}\left(\cos\omega\frac{\partial \psi}{\partial x} + \sin\omega\frac{\partial \psi}{\partial y}\right) - \frac{\partial}{\partial z}\frac{D}{4\pi}\frac{\partial \phi}{\partial z} + \Sigma_t\psi = \frac{1}{4\pi}\Big(\Sigma_s\phi + Q\Big)} \ . \tag{6}$$

The vacuum boundary conditions for Eq. (6) remain the standard transport vacuum boundary condition on the "sides" of ∂V:

$$\psi(\boldsymbol{x}, \boldsymbol{\Omega}) = 0 \ , \quad (x,y) \in \partial R \ , \ 0 < z < Z \ , \ \boldsymbol{\Omega}\cdot\boldsymbol{n} < 0 \ , \tag{7a}$$

but become "diffusion" boundary conditions on the "top" and "bottom" of V:

$$\phi(x,y,0) - 2D\frac{\partial \phi}{\partial z}(x,y,0) = 0 \ , \quad (x,y) \in R \ , \tag{7b}$$

$$\phi(x,y,Z) + 2D\frac{\partial \phi}{\partial z}(x,y,Z) = 0 \ , \quad (x,y) \in R \ . \tag{7c}$$

The second-order integrodifferential 2D/1D Eq. (6) approximates the linear Boltzmann equation only in its axial derivative term; here this is done using the standard diffusion approximation. The radial derivative terms in Eq. (6) are not approximated, and – unlike the standard diffusion equation – the angular variable is not eliminated from the 2D/1D equation.

3. BASIC PROPERTIES OF THE 2D/1D EQUATION

Here we discuss some basic properties of the 2D/1D Eq. (6).

1. *Conjecture: The 2D/1D equation with vacuum boundary conditions [Eqs. (6) and (7)] has a unique, positive solution.* Eq. (6) is an unfamiliar (second-order integrodifferential) equation which, to our knowledge, has not been studied previously. Our work has shown theoretically and experimentally that discrete versions of Eqs. (6) and (7) have unique solutions, which (experimentally) are positive. Unfortunately, proving the stated conjecture for the continuous 2D/1D equation is beyond our capability at this time. To proceed, we assume that the conjecture is true. (Nothing in our analysis or our numerical simulations suggests that the conjecture is untrue.)

2. *The 2D/1D equation preserves 2D radial transport.* If any problem is considered in which the cross sections and source are independent of z, and the boundary conditions (7b) and (7c) are replaced by reflecting boundary conditions:

$$\frac{\partial \phi}{\partial z}(x,y,0) = 0 = \frac{\partial \phi}{\partial z}(x,y,Z) \ , \quad (x,y) \in R \ ,$$

then ψ is independent of z. In this case, the 2D/1D Eq. (6) directly reduces to the 2D Boltzmann equation. Thus, for problems with no axial dependence, the 2D/1D equation and the 2D Boltzmann equation are identical.

3. *The 2D/1D equation preserves 1D axial diffusion.* If any problem is considered in which the cross sections and source are independent of x and y, and the boundary condition (7a) is replaced by a reflecting boundary condition, then ψ is independent of x and y. In this case, Eqs. (6), (7b), and (7c) reduce to:

$$-\frac{\partial}{\partial z}\frac{D}{4\pi}\frac{\partial \phi}{\partial z} + \Sigma_t \psi = \frac{1}{4\pi}\Big(\Sigma_s \phi + Q\Big) \,, \tag{8a}$$

$$\phi(0) - 2D\frac{d\phi}{dz}(0) = 0 \,, \tag{8b}$$

$$\phi(Z) + 2D\frac{d\phi}{dz}(Z) = 0 \,. \tag{8c}$$

Operating on Eq. (8a) by $\int(\cdot)d\Omega$, we immediately get

$$-\frac{\partial}{\partial z}D\frac{\partial \phi}{\partial z} + \Sigma_a \phi = Q \,. \tag{9}$$

Thus, for problems with no radial dependence, the 2D/1D equation reduces to the standard 1D axial diffusion equation.

4. *The 2D/1D equation preserves the standard 3D P_1 approximation.* Operating on Eq. (6) by

$$\int (\cdot)\, d\Omega \,, \quad \int \Omega_x (\cdot)\, d\Omega \,, \quad \int \Omega_y (\cdot)\, d\Omega \,, \quad \text{and} \int \Omega_z (\cdot)\, d\Omega \,,$$

and defining

$$J_x = \int \Omega_x \psi \, d\Omega \,, \quad J_y = \int \Omega_y \psi \, d\Omega \,, \quad \text{and } J_z = \int \Omega_z \psi \, d\Omega \,,$$

we obtain:

$$\frac{\partial J_x}{\partial x} + \frac{\partial J_y}{\partial y} - \frac{\partial}{\partial z}D\frac{\partial \phi}{\partial z} + \Sigma_a \phi = Q \,, \tag{10a}$$

$$\frac{\partial}{\partial x}\int \Omega_x^2 \psi \, d\Omega + \frac{\partial}{\partial y}\int \Omega_x \Omega_y \psi \, d\Omega + \Sigma_t J_x = 0 \,, \tag{10b}$$

$$\frac{\partial}{\partial x}\int \Omega_x \Omega_y \psi \, d\Omega + \frac{\partial}{\partial y}\int \Omega_y^2 \psi \, d\Omega + \Sigma_t J_y = 0 \,, \tag{10c}$$

$$\frac{\partial}{\partial x}\int \Omega_x \Omega_z \psi \, d\Omega + \frac{\partial}{\partial y}\int \Omega_y \Omega_z \psi \, d\Omega + \Sigma_t J_z = 0 \,. \tag{10d}$$

Assuming the standard P_1 approximation for ψ:

$$\psi \approx \frac{1}{4\pi}\left[\phi + 3\big(\Omega_x J_x + \Omega_y J_y + \Omega_z J_z\big)\right] \,,$$

Eqs. (10b) and (10c) reduce to:

$$\frac{\partial}{\partial x}\frac{\phi}{3} + \Sigma_t J_x = 0 \,, \tag{11a}$$

$$\frac{\partial}{\partial y}\frac{\phi}{3} + \Sigma_t J_y = 0 \,. \tag{11b}$$

Using Eqs. (11) to eliminate J_x and J_y from Eq. (10a), we obtain the standard diffusion equation.

The above results show that the 2D/1D equation (i) preserves the correct transport physics in the radial variables x and y, and (ii) uses diffusion physics in the axial variable z, in such a way that (iii) the standard 3D (x, y, z) diffusion approximation is preserved. (Applying the standard asymptotic analysis to Eq. (6) also yields the standard diffusion equation.)

These favorable results hold for the "simplest" 2D/1D equation, derived in Sec. 2 from Eqs. (3) and (5c). The same results also hold for more complicated 2D/1D equations, obtained using Eq. (5b) or (5a).

4. DISCRETIZATION OF THE 2D/1D EQUATION

An axial discretization for the 2D/1D Eq. (6) can be derived by integrating the equation over axial "slices" $z_{k-1/2} < z < z_{k+1/2}$ of width $\Delta_k = z_{k+1/2} - z_{k-1/2}$, and using a standard finite difference approximation for the axial leakage term. Assuming that the cross sections are independent of z on each slice and defining:

$$\frac{1}{\Delta_k}\int_{z_{k-1/2}}^{z_{k+1/2}} \psi(\boldsymbol{x},\boldsymbol{\Omega})dz = \psi_k(x,y,\boldsymbol{\Omega}) \;, \tag{12a}$$

$$\frac{1}{\Delta_k}\int_{z_{k-1/2}}^{z_{k+1/2}} \phi(\boldsymbol{x})dz = \phi_k(x,y) = \int \psi_k(x,y,\boldsymbol{\Omega})d\Omega \;, \tag{12b}$$

$$\begin{aligned}\frac{1}{\Delta_k}\int_{z_{k-1/2}}^{z_{k+1/2}} \frac{\partial}{\partial z}D(\boldsymbol{x})\frac{\partial\phi(\boldsymbol{x})}{\partial z}dz &= \frac{1}{\Delta_k}\left[D_{k+1/2}(x,y)\frac{\partial\phi_{k+1/2}(x,y)}{\partial z} - D_{k-1/2}(x,y)\frac{\partial\phi_{k-1/2}(x,y)}{\partial z}\right] \\ &\approx \frac{1}{\Delta_k}\left[\frac{D_{k+1/2}(x,y)}{\Delta_{k+1/2}}\Big(\phi_{k+1}(x,y)-\phi_k(x,y)\Big) - \frac{D_{k-1/2}(x,y)}{\Delta_{k-1/2}}\Big(\phi_k(x,y)-\phi_{k-1}(x,y)\Big)\right] \;,\end{aligned} \tag{12c}$$

where:

$$D_{k+1/2} = \frac{\Delta_k + \Delta_{k+1}}{\frac{\Delta_k}{D_k} + \frac{\Delta_{k+1}}{D_{k+1}}} \quad , \quad \Delta_{k+1/2} = \frac{1}{2}(\Delta_k + \Delta_{k+1}) \;, \tag{13}$$

the axially-discretized 2D/1D equation becomes:

$$\begin{aligned}\left(\Omega_x\frac{\partial}{\partial x} + \Omega_y\frac{\partial}{\partial y} + \Sigma_{t,k}\right)\psi_k(x,y,\boldsymbol{\Omega}) &= \frac{1}{4\pi}\Bigg\{\Sigma_{s,k}\phi_k(x,y) + Q_k(x,y) \\ &+ \frac{1}{\Delta_k}\left[\frac{D_{k+1/2}(x,y)}{\Delta_{k+1/2}}\Big(\phi_{k+1}(x,y)-\phi_k(x,y)\Big) - \frac{D_{k-1/2}(x,y)}{\Delta_{k-1/2}}\Big(\phi_k(x,y)-\phi_{k-1}(x,y)\Big)\right]\Bigg\} \;.\end{aligned} \tag{14}$$

For each $1 \le k \le K$, this is a 2-D transport equation, which is coupled in a simple way (requiring minimal storage and passage of information) to the neighboring slices $k-1$ and $k+1$. The special cases $k = 1$ and K are handled using the boundary conditions (7b), (7c) in the standard manner. For example, Eq. (7c) can be written

$$\phi_{K+1/2}(x,y) - 2J_{K+1/2}(x,y) = 0 \;.$$

This result, coupled with

$$J_{K+1/2} = -\frac{D_K}{\Delta_K/2}\big(\phi_{K+1/2}(x,y) - \phi_K(x,y)\big) = -\frac{D_{K+1/2}}{\Delta_{K+1/2}}\big(\phi_{K+1}(x,y) - \phi_K(x,y)\big)$$

gives:

$$J_{K+1/2}(x,y) = \boxed{-\frac{D_{K+1/2}(x,y)}{\Delta_{K+1/2}}\big(\phi_{K+1}(x,y) - \phi_K(x,y)\big) = \left(\frac{2D_K(x,y)}{\Delta_K + 4D_K(x,y)}\right)\phi_K(x,y)} \;.$$

This (boxed) result enables the term containing ϕ_{K+1}, in Eq. (14) with $k = K$, to be replaced by an equivalent term containing only D_K, Δ_K, and ϕ_K.

In our numerical simulations, we employed the 2D Method-of-Characteristics (MOC) [14] to discretize the radial and angular variables in Eq. (14). The only feature of these discretizations requiring comment is that in DeCART, the axial leakage terms [the second line of Eq. (14)] are discretized on a *coarse* radial grid, while the remaining terms are discretized on a *fine* radial grid. Typically, a coarse spatial cell consists of a pin cell (which is about one mean free path in width), and the fine spatial cells resolve the inner structure of a pin cell (and are small fractions of a mean free path in width). In practice, the radially discretized ϕ's in the axial leakage terms in Eq. (14) are volume-averaged over a coarse cell, and the axial diffusion coefficients $D_{k\pm1/2}$ are homogenized over a coarse cell.

The restriction of the axial leakage terms to coarse mesh scalar fluxes implies that the resulting 2D/1D equation can be parallelized, in such a way that each processor performs sweeps on one slice, and only minimal information (coarse grid scalar fluxes) need to be passed between processors. (If spatially fine-grid or angularly fine-grid information had to be transmitted between processors, the method would have much less parallel efficiency.)

For highly-scattering homogeneous medium problems in which classic diffusion theory is valid, the axial diffusion coefficients do not need to be radially homogenized, and the prescription $D = 1/3\Sigma_t$ in Eq. (14) is valid. These are the types of problems considered in this paper, and discussed in our numerical results [1]. However, for reactor cores, in which ψ is a strong function of x, y, and $\mathbf{\Omega}$, classic diffusion theory is not valid, and a more sophisticated approximation to the axial leakage term becomes necessary for optimum accuracy. This is discussed in more detail in Section 6.

5. ITERATIVE METHODS

Next, we consider what is likely the simplest possible iteration scheme for solving Eq. (14) that can be made stable for all $\Delta_z > 0$. Noting that the right side of Eq. (14) depends only on the scalar flux ϕ, we consider a simple 2D sweep on each slice to update the scalar flux:

$$\left(\Omega_x\frac{\partial}{\partial x}+\Omega_y\frac{\partial}{\partial y}+\Sigma_{t,k}\right)\psi_k^{(\ell+1/2)}(\boldsymbol{x},\mathbf{\Omega})=\frac{1}{4\pi}\Bigg\{\Sigma_{s,k}\phi_k^{(\ell)}(\boldsymbol{x})+Q_k(\boldsymbol{x})$$
$$+\frac{1}{\Delta_k}\left[\frac{D_{k+1/2}}{\Delta_{k+1/2}}\Big(\phi_{k+1}^{(\ell)}(\boldsymbol{x})-\phi_k^{(\ell)}(\boldsymbol{x})\Big)-\frac{D_{k-1/2}}{\Delta_{k-1/2}}\Big(\phi_k^{(\ell)}(\boldsymbol{x})-\phi_{k-1}^{(\ell)}(\boldsymbol{x})\Big)\right]\Bigg\}\,, \tag{15a}$$

$$\phi_k^{(\ell+1/2)}(\boldsymbol{x})=\int\psi_k^{(\ell+1/2)}(\boldsymbol{x},\mathbf{\Omega}')d\Omega'\,, \tag{15b}$$

followed by a (nonstandard) relaxation step to define the end-of-iteration scalar flux:

$$\phi_k^{(\ell+1)}(\boldsymbol{x})=\theta\phi_k^{(\ell+1/2)}(\boldsymbol{x})+(1-\theta)\phi_k^{(\ell)}(\boldsymbol{x})\,. \tag{15c}$$

In analyzing this method, we do not treat Eq. (15) with any angular or radial spatial discretizations; our experience is that these although these choices affect the accuracy of the discrete solution, they do not affect the iterative performance in converging to this solution. The relaxation parameter θ in Eq. (15c) is to be determined; if $\theta = 1$, the method defined by Eqs. (15) is basically Source Iteration (and is very similar, if not identical, to the original iteration method encoded in DeCART). We note that in each iteration, the numerical solutions in slice k are directly coupled only to the numerical solutions in the neighboring slices $k+1$ and $k-1$. Therefore, many iterations may be required for the numerical fluxes in all the axial slices $1 \le k \le K$ to sufficiently "communicate."

For an infinite, homogeneous medium with uniform $\Delta_k = \Delta_z$, the iterative performance of the above method can be assessed by a Fourier analysis. The standard Fourier ansatz is:

$$Q_k(\boldsymbol{x}) = 0 \ , \tag{16a}$$

$$\phi_k^{(\ell)}(\boldsymbol{x}) = \omega^\ell e^{i\Sigma_t(\boldsymbol{\lambda}\cdot\boldsymbol{x})} \ , \tag{16b}$$

$$\psi_k^{(\ell+1/2)}(\boldsymbol{x},\boldsymbol{\Omega}) = \omega^\ell a(\boldsymbol{\Omega}) e^{i\Sigma_t(\boldsymbol{\lambda}\cdot\boldsymbol{x})} \ , \tag{16c}$$

$$\phi_k^{(\ell+1/2)}(\boldsymbol{x}) = \omega^\ell A e^{i\Sigma_t(\boldsymbol{\lambda}\cdot\boldsymbol{x})} \ , \tag{16d}$$

where $\boldsymbol{\lambda} = (\lambda_x, \lambda_y, \lambda_z)$ is an arbitrary fixed 3-vector. Introducing Eqs. (16) into (15), we easily obtain

$$\big[i\big(\Omega_x\lambda_x + \Omega_y\lambda_y\big) + 1\big] a(\boldsymbol{\Omega}) = \frac{1}{4\pi}\left[c - \frac{2}{3}\left(\frac{1-\cos\Sigma_t\lambda_z\Delta_z}{(\Sigma_t\Delta_z)^2}\right)\right] \ , \tag{17a}$$

$$A = \int a(\boldsymbol{\Omega})\, d\Omega \ , \tag{17b}$$

$$\omega = \theta A + 1 - \theta \ . \tag{17c}$$

Introducing Eq. (17a) into Eq. (17b), we get

$$A = \left[c - \frac{2}{3}\left(\frac{1-\cos\Sigma_t\lambda_z\Delta_z}{(\Sigma_t\Delta_z)^2}\right)\right] I_0 \ , \tag{18}$$

where $c = \Sigma_s/\Sigma_t$ is the scattering ratio, and

$$\begin{aligned} I_0 &= \frac{1}{4\pi}\int \frac{d\Omega}{1 + i(\Omega_x\lambda_x + \Omega_y\lambda_y)} \\ &= \frac{1}{2}\int_{-1}^{1} \frac{d\mu}{1 + (\lambda_r\mu)^2} \qquad \left(\lambda_r = \sqrt{\lambda_x^2 + \lambda_y^2}\right) \ , \\ &= \frac{1}{\lambda_r}\tan^{-1}\lambda_r \ . \end{aligned}$$

I_0 monotonically decreases from 1 to 0 as λ_r increases from 0 to ∞. Thus, since $I_0 > 0$, Eq. (18) gives

$$\left[c - \frac{4}{3(\Sigma_t\Delta_z)^2}\right] I_0 \le A \le cI_0 \ .$$

This implies

$$A_{max} = c \ , \tag{19a}$$

which is attained for "flat" radial and axial modes ($\lambda_r \approx 0$ and $\lambda_z \approx 0$). Also,

$$A_{min} = \begin{cases} 0 & , \quad \Sigma_t\Delta_z \ge \frac{2}{\sqrt{3c}} \ , \quad (\text{ "large" } \Delta_z) \ , \\ c - \frac{4}{3(\Sigma_t\Delta_z)^2} & , \quad \Sigma_t\Delta_z < \frac{2}{\sqrt{3c}} \ , \quad (\text{ "small" } \Delta_z) \ , \end{cases} \tag{19b}$$

which is attained (i) for "large" Δ_z by $\lambda_r \approx \infty$ (radially oscillatory modes), and (ii) for "small" Δ_z by $\lambda_r \approx 0$ (radially flat modes) and $\lambda_z \approx \pi/\Sigma_t\Delta_z$ (axially oscillatory modes).

By Eq. (17c), we have for $0 \le \theta \le 1$

$$\theta A_{min} + 1 - \theta \le \omega \le \theta A_{max} + 1 - \theta \ . \tag{20}$$

For $\theta = 1$ (the "Source Iteration" method originally in DeCART), Eqs. (19) and (20) give

$$A_{min} \leq \omega \leq A_{max} \ ,$$

and therefore

$$\rho = |\omega|_{max} = \begin{cases} c & , \quad \sqrt{\frac{2}{3c}} < \Sigma_t \Delta_z \ , \\ \frac{4}{3(\Sigma_t \Delta_z)^2} - c & , \quad \Sigma_t \Delta_z \leq \sqrt{\frac{2}{3c}} \ . \end{cases} \tag{21}$$

This method is stable for

$$\Sigma_t \Delta_z > \frac{2}{\sqrt{3(1+c)}} \ ,$$

but for small Δ_z it becomes unstable, similar to the original method in DeCART.

Since $A_{max} > 0$, it can be shown that the optimum value of θ in Eq. (20) is the value for which the left and right sides are equal in magnitude but opposite in sign:

$$\theta_{opt} A_{min} + 1 - \theta_{opt} = -\left[\theta_{opt} A_{max} + 1 - \theta_{opt}\right] \ . \tag{22a}$$

Thus,

$$\theta_{opt} = \frac{2}{2 - (A_{max} + A_{min})} \ , \tag{22b}$$

and then

$$\begin{aligned} \rho = |\omega|_{max} &= \theta_{opt} A_{max} + 1 - \theta_{opt} \\ &= \frac{A_{max} - A_{min}}{2 - (A_{max} + A_{min})} \ . \end{aligned} \tag{22c}$$

Combining Eqs. (19) and (22), we obtain:

$$\theta_{opt} = \begin{cases} \frac{2}{2-c} & , \quad \frac{2}{\sqrt{3c}} < \Sigma_t \Delta_z \ , \\ \frac{3(\Sigma_t \Delta_z)^2}{2+3(1-c)(\Sigma_t \Delta_z)^2} & , \quad \Sigma_t \Delta_z \leq \frac{2}{\sqrt{3c}} \ , \end{cases} \tag{23a}$$

$$\rho = \begin{cases} \frac{c}{2-c} & , \quad \frac{2}{\sqrt{3c}} < \Sigma_t \Delta_z \ , \\ \frac{2}{2+3(1-c)(\Sigma_t \Delta_z)^2} & , \quad \Sigma_t \Delta_z \leq \frac{2}{\sqrt{3c}} \ . \end{cases} \tag{23b}$$

Eq. (23b) shows that the iterative method defined by Eqs. (15) with θ defined by Eq. (23a) is stable for all scattering ratios $0 \leq c \leq 1$ and all axial grids $\Delta_z > 0$. (See Fig. 2 on the next page.) Like standard Source Iteration applied to the S_N equations, this method become slowly converging as $c \to 1$. It also becomes slowly converging as $\Delta_z \to 0$. However, like Source Iteration, it does not become unstable.

6. DISCUSSION

In this paper we have proposed a basic mathematical foundation for the 2D/1D methodology in DeCART. The starting point of our analysis is a 2D/1D equation – a second-order integrodifferential equation that approximates the linear 3D Boltzmann equation only in its axial leakage term. Many approximations to the axial leakage are possible; in this paper we have treated only the simplest. By systematically discretizing this "simplest" 2D/1D equation in all its independent variables, and then by formulating and Fourier-analyzing an iterative method for solving the discrete equations, we obtain a computational method that (i) iteratively converges for each fixed grid, and (ii) also converge as the grid is refined – to the analytic solution of the original 2D/1D equation. Numerical results, presented and discussed in [1], confirm these theoretical predictions and show that for 3D problems in which the standard diffusion approximation is valid, the 2D/1D and linear Boltzmann equations yield highly similar solutions.

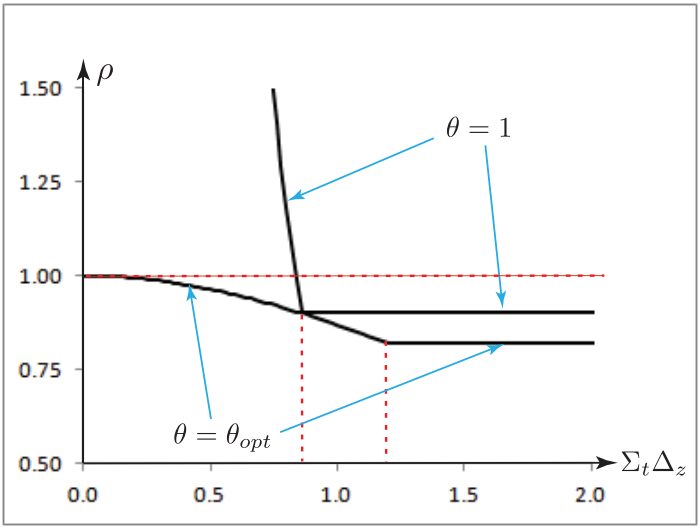

Figure 2: Spectral Radius ρ vs Axial Optical Thickness $\Sigma_t \Delta_z$ for $c = 0.9$

The theory presented in this paper fulfills two goals:

1. By using the 2D/1D equation as the starting point, numerical 2D/1D solutions can be interpreted in the limit as the numerical grids become fine: these solutions will consistently limit to the analytic solution of the continuous 2D/1D equation – which approximates the Boltzmann equation more accurately than the standard diffusion equation. (Without an underlying approximate transport equation as a starting point, it is not evident that a discretization method will possess a limiting solution as the grids are refined.)

2. By using a standard Fourier analysis, stable iteration methods can be developed for solving the consistently-discretized 2D/1D equations.

Both of these goals are illustrated in our companion (numerical comparisons) paper [1].

The theory presented here applies only to the simplest 2D/1D equation, using a standard finite-difference approximation for the 1D axial diffusion discretization, and a relatively simple "Source Iteration" method with under-relaxation. For the theory to become applicable to realistic reactor core problems, it must be generalized in several ways:

1. It must include multigroup energy dependence with anisotropic scattering.

2. Eq. (14) can be directly applied to problems with radial spatial variation of the type found in reactor cores. This basic procedure is followed in DeCART, and useful numerical results are obtained. However, in these problems classic diffusion theory is not valid, and the logic that leads to Eq. (5c) with $D = 1/3\Sigma_t$ is also not valid. Therefore, although the 2D/1D Eq. (14) with $D = 1/3\Sigma_t$ can be solved, there is no theoretical reason why the classic diffusion coefficient $D = 1/3\Sigma_t$ should yield the most accurate solution. Fortunately, an asymptotic theory has been developed that provides the logic needed to specify D [15, 16]. This approach will be used in our future work.

3. Currently, DeCART uses a nodal (not a finite difference) axial diffusion discretization in z. The option of a nodal discretization in z is being implemented and tested in MPACT.

4. More sophisticated iteration schemes should be considered, in order to solve the 2D/1D equation more efficiently. Unlike standard Source Iteration for the S_N equations, for which the most slowly

converging modes are "flat" or "diffusive," the most slowly converging modes for the simple "Source Iteration" method developed here for the 2D/1D equations are oscillatory if Δ_z is "small." Thus, using a low-order diffusion equation to accelerate the iterative convergence of the 2D/1D equations may not perform in the same way, or as well, as it does for the S_N equations.

5. It should be determined how much more accurate Eq. (5a) is than Eq. (5b), and how much more accurate Eq. (5b) is than Eq. (5c). Other angular approximations to the axial leakage term, more accurate than the P_1 representation in Eq. (5a), should be also considered. The following issues should be kept in mind:

   (a) If the angular discretizations of F and ψ satisfy Eq. (4a), then the angularly-discretized 2D/1D Eq. (3) becomes identical to the angularly-discretized linear Boltzmann equation. Thus, by systematically increasing the accuracy of the angular dependence of the axial leakage term, the solution of the *continuous* 2D/1D equation should systematically limit to the solution of the *continuous* Boltzmann equation.

   (b) As the angular complexity of the transverse leakage term increases, the amount of information that must be passed between processors will increase, and the parallel efficiency of the resulting method will decrease. Thus, there is a tradeoff between accuracy and parallelizability.

   (c) An extra degree of complexity occurs because of the fine and coarse radial spatial grids: no amount of angular refinement will cause the discrete 2D/1D solution to limit to the discrete Boltzmann solution unless all the spatial grids are refined.

The difference between the 2D/1D method in DeCART, and the 2D/1D Fusion method in CRX can now be explained. Both methods employ a coarse radial grid (in which one cell = one pin cell) and a fine radial grid (to resolve the inner structure of a pin cell). Both methods (i) use MOC to discretize the 2D transport operator on the fine radial grid, and (ii) discretize the axial leakage terms on the coarse radial grid, using homogenized data in the axial leakage terms. However, the DeCART method uses Eq. (5c) to approximate F, while the CRX method uses the exact Eq. (4a) for F. Thus: the CRX method is an unconventional discretization of the 3D Boltzmann equation (*not the 2D/1D equation!*) – in which fine and coarse radial spatial grids occur, the radial derivative terms are evaluated on the fine mesh using 2D MOC, and the axial derivative term is evaluated on the coarse radial mesh using a standard 1D S_N discretization method (diamond difference, step or linear characteristic, or nodal).

Since the 2D/1D Fusion method in CRX uses the exact Eq. (4a) for F, it should be more accurate than the 2D/1D method in DeCART. However, because of the full angular dependence of the axial leakage terms in CRX, much more information must be calculated, stored, and passed between processors; this method will be more costly and less parallelizable than the DeCART method. Also, the CRX 1D axial equation is a transport – not a diffusion – equation, and accurately discretizing this equation for coarse Δ_z is more problematic than discretizing the diffusion equation for coarse Δ_z. Thus, although the 2D/1D Fusion method in CRX should be more accurate, it should also be more complex, more costly, and less parallelizable.

To summarize: we have presented in this paper the beginning of a mathematical theory for the 2D/1D methodology in DeCART, so that this methodology can be systematically developed and improved for practical reactor core problems. We plan to continue this effort in our future work.

ACKNOWLEDGEMENTS

We wish to acknowledge many helpful discussions with Han Joo, Tom Downar, Bill Martin, and Ben Collins. Also, we gratefully acknowledge support by the NEUP contract No. DE-AC07-05ID14517, and by

the Consortium for Advanced Simulation of Light Water Reactors (www.casl.gov), an Energy Innovation Hub (http://www.energy.gov/hubs) for Modeling and Simulation of Nuclear Reactors under U.S. Department of Energy Contract No. DE-AC05-00OR22725.

REFERENCES

[1] B. Kelley, B. Collins, and E.W. Larsen, " 2D/1D Approximations to the 3D Neutron Transport Equation. II: Numerical Comparisons," *Proc. M&C 2013*, Sun Valley, ID, USA, May 5-9 (2013).

[2] J.Y. Cho, H.G. Joo, K.S. Kim, and S.Q. Zee, "Three-Dimensional Heterogeneous Whole Core Transport Calculation Employing Planar MOC Solutions," *Trans. Am. Nucl. Soc.*, **87**, pp. 234-236 (2002).

[3] N.Z. Cho, G.S. Lee, and C.J. Park, "Refinement of the 2-D/1-D Fusion Method for 3-D Whole Core Transport Calculation," *Trans Am. Nucl. Soc.*, **87**, pp. 417-420 (2002).

[4] N.Z. Cho, G.S. Lee, and C.J. Park, "A Fusion Technique of 2-D/1-D Methods for Three-Dimensional Whole-Core Transport Calculations," *Proc. Korean Nucl. Soc.*, Kwangju, Korea (May, 2002).

[5] N.Z. Cho, G.S. Lee, and C.J. Park, "Partial Current-Based CMFD Acceleration of the 2D/1D Fusion Method for 3D Whole Core Transport Calculations," *Trans. Am. Nucl. Soc.*, **88**, pp. 594-596 (2003).

[6] H.G. Joo, J.Y. Cho, K.S. Kim, C.C. Lee, and S.Q. Zee, "Methods and Performance of a Three-Dimensional Whole Core Transport Code DeCART," *Proc. PHYSOR 2004*, Chicago, April 25-29, 2004, American Nuclear Society, CD-ROM (2004).

[7] S. Kosaka and T. Takeda, "Verification of 3D Heterogeneous Core Transport Calculation Using Nonlinear Iteration Technique," *J. Nucl. Sci. Tech.*, **41**, No. 6, pp. 645-654 (2004).

[8] N.Z. Cho, "Fundamentals and Recent Developments of Reactor Physics Methods," *Nucl. Eng. Tech.*, **37**, pp. 25-78 (2005).

[9] G.S. Lee and N.Z. Cho, "2D/1D Fusion Method Solutions of the Three-Dimensional Transport OECD Benchmark Problem C5G7 MOX," *Prog. Nucl. Energy*, **48**, pp. 410-423 (2006).

[10] J.Y. Cho and J.G. Joo, "Solution of the C5G7MOX Benchmark Three-Dimensional Extension Problems by the DeCART Direct Whole Core Calculation Code," *Prog. Nucl. Energy,* **48**, pp. 456-466 (2006).

[11] J.Y. Cho, K.S. Kim, C.C. Lee, S.Q. Zee, and H.G. Joo, "Axial SPN and Radial MOC Coupled Whole Core Transport Calculation," *J. Nuc. Sci. Tech.*, **44**, pp. 1156-1171 (2007).

[12] N.Z. Cho, G.S. Lee, and C.J. Park, "Fusion Method of Characteristics and Nodal Method for 3D Whole Core Transport Calculation," *Trans. Am. Nucl. Soc.*, **86**, pp. 322-324 (2002).

[13] B. Kochunas, et al., "Overview of Development and Design of MPACT: Michigan Parallel Characteristics Transport Code," *Proc. M&C 2013*, Sun Valley, ID, USA, May 5-9 (2013).

[14] B. Kochunas, Z. Liu, and T. Downar, "Parallel 3-D Method of Characteristics in MPACT," *Proc. M&C 2013*, Sun Valley, ID, USA, May 5-9 (2013).

[15] T.J. Trahan and E.W. Larsen, "An Asymptotic Homogenized Neutron Diffusion Approximation. I. Theory," *Proc. PHYSOR 2012*, Knoxville, TN, April 15-20, 2012, American Nuclear Society, CD-ROM (2012).

[16] T.J. Trahan and E.W. Larsen, "An Asymptotic Homogenized Neutron Diffusion Approximation. II. Numerical Comparisons," *Proc. PHYSOR 2012*, Knoxville, TN, April 15-20, 2012, American Nuclear Society, CD-ROM (2012).

2D/1D APPROXIMATIONS TO THE 3D NEUTRON TRANSPORT EQUATION. II: NUMERICAL COMPARISONS

Blake W. Kelley, Benjamin Collins, and Edward W. Larsen
Department of Nuclear Engineering and Radiological Sciences
University of Michigan, Ann Arbor, MI 48109
kelleybl@umich.edu; bscollin@umich.edu; edlarsen@umich.edu

ABSTRACT

In a companion paper [1], (i) several new "2D/1D equations" are introduced as accurate approximations to the 3D Boltzmann transport equation, (ii) the simplest of these approximate equations is systematically discretized, and (iii) a theoretically stable iteration scheme is developed to solve the discrete equations. In this paper, numerical results are presented that confirm the theoretical predictions made in [1].

Key Words: 3D neutron transport simulations, diffusion approximation, Fourier analysis

1. INTRODUCTION

In a companion paper [1], new 2D/1D approximations to the 3D neutron transport equation are proposed in which the exact transport physics is preserved for the radial directions x and y, but is approximated by classic diffusion physics for the axial direction z. The purpose of the 2D/1D equations is to provide a mathematical basis for accurate, efficient methods for simulating 3D reactor cores, in which the spatial variation of the neutron flux is usually much more complex in the radial directions than in the axial direction. In the present paper, we provide numerical evidence showing that for geometrically simple 3D problems, the theoretical predictions of (i) the accuracy of the simplest 2D/1D solutions, and (ii) the stability of the "source iteration with under-relaxation" iterative method (described in [1]) are valid. More specifically, we show the following:

- Numerical solutions of the 2D/1D equation exist and can be obtained iteratively, in accordance with the theory developed in [1].
- For 3D problems that are "classically diffusive" (optically thick and highly scattering), the 2D/1D and diffusion solutions both well-approximate the transport solution.
- For problems which are diffusive axially, but not radially, the 2D/1D solutions are more accurate (closer to the solution of the Boltzmann equation) than the standard diffusion solution.
- The "source iteration with under-relaxation" iteration scheme for solving the 2D/1D equation is experimentally stable, and the performance (spectral radius) of this scheme is accurately predicted by the Fourier analysis.

To demonstrate these properties of the 2D/1D equations, we consider the 3D fixed-source homogeneous-medium transport equation with a flat source:

$$\boldsymbol{\Omega}\cdot\boldsymbol{\nabla}\psi(\boldsymbol{x},\boldsymbol{\Omega})+\Sigma_t\psi(\boldsymbol{x},\boldsymbol{\Omega})=\frac{\Sigma_s}{4\pi}\int_{4\pi}\psi(\boldsymbol{x},\boldsymbol{\Omega}')d\Omega'+\frac{Q}{4\pi}\ ,\quad \boldsymbol{x}\in V\ ,\ \boldsymbol{\Omega}\in 4\pi\ , \tag{1}$$

defined on a hexahedral domain V consisting of points $\boldsymbol{x}=(x,y,z)$, with $(x,y)\in$ the square R consisting of points $0<x,y<L$, and $0\leq z\leq Z$. The boundary conditions (i) on the "inner" three sides of V touching the point $(0,0,0)$ are reflecting, and (ii) on the "outer" three sides of V are vacuum.

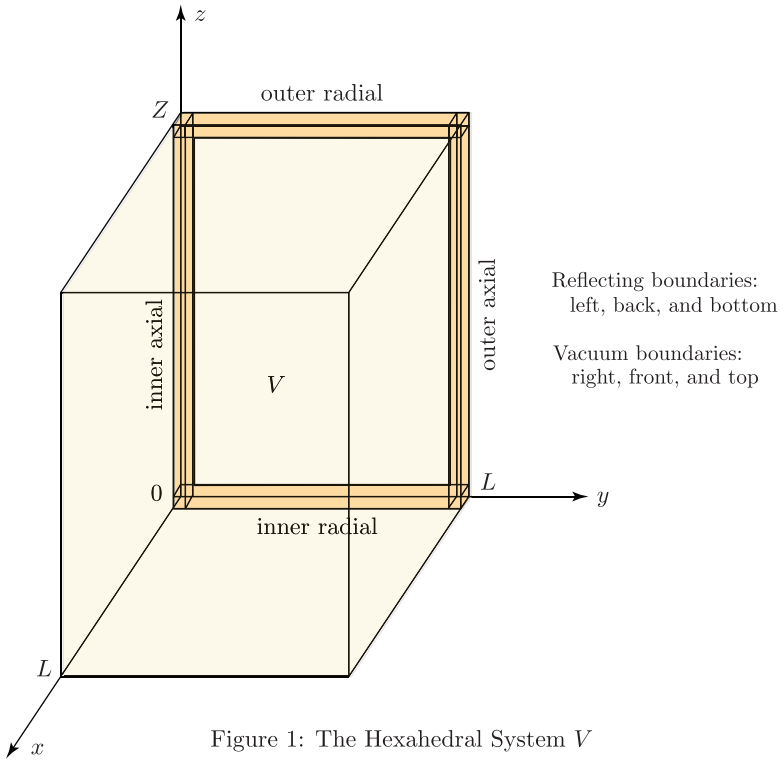

Figure 1: The Hexahedral System V

We discretize z by a uniform grid $0 = z_{1/2} < \cdots < z_{k-1/2} < z_{k+1/2} < \cdots z_{K+1/2} = Z$, with $z_{k+1/2} - z_{k-1/2} = \Delta_z$. For each axial "slice," we define

$$\psi_k(x, y, \mathbf{\Omega}) = \frac{1}{\Delta_z} \int_{z_{k-1/2}}^{z_{k+1/2}} \psi(x, y, z', \mathbf{\Omega}) dz' \ , \quad 1 \leq k \leq K \ . \tag{2}$$

In [1], we derived for this (homogeneous medium, uniform axial grid) problem, the following axially-discretized 2D/1D approximation to Eqs. (1):

$$\Big(\Omega_x \frac{\partial}{\partial x} + \Omega_y \frac{\partial}{\partial y} + \Sigma_t\Big)\psi_k(x, y, \mathbf{\Omega}) = \frac{1}{4\pi}\Bigg[\Sigma_s \phi_k(x, y) + Q + \frac{D}{\Delta_z^2}\Big(\phi_{k+1}(x, y) - 2\phi_k(x, y) + \phi_{k-1}(x, y)\Big)\Bigg] \ , \tag{3}$$

where

$$\phi_k(x, y) = \int_{4\pi} \psi_k(x, y, \mathbf{\Omega}') \, d\Omega' \quad , \quad D = \frac{1}{3\Sigma_t} \ . \tag{4}$$

The boundary of V has six planar surfaces. The boundary conditions on the four "radial" bounding surfaces of V (whose normal vectors point in the radial directions) are the usual transport reflecting or vacuum boundary conditions. On the two "axial" bounding surfaces of V, whose normal vectors point in the $\pm$ axial directions, the reflecting and vacuum boundary conditions can be formulated as (see [1])

$$\phi_0(x, y) = \phi_1(x, y) \ , \quad (x, y) \in R \qquad \text{(reflecting)} \ , \tag{5a}$$

$$\phi_{K+1}(x, y) = \left(\frac{4D - \Delta_z}{4D + \Delta_z}\right) \phi_K(x, y) \ , \quad (x, y) \in R \qquad \text{(vacuum)} \ . \tag{5b}$$

These conditions specify ϕ_0 and ϕ_{K+1} and thus make Eq. (3) valid for all $1 < k < K$.

In the MPACT code [2], we have discretized the 2D/1D equation in x, y, and $\mathbf{\Omega}$ using the method of characteristics [3]. In Section 2 of this paper we discuss the accuracy of the resulting 2D/1D solutions (by showing plots of the scalar flux on the four rows of spatial cells shown in Figure 1), and in Section 3 we discuss the performance of the iterative "source iteration with under-relaxation" iteration scheme (described in [1]). Section 4 concludes this paper with a discussion.

2. ACCURACY OF THE 2D/1D SOLUTIONS

To test the accuracy of the 2D/1D solutions, we consider six homogeneous, purely-scattering problems, defined as follows:

$$
\begin{aligned}
Z &= 10 \text{ cm} , \\
X = Y = L &= 10,\ 5,\ \text{and } 2.5 \text{ cm} \qquad (3 \text{ cases}) , \\
\Sigma_t = \Sigma_s &= 1.0 \text{ cm}^{-1} , \\
Q &= 1.0 \text{ cm}^{-3} \text{ sec}^{-1} , \\
\Delta_x = \Delta_y &= 0.05L , \\
\Delta_z &= 0.5 \text{ and } 1.0 \text{ cm} \qquad (2 \text{ cases}) .
\end{aligned}
$$

The problems differ by their values of Δ_z and L, with $\Delta x = \Delta y$ scaled proportional to L. For $L = 10$ cm, the system is a cube of width, height, and depth equal to 20 mean free paths. This problem is reasonably "diffusive," so the 3D MOC, 2D/1D and standard diffusion solutions should agree reasonably well. Figure 2 plots the cell-averaged scalar fluxes along the four rows of cells depicted in Figure 1: the "Inner Radial" row, which adjoins the center of the system and extends to the outer boundary in the radial (y) direction, the "Inner Axial" row, which adjoins the center of the system and extends to the outer boundary in the axial (z) direction, and the "Outer Radial" and "Outer Axial" rows, which adjoin the outer boundary of the system.

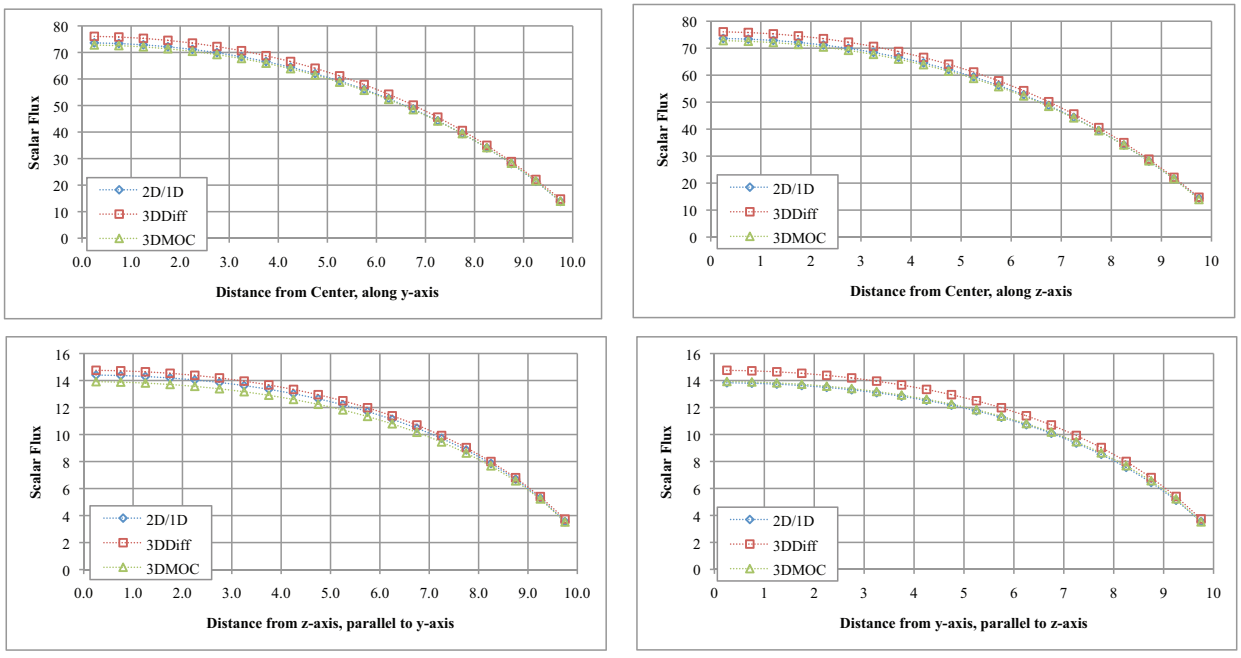

Figure 2: Scalar Flux Plots for $L = 10$ cm and Δ_z = 0.5 cm

Top Left: Inner Radial Top Right: Inner Axial
Bottom Left: Outer Radial Bottom Right: Outer Axial

The 3D MOC and 2D/1D solutions agree closely on the inner radial, inner axial, and outer axial rows of cells. Along these rows, the axial derivative (diffusion) term in the 2D/1D equation does not dominate the radial derivative (transport) term – and the resulting approximation should be accurate. The accuracy is not as good on the outer radial row of cells, in which an axial transport boundary layer occurs. Here the diffusion axial derivative term of the 2D/1D equation dominates the transport radial derivative terms, and the axial transport boundary layer is treated with diffusion (not transport) accuracy.

In all four subplots of Figure 2, the diffusion solution has the correct qualitative shape, but its amplitude is consistently about 6% high. The reason for the reasonable but not tight accuracy of the diffusion approximation is that the $L = 10$ problem is not sufficiently large (optically thick).

Overall, the 2D/1D solution agrees closely with the 3D MOC solution (i.e. has "transport accuracy") in the interior of V, and on the parts of ∂V where the axial derivative does not dominate the radial derivative. On the parts of ∂V where the axial derivative dominates the radial derivative, the 2D/1D solution has "diffusion accuracy." (Where this happens – on the outer radial row of cells – the 2D/1D error is about half that of the diffusion solution.)

As L = width = depth of V is reduced, V becomes more "leaky" (and hence more transport-like) in the radial directions x and y. However, V remains optically thick in the z-direction, and the scalar flux should continue to vary smoothly and slowly in z. The 2D/1D solutions for smaller L should continue to have transport accuracy – except possibly on the outer radial row of cells, where at worst it should have diffusion accuracy. Figure 3 depicts similar plots as in Figure 2, but instead for the $L = 5$ problem.

Figure 3 shows that indeed, the 2D/1D solution has transport accuracy away from the outer radial rows of cells, and in this row it is more accurate than before! The likely reason for this is that the axial derivatives in this row are similar to those in the previous problem, but the radial derivatives are larger. Thus, the axial

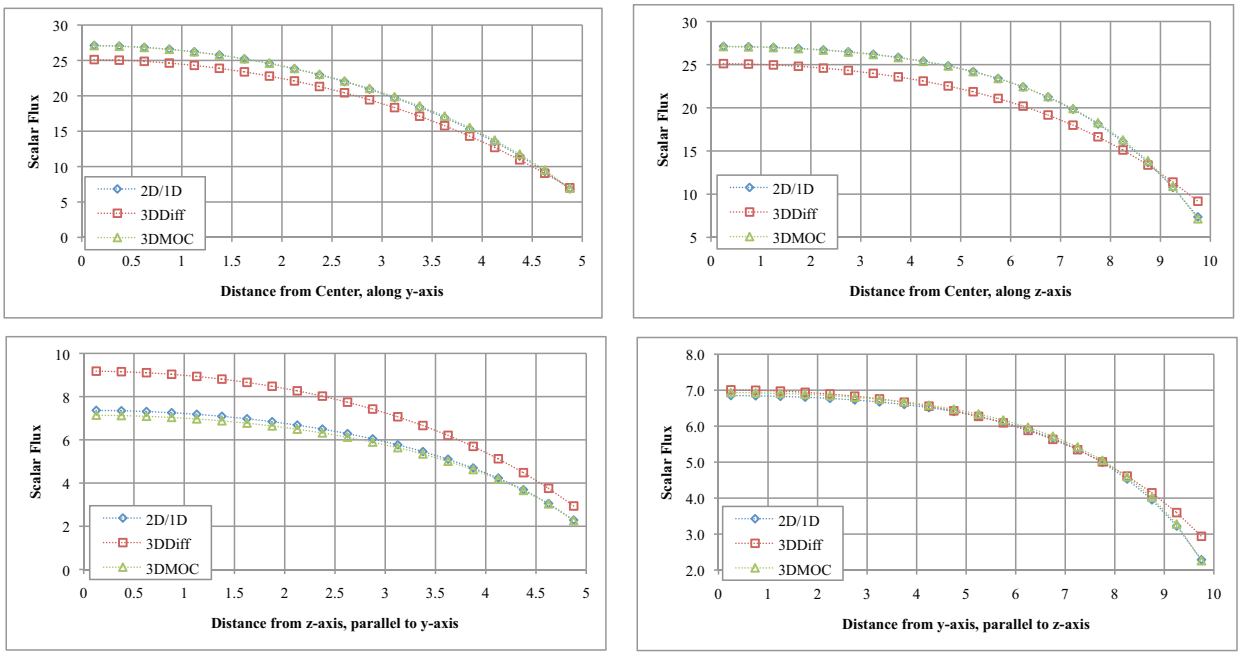

Figure 3: Scalar Flux Plots for $L = 5.0$ cm and $\Delta_z = 0.5$ cm

Top Left: Inner Radial Top Right: Inner Axial
Bottom Left: Outer Radial Bottom Right: Outer Axial

derivatives in this problem do not dominate to the same extent that they did in the previous problem. In this problem, the diffusion solution is about 10% low in the center of the problem, 20% high on the outer radial row, and reasonably accurate on the outer axial row of cells.

Next, Figure 4 depicts the same types of plots as in Figure 2, for the $L = 2.5$ problem:

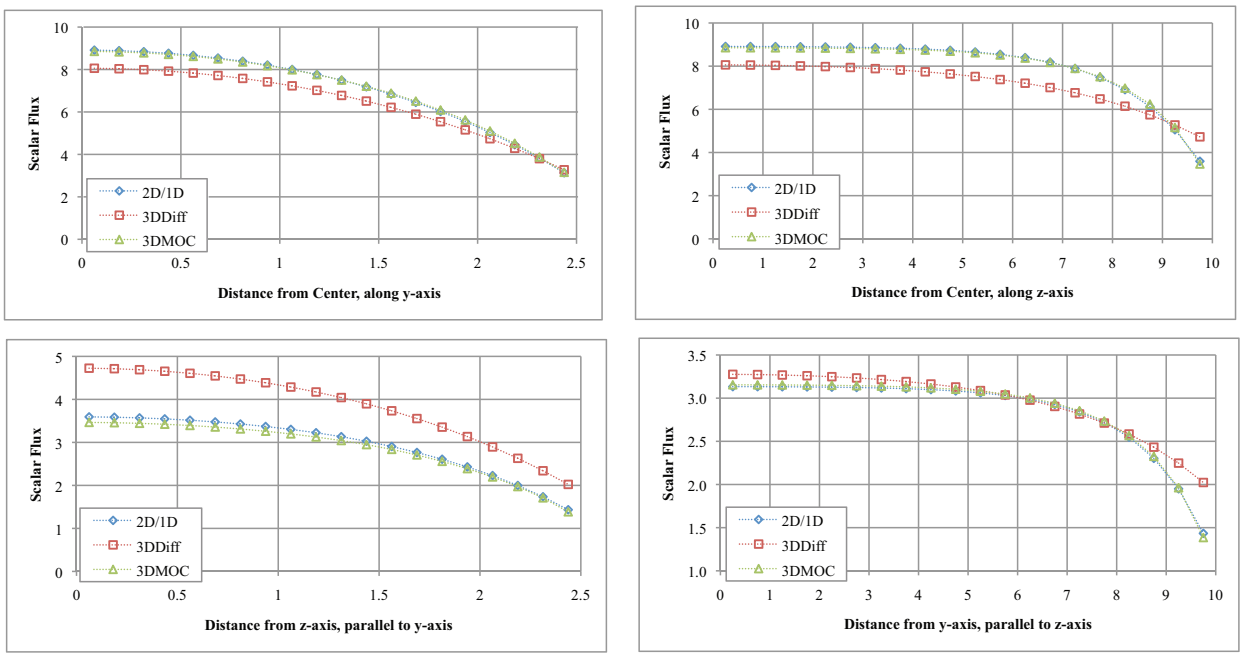

Figure 4: Scalar Flux Plots for $L = 2.5$ cm and $\Delta_z = 0.5$ cm

Top Left: Inner Radial Top Right: Inner Axial
Bottom Left: Outer Radial Bottom Right: Outer Axial

These plots continue the same basic trends seen – and discussed – in Figures 2 and 3. Overall, Figures 2-4 show that the 2D/1D solutions treat "radial" boundary layers (along surfaces whose normals point in a radial direction) with transport accuracy, and "axial" boundary layers (along surfaces whose normals point in an axial direction) with at worst diffusion accuracy. (If the axial boundary layers contain significant radial derivative terms, the 2D/1D accuracy increases.)

The next three figures present the same three problems depicted in Figures 2-4, but now calculated with a coarser axial grid size of $\Delta_z = 1.0$ cm. We include these results to give evidence that – provided the solution varies slowy in z – the 2D/1D solution will remain accurate if Δ_z is chosen to be on the order of (or smaller than) a *diffusion length*. The discretization of the transport part of the 2D/1D equation generally requires the radial variables x and y to be discretized on a grid which is small compared to a *mean free path*. Thus: for the 3D problems in which the 2D/1D approximation is valid, it should be possible to discretize the 2D/1D equations on a coarser axial grid than the 3D transport equation. (This is another advantage of the 2D/1D approximation.) We note that DeCART is routinely run in this manner – with an axial grid which is much coarser than the radial grid.

The results in Figures 5-7 are similar to those in Figures 2-4. Overall, the diffusion solution is less accurate than before, due to the transport boundary layer on the outer radial surface, which is now even less resolved by the diffusion solution on the coarser axial grid. In all cases, 2D/1D solution has

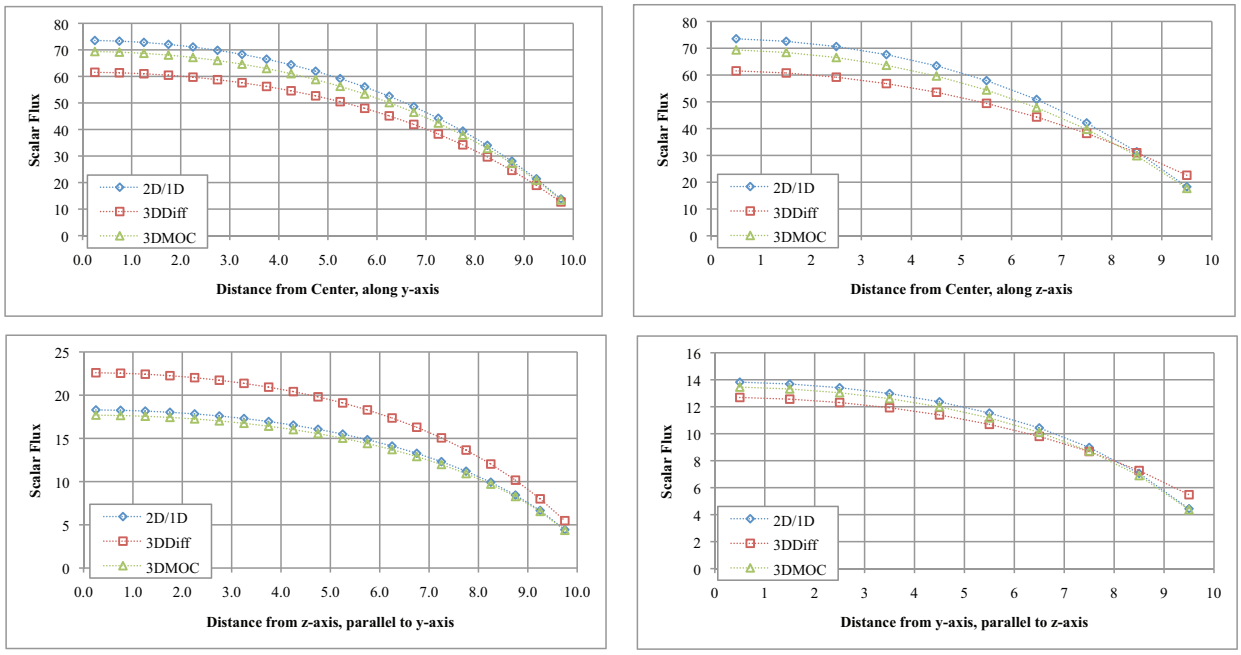

Figure 5: Scalar Flux Plots for $L = 10$ cm and Δ_z = 1.0 cm

Top Left: Inner Radial Top Right: Inner Axial
Bottom Left: Outer Radial Bottom Right: Outer Axial

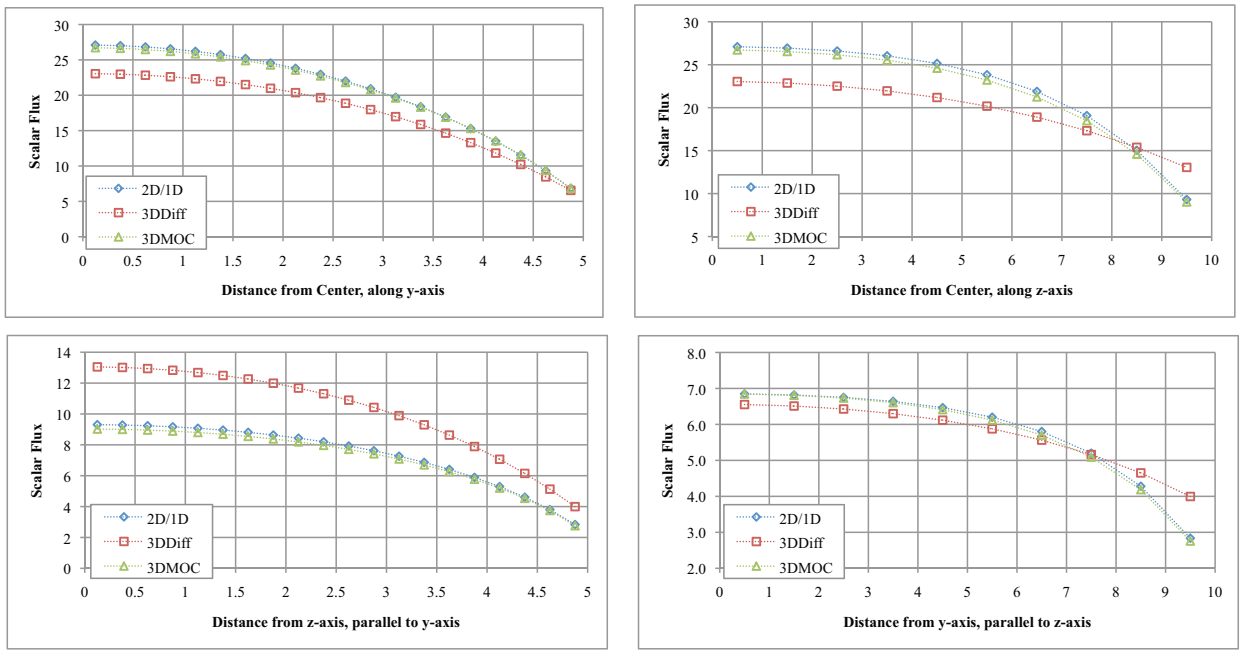

Figure 6: Scalar Flux Plots for $L = 5.0$ cm and Δ_z = 1.0 cm

Top Left: Inner Radial Top Right: Inner Axial
Bottom Left: Outer Radial Bottom Right: Outer Axial

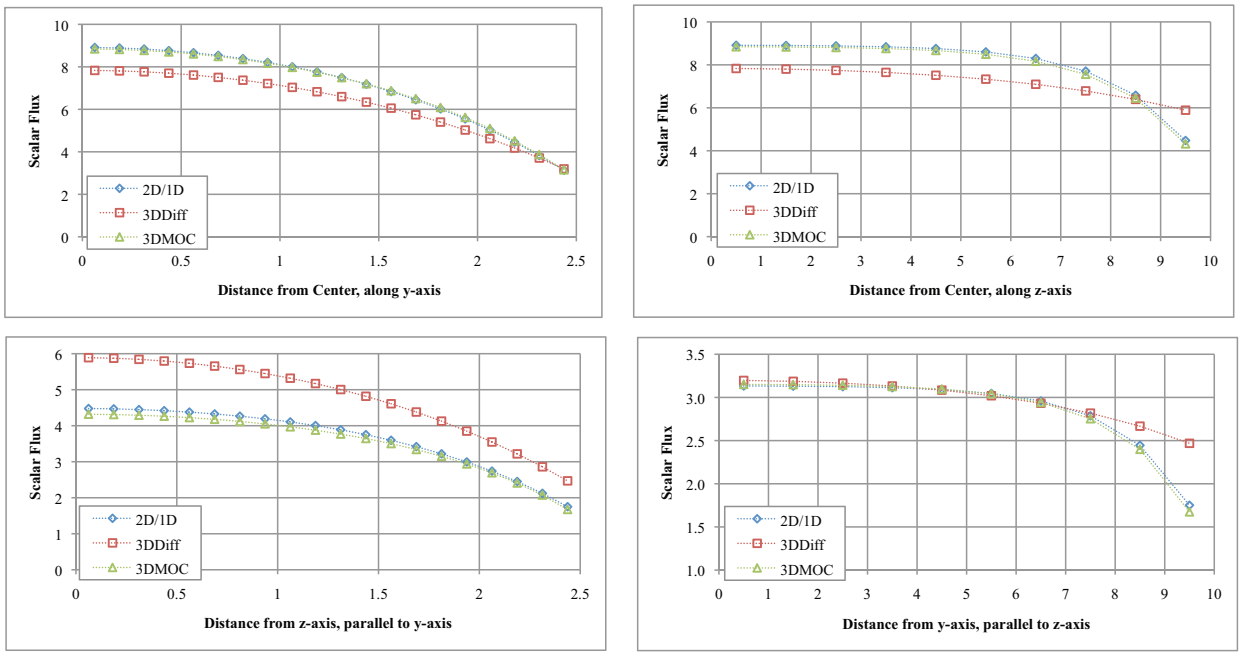

Figure 7: Scalar Flux Plots for $L = 2.5$ cm and Δ_z = 1.0 cm

Top Left: Inner Radial Top Right: Inner Axial
Bottom Left: Outer Radial Bottom Right: Outer Axial

transport accuracy at points where axial boundary layers do not occur, and at worst diffusion accuracy at points where axial boundary layers do occur. This property of the 2D/1D solutions should continue to hold in heterogeneous reactor cores – which possess a multitude of radial boundary layers, but few axial boundary layers.

3. EFFICIENCY AND STABILITY OF THE 2D/1D ITERATIVE SCHEME

To test the stability and convergence rates of the "source iteration with under-relaxation" scheme described in [1], we considered a total of 35 different problems, defined by:

$$
\begin{aligned}
X = Y = Z &= 10 \text{ cm} , \\
\Sigma_t &= 1.0 \text{ cm}^{-1} , \\
\Sigma_s = c &= 0.0,\ 0.25.\ 0.5,\ 0.75,\ \text{and } 0.95 \quad (5 \text{ cases}) , \\
Q &= 0.0 \text{ cm}^{-3} \text{ sec}^{-1} , \\
\Delta_x = \Delta_y &= 0.5 \text{ cm} , \\
\Delta_z &= 10.0,\ 5.0,\ 2.0,\ 1.0,\ 0.5,\ 0.2,\ \text{and } 0.1 \text{ cm} \quad (7 \text{ cases}) .
\end{aligned}
$$

These problems differ by their 5 values of the scattering ratio c and their 7 values of the axial cell width Δ_z, but they all have the solution $\phi_k(x, y) = 0$. To estimate the spectral radius ρ for each of the 35 cases, we started the iterations with a noisy initial guess and monitored the rate at which the solutions converged to 0. The spectral radius ρ was estimated as

$$\rho = \frac{||\phi^{(n+1)}||}{||\phi^{(n)}||} ,$$

where $||\cdot||$ denotes the L_2 norm over all three spatial dimensions, and n (the iteration count) is sufficiently high that the estimate of ρ is stable.

When the iterations are run with $\theta = 1$, there is no under-relaxation, and the iteration method becomes very similar to the original iteration method in DeCART. The estimated and predicted (via Fourier analysis) values of ρ are:

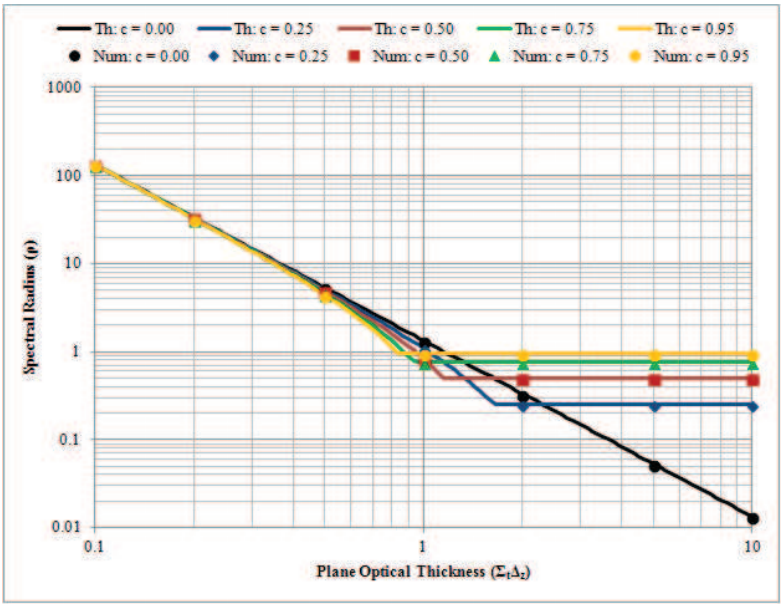

Figure 8: ρ vs $\Sigma_t \Delta_z$ for $\theta = 1$

We see that the estimated values of ρ (symbols) and the theoretical values of ρ (lines) agree quite well, with $\rho = c =$ scattering ratio for $\Sigma_t \Delta_z$ sufficiently large, and $\rho > 1$ (unstable) for roughly $\Sigma_t \Delta_x < 1$.

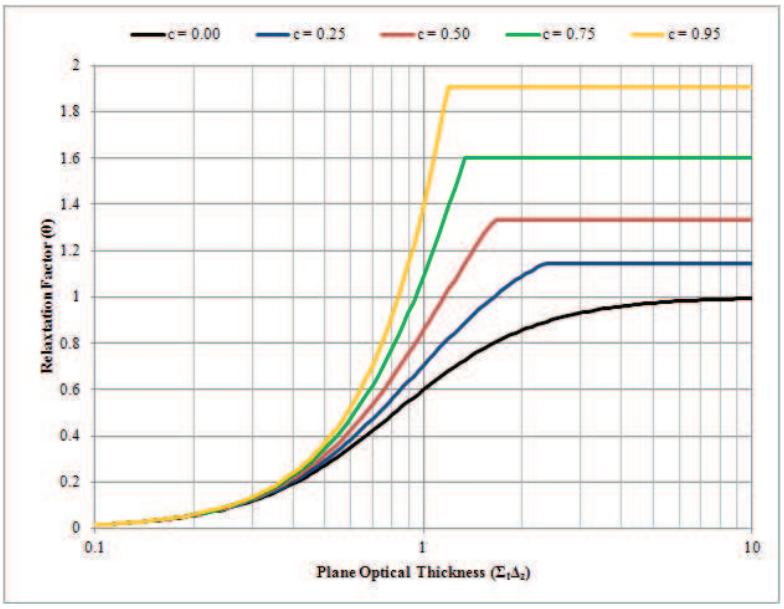

Figure 9: θ_{opt} vs $\Sigma_t \Delta_z$

In Figure 9, the optimal relaxation factor θ_{opt} is plotted as a function of $\Sigma_t\Delta_z$, for 5 different values of the scattering ratio c. As expected, this figure shows that for small $\Sigma_t\Delta_z$ we have $\theta_{opt} < 1$, which corresponds to under-relaxation. Interestingly, for large $\Sigma_t\Delta_z$, we have $\theta_{opt} > 1$, which corresponds to over-relaxation. For large $\Sigma_t\Delta_z$, it is not necessary to over-relax; if one simply uses $\theta = 1$, the theoretical spectral radius $\rho = c$ results. However, the use of $\theta = \theta_{opt}$ does reduce the theoretical spectral radius to $\rho = c/(2 - c)$.

For $\theta = \theta_{opt}$, Figure 10 shows the theoretical (solid lines) and the observed (symbols) estimates of the spectral radius ρ:

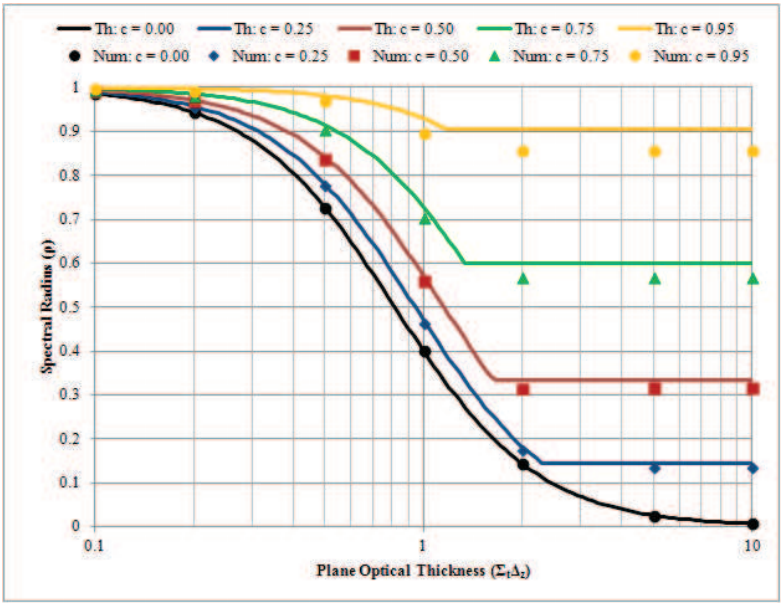

Figure 10: ρ vs $\Sigma_t\Delta_z$ for $\theta = \theta_{opt}$

Again, the agreement between theory and experiment is very good. We have determined that the reason for the faster-than-theoretically-predicted rates of convergence observed experimentally for larger values of $\Sigma_t\Delta_z$ are due to the vacuum boundary conditions. (For large values of Δ_z, the most slowly converging Fourier modes are flat, and these modes are not present unless the system becomes very optically thick.) Overall, the most significant result is that the inclusion of under-relaxation stabilizes the method, and the convergence rates are well- (and conservatively-) predicted by the Fourier analysis.

4. DISCUSSION

We have presented results of 2D/1D and 3D calculations for some geometrically simple problems, showing that (i) the 2D/1D solutions exist and are more accurate than standard diffusion, and (ii) the iterative method described in [1] is stable and behaves as predicted by the Fourier analysis.

To summarize the results of our numerical simulations, they show that the 2D/1D solutions treat "radial" boundary layers (along surfaces whose normals point in a radial direction) with transport accuracy, and "axial" boundary layers (along surfaces whose normals point in an axial direction) with at worst diffusion accuracy. If an axial boundary layer contains strong radial derivatives, then the accuracy of the 2D/1D solution actually increases. This is all that one would hope for, from solving an equation that preserves the correct transport physics in the radial directions and the approximate diffusion physics in the axial direction.

Our simulations also confirm that a key element of stability of the 2D/1D iteration scheme is the under-relaxation step described in [1]. Under-relaxation is never used for iteratively solving standard S_N calculations; the necessary inclusion of this step for solving the 2D/1D equation demonstrates a fundamental difference between this equation and the Boltzmann transport equation.

If the under-relaxation step is not performed, the iteration method used in our simulations becomes quite similar to the original iteration method used in DeCART – and it becomes unstable for sufficiently small Δ_z. Currently, we are considering an accelerated version of the "source iteration with under-relaxation" method that include a low-order 3D "diffusion" calculation, based on the concepts that underly the CMFD and the Coarse Mesh DSA methods [4].

The 2D/1D simulations in this paper were performed on a single radial spatial grid, whereas practical 2D/1D simulations on reactor lattices employ a coarse radial grid (one cell = one pin cell) and a fine radial grid (to resolve the inner structure of a pin cell). Almost certainly, the 2D/1D equation itself should be discretized on the fine radial grid, and the low-order "diffusion" equation in the proposed CMFD method (see the previous paragraph) should be discretized consistently on the coarse radial grid. This important practical issue cannot be discussed in detail here.

The accuracy of the 2D/1D solution depends strongly on the use of the correct diffusion coefficient in the approximate axial derivative term. For problems that are classically diffusive, such as the ones tested here, the our numerical results show that the standard diffusion coefficient $D = 1/3\Sigma_{tr}$ is correct. However, for a reactor lattice, where classic diffusion theory is not valid (because the angular dependence of the neutron flux is much more complicated than linear), the classic formula $D = 1/3\Sigma_{tr}$ (or a homogenized version of this formula) is not justified theoretically. Fortunately, for lattice problems, a systematic asymptotic theory does predict an axial diffusion coefficient [5, 6], and for reactor lattice problems we plan to implement and test that approach.

We intend to move rapidly in the direction of systematically developing, implementing (in MPACT), and testing the necessary generalizations to the 2D/1D method presented here, so that the resulting method will be applicable to reactor lattices. We anticipate that when these generalizations are in place, the resulting 2D/1D method will be an accurate and efficient tool for many 3D reactor simulations.

The resulting 2D/1D solutions will not be identical to solutions of the 3D Boltzmann transport equation, because the 2D/1D transport physics in the axial direction is approximated (by diffusion physics). However, more accurate approximations to the axial derivative term can be envisioned, as was discussed in [1]. In particular, approximations more sophisticated than P_1 (for example, P_3) can be used. In fact, the current KAERI version of DeCART now uses an SP_3 approximation to the transverse leakage term [7].

The main point to emphasize is that many different possibilities exist for approximating the axial leakage term in the 3D Boltzmann transport equation, so that the resulting "2D/1D" equation (i) models practical reactor core problems with sufficient accuracy, and (ii) can be solved more efficiently than the standard 3D Boltzmann transport equation.

ACKNOWLEDGEMENTS

We wish to acknowledge many helpful discussions with Han Joo, Tom Downar, and Bill Martin. Also, we gratefully acknowledge support by the NEUP contract No. DE-AC07-05ID14517, and by the Consortium for Advanced Simulation of Light Water Reactors (www.casl.gov), an Energy Innovation Hub (http://www.energy.gov/hubs) for Modeling and Simulation of Nuclear Reactors under U.S. Department of Energy Contract No. DE-AC05-00OR22725.

REFERENCES

[1] B. Kelley and E.W. Larsen, " 2D/1D Approximations to the Neutron Transport Equation. I: Theory," *Proc. M&C 2013*, Sun Valley, ID, USA, May 5-9 (2013).

[2] B. Kochunas, et al., "Overview of Development and Design of MPACT: Michigan Parallel Characteristics Transport Code," *Proc. M&C 2013*, Sun Valley, ID, USA, May 5-9 (2013).

[3] B. Kochunas, Z. Liu, and T. Downar, "Parallel 3-D Method of Characteristics in MPACT"," *Proc. M&C 2013*, Sun Valley, ID, USA, May 5-9 (2013).

[4] E.W. Larsen and B.W. Kelley, "CMFD and Coarse-Mesh DSA," *Proc. PHYSOR 2012, Advances in Reactor Physics Linking Research, Industry, and Education*, Knoxville, Tennessee, April 15-20, 2012, on CD-ROM, American Nuclear Society, LaGrange Park, IL (2012).

[5] T.J. Trahan and E.W. Larsen, "An Asymptotic Homogenized Neutron Diffusion Approximation I. Theory," *Proc. PHYSOR 2012, Advances in Reactor Physics Linking Research, Industry, and Education*, Knoxville, Tennessee, April 15-20, 2012, on CD-ROM, American Nuclear Society, LaGrange Park, IL (2012).

[6] T.J. Trahan and E.W. Larsen, "An Asymptotic Homogenized Neutron Diffusion Approximation II. Numerical Comparisons," *Proc. PHYSOR 2012, Advances in Reactor Physics Linking Research, Industry, and Education*, Knoxville, Tennessee, April 15-20, 2012, on CD-ROM, American Nuclear Society, LaGrange Park, IL (2012).

[7] J.Y. Cho, K.S. Kim, C.C. Lee, S.Q. Zee, and H.G. Joo, "Axial SP_N and Radial MOC Coupled Whole Core Transport Calculation," *J. Nucl. Sci. and Tech.*, **44**, pp. 1156-1171 (2007).

Submitted to: *Nuclear Science & Engineering*

THE RELATIONSHIP BETWEEN THE CMFD AND THE COARSE-MESH DSA METHODS

by

Edward W. Larsen and Blake W. Kelley

Department of Nuclear Engineering and Radiological Sciences
University of Michigan
Ann Arbor, Michigan 48109-2104 USA
edlarsen@umich.edu, kelleybl@umich.edu

Email: edlarsen@umich.edu
Telephone: (734) 936-0124
Fax: (734) 763-4540

Total number of pages: 31
Number of tables: 0
Number of figures: 17

ABSTRACT

The Coarse Mesh Finite Difference (CMFD) and Diffusion Synthetic Acceleration (DSA) methods are widely-used, independently-developed methods for accelerating the iterative convergence of deterministic neutron transport calculations. In this paper we show that these methods have the following theoretical relationship: if the standard notion of DSA as a "fine mesh" method is straightforwardly generalized to a "coarse mesh" method, then the linearized form of the CMFD method is algebraically equivalent to a coarse-mesh DSA method. We also show theoretically (via Fourier analysis) and experimentally (via simulations) that for fixed-source problems, the coarse mesh DSA and CMFD methods have nearly identical convergence rates. Our numerical results confirm the close theoretically-predicted relationship between these methods.

KEYWORDS: neutron transport, iteration methods, acceleration methods

I. INTRODUCTION

For many years, large-scale deterministic neutron transport codes have used Source Iteration (SI) with an acceleration scheme to iteratively converge the scattering and fission sources [1]. The SI method alone converges rapidly only for problems having high absorption or high leakage probabilities; when the absorption and leakage probabilities are both small (and neutron histories are long), the SI scheme converges extremely slowly. Early acceleration methods included Fine and Coarse-Mesh Rebalance; these were superseded by various forms of Diffusion Synthetic Acceleration (DSA) [1–5]. Still later, the Coarse Mesh Finite Difference (CMFD) method was developed independently [6–9].

Outwardly, the DSA and CMFD methods have certain similarities: both methods define a single iteration to consist of a "high order" transport sweep, followed by a "low-order" diffusion calculation. However, the two methods have significant differences: (i) DSA is linear, and CMFD is nonlinear, (ii) DSA is traditionally used as a "fine grid" method in which the spatial grids for the transport and diffusion calculations are the same, whereas CMFD is normally used as a "coarse grid" method in which the spatial grid for the diffusion equation is coarser than the spatial grid for the transport equation, and (iii) in DSA, the low-order solution is a fine-grid linear correction to the high-order scalar flux, whereas in CMFD, the low-order solution is a coarse-grid volume-averaged scalar flux.

In 2003, Cho and Park Fourier-analyzed a linearized CMFD method [8]. They showed, theoretically and experimentally, that the CMFD method converges rapidly when the coarse cells are less than one mean free path thick; but as the coarse cells become thicker, the method degrades in performance and ultimately diverges. Cho and Park observed that this behavior is qualitatively similar to the convergence properties of an "inconsistent" DSA method, in which (i) the transport and diffusion grids are the same, and (ii) a standard discretization of the diffusion equation is used, which is not "consistent" with the transport discretization [1, 4].

DSA is commonly viewed as a "fine mesh" method (in which the spatial grids for the high order transport and the low-order diffusion equations are the same), but it is easy to allow the low-order diffusion problem to be discretized on a coarser spatial grid. The resulting "Coarse Mesh DSA" (CMDSA) method is usually "inconsistent" – the diffusion discretization is not related to the transport discretization in a way that ensures rapid convergence for all fine or coarse mesh thicknesses. Nonetheless, if the "consistency" issue is put aside, there is no conceptual difficulty implementing the DSA method using a coarser spatial mesh for the low-order diffusion calculation than for the higher-order transport equation.

In this paper we apply the above ideas to show that the CMDSA and CMFD methods have the following theoretical relationship:

1. The linearized form of the CMFD method is algebraically equivalent to a "coarse-mesh DSA" method.
2. A Fourier analysis accurately predicts the convergence properties of the CMDSA method. (This extends the previous work by Cho and Park [8].)
3. In numerical simulations of fixed-source problems, the (linear) CMDSA and (nonlinear) CMFD methods have nearly the same convergence properties. Hence, the Fourier analysis results accurately describe both the linear CMDSA (= linearized CMFD) and the nonlinear CMFD methods.

Thus, rather than being two unrelated methods, DSA and CMFD have close theoretical ties. Of course, there are significant differences – the main one being that the low-order DSA and CMDSA problems are linear, while the low-order CMFD problem is nonlinear. (Because of its nonlinearity, CMFD is easier to apply to the outer iterations of eigenvalue problems – an advantage to CMFD. However, the linear CMDSA method will not become unstable if an angular flux iterate becomes zero or negative – an advantage to CMDSA.) Nonetheless, for problems on which both methods can be used, the Fourier analysis predicts and our numerical results confirm that the two methods have nearly the same convergence properties.

This paper is a revised version of a recent conference paper [10]. The remainder of the paper is summarized as follows. In Section II a 1-D S_N fixed-source problem is described, for which the (linear) CMDSA and (nonlinear) CMFD methods are formulated. In Sec. III the CMFD method is linearized, and the resulting "linearized CMFD" (LCMFD) method is shown to be algebraically equivalent to a CMDSA method. In Section IV the Fourier analysis for the CMDSA method is developed for the Step Characteristic spatial discretization method with p fine spatial cells per coarse cell; and the Fourier analysis is used to predict the spectral radius of this method. (This section reviews the previous work of Cho and Park [8].) Section V presents the results of numerical experiments, confirming the theoretical predictions from Section III and showing that the (linear) CMDSA and (nonlinear) CMFD methods have nearly the same convergence properties. Section VI concludes the paper with a brief discussion.

II. THE CMFD AND CMDSA METHODS

Here we describe the CMFD and CMDSA methods for a planar geometry fixed-source problem on the system $0 \le x \le X$:

$$\mu \frac{\partial \psi}{\partial x}(x,\mu) + \sigma_t(x)\psi(x,\mu) = \frac{\sigma_s(x)}{2} \int_{-1}^{1} \psi(x,\mu')d\mu' + \frac{q(x)}{2} \ , \tag{2.1a}$$

$$\psi(0,\mu) = \psi^b(\mu) \ , \ \ 0 < \mu \le 1 \ , \tag{2.1b}$$

$$\psi(X,\mu) = \psi^b(\mu) \ , \ \ -1 \le \mu < 0 \ . \tag{2.1c}$$

The notation here is standard.

Using the familiar discrete ordinates approximation in angle and an arbitrary weighted diamond approximation in space, we discretize Eqs. (2.1) as follows:

$$\frac{\mu_n}{h_j}\left(\psi_{n,j+1/2}-\psi_{n,j+1/2}\right)+\sigma_{t,j}\psi_{n,j}=\frac{\sigma_{s,j}}{2}\sum_{m=1}^{N}\psi_{m,j}w_m+\frac{q_j}{2}\ , \tag{2.2a}$$

$$\psi_{n,j}=\left(\frac{1+\alpha_{n,j}}{2}\right)\psi_{n,j+1/2}+\left(\frac{1-\alpha_{n,j}}{2}\right)\psi_{n,j-1/2}\ , \tag{2.2b}$$

$$\psi_{n,1/2}=\psi_n^b\ ,\ \ \mu_n>0\ , \tag{2.2c}$$

$$\psi_{n,J+1/2}=\psi_n^b\ ,\ \ \mu_n<0\ . \tag{2.2d}$$

The notation in Eqs. (2.2) is also standard. The subscript j, running over $1\le j\le J$, denotes the (fine) spatial cell, which has width h_j, cross sections $\sigma_{t,j}$ and $\sigma_{s,j}$, and constant internal source q_j. The subscript n, running from $1\le n\le N$, denotes the direction cosine of flight. The constants $\alpha_{n,j}$ determine the specific spatial discretization method, e.g.

$$\alpha_{n,j}=\begin{cases}0 & ,\ \text{Diamond Difference}\ ,\\ \frac{1+e^{-\sigma_{t,j}h_j/\mu_n}}{1-e^{-\sigma_{t,j}h_j/\mu_n}}-\frac{2\mu_n}{\sigma_{t,j}h_j} & ,\ \text{Step Characteristic}\ .\end{cases} \tag{2.3}$$

The CMFD and CMDSA methods begin each iteration with a standard fine-mesh transport sweep. At the beginning of the ℓ^{th} iteration, the fine-mesh cell-averaged scalar fluxes

$$\phi_{0,j}^{(\ell)}=\sum_{n=1}^{N}\psi_{n,j}^{(\ell)}w_n\ ,\ \ 1\le j\le J \tag{2.4}$$

are assumed to be known, either from the previous iteration or from the initial guess if $\ell=0$. Then the following version of Eqs. (2.2):

$$\frac{\mu_n}{h_j}\left(\psi_{n,j+1/2}^{(\ell+1/2)}-\psi_{n,j-1/2}^{(\ell+1/2)}\right)+\sigma_{t,j}\psi_{n,j}^{(\ell+1/2)}=\frac{\sigma_{s,j}}{2}\phi_{0,j}^{(\ell)}+\frac{q_j}{2}\ , \tag{2.5a}$$

$$\psi_{n,j}^{(\ell+1/2)}=\left(\frac{1+\alpha_{n,j}}{2}\right)\psi_{n,j+1/2}^{(\ell+1/2)}+\left(\frac{1-\alpha_{n,j}}{2}\right)\psi_{n,j-1/2}^{(\ell+1/2)}\ , \tag{2.5b}$$

$$\psi_{n,1/2}^{(\ell+1/2)}=\psi_n^b\ ,\ \ \mu_n>0\ , \tag{2.5c}$$

$$\psi_{n,J+1/2}^{(\ell+1/2)}=\psi_n^b\ ,\ \ \mu_n<0\ , \tag{2.5d}$$

is solved by a standard transport sweep for the $\psi^{(\ell+1/2)}$ unknowns. During this sweep, the cell-averaged fluxes and (for CMFD) the cell-edge currents are computed and stored:

$$\phi_{0,j}^{(\ell+1/2)}=\sum_{n=1}^{N}\psi_{n,j}^{(\ell+1/2)}w_n\ , \tag{2.6a}$$

$$\phi_{1,j+1/2}^{(\ell+1/2)}=\sum_{n=1}^{N}\mu_n\psi_{n,j+1/2}^{(\ell+1/2)}w_n\ . \tag{2.6b}$$

In the classic Source Iteration (SI) method, the fine-mesh scalar fluxes for iteration $\ell+1$ are defined simply from Eqs. (2.6) by

$$\phi_{0,j}^{(\ell+1)} = \phi_{0,j}^{(\ell+1/2)} \ , \ \ 1 \le j \le J \ . \tag{2.7}$$

However, this method converges slowly for problems in which the system is optically thick and highly scattering. The CMDSA and CMFD methods retain Eqs. (2.5) and (2.6) but not Eq. (2.7); this definition of $\phi_{0,j}^{(\ell+1)}$ is replaced by a more sophisticated calculation that can significantly reduce the total number of iterations.

To proceed, we introduce the notation for the coarse spatial grid. This grid contains $K \le J$ disjoint "coarse" spatial cells, each consisting of a contiguous union of fine-mesh cells. If p_k = the number of fine cells in coarse cell k (ordered from left to right as k increases), then for $0 \le k \le K$:

$$P_0 = 0 \ , \tag{2.8a}$$

$$P_k = \sum_{k'=1}^{k} p_{k'} = \text{the number of fine cells in the first } k \text{ coarse cells} \ , \tag{2.8b}$$

$$P_K = J = \text{the total number of fine cells} \ , \tag{2.8c}$$

and

$$\begin{aligned} X_{k+1/2} &= x_{P_k+1/2} \\ &= \text{the right edge of the } k^{th} \text{ coarse cell} \\ &= \text{the left edge of the } (k+1)^{st} \text{ coarse cell} \ . \end{aligned} \tag{2.9}$$

The fine and coarse spatial cells are depicted in Figure 1:

Insert Figure 1 about here.

To proceed, we introduce the notation

$$\sum_{j \in k} = \sum_{j=P_k+1}^{P_{k+1}} = \text{the sum over all fine cells } j \text{ in coarse cell } k \ , \tag{2.10}$$

and we define the coarse cell quantities:

$$\Delta_k = \sum_{j \in k} h_j = \text{width of coarse cell } k \ , \tag{2.11a}$$

$$\Phi_{0,k} = \frac{1}{\Delta_k} \sum_{j \in k} \phi_{0,j} h_j = \text{volume-averaged scalar flux in coarse cell } k \ , \tag{2.11b}$$

$$Q_k = \frac{1}{\Delta_k} \sum_{j \in k} q_j h_j = \text{volume-averaged source in coarse cell } k \ , \tag{2.11c}$$

$$\Phi_{1,k+1/2} = \phi_{1,P_k+1/2} = \text{current on the right edge of coarse cell } k \ , \tag{2.11d}$$

$$\begin{aligned} \Sigma_{u,k} &= \frac{1}{\Delta_k} \sum_{j \in k} \sigma_{u,j} h_j \\ &= \text{volume-averaged cross section in coarse cell } k \quad (u = t, s, \gamma) \ , \end{aligned} \tag{2.11e}$$

$$\begin{aligned} \Sigma_{u,k}^{(\ell+1/2)} &= \frac{\sum_{j \in k} \sigma_{u,j} \phi_{0,j}^{(\ell+1/2)} h_j}{\sum_{j \in k} \phi_{0,j}^{(\ell+1/2)} h_j} \\ &= \text{flux-weighted cross section in coarse cell } k \quad (u = t, s, \gamma) \ . \end{aligned} \tag{2.11f}$$

(Fine-cell quantities are denoted by lower-case letters; coarse-cell quantities are denoted by upper-case letters.)

2.1 Coarse Mesh Finite Difference (CMFD)

To derive the CMFD method, we operate on Eq. (2.5a) by $\sum_{n=1}^{N} (\cdot) w_n$ and get

$$\frac{1}{h_j} \left(\phi_{1,j+1/2}^{(\ell+1/2)} - \phi_{1,j-1/2}^{(\ell+1/2)} \right) + \sigma_{t,j} \phi_{0,j}^{(\ell+1/2)} = \sigma_{s,j} \phi_{0,j}^{(\ell)} + q_j \ . \tag{2.12}$$

Then we operate on Eq. (2.12) by $\sum_{j \in k} (\cdot) h_j$. Using the definitions (2.11), we obtain:

$$\Phi_{1,k+1/2}^{(\ell+1/2)} - \Phi_{1,k-1/2}^{(\ell+1/2)} + \Sigma_{t,k}^{(\ell+1/2)} \Phi_{0,k}^{(\ell+1/2)} \Delta_k = \Sigma_{s,k}^{(\ell)} \Phi_{0,k}^{(\ell)} \Delta_k + Q_k \Delta_k \ . \tag{2.13}$$

Next, we define $\hat{D}_{k+1/2}^{(\ell+1/2)}$ at each interior coarse cell edge ($1 \le k \le K-1$) by:

$$\begin{aligned} \Phi_{1,k+1/2}^{(\ell+1/2)} = -\frac{2}{3} &\left(\frac{\Phi_{0,k+1}^{(\ell+1/2)} - \Phi_{0,k}^{(\ell+1/2)}}{\Sigma_{t,k+1}^{(\ell+1/2)} \Delta_{k+1} + \Sigma_{t,k}^{(\ell+1/2)} \Delta_k} \right) \\ &+ \hat{D}_{k+1/2}^{(\ell+1/2)} \left(\Phi_{0,k+1}^{(\ell+1/2)} + \Phi_{0,k}^{(\ell+1/2)} \right) \ . \end{aligned} \tag{2.14}$$

(We note that $\hat{D}_{k+1/2}^{(\ell+1/2)}$ can be calculated at the conclusion of each transport sweep, and that this quantity is a *transport correction to Fick's Law* – which vanishes if Fick's Law exactly relates the current to the derivative of the scalar flux.) At the left edge of the system, we define $B_{1/2}^{(\ell+1/2)}$ by

$$\begin{aligned} 2\Phi_{1,1/2}^{+} &= 2 \sum_{\mu_n > 0} \mu_n \psi_n^b w_n \\ &= \sum_{n=1}^{N} \left(\mu_n + |\mu_n| \right) \psi_{n,1/2}^{(\ell+1/2)} w_n \\ &= \Phi_{1,1/2}^{(\ell+1/2)} + \left(\frac{\sum_{n=1}^{N} |\mu_n| \psi_{n,1/2}^{(\ell+1/2)} w_n}{\sum_{n=1}^{N} \Psi_{n,1}^{(\ell+1/2)} w_n} \right) \Phi_{0,1}^{(\ell+1/2)} \\ &= \Phi_{1,1/2}^{(\ell+1/2)} + \left(B_{1/2}^{(\ell+1/2)} \right) \Phi_{0,1}^{(\ell+1/2)} \ , \end{aligned} \tag{2.15a}$$

and at the right edge of the system, we define $B_{K+1/2}^{(\ell+1/2)}$ by

$$
\begin{aligned}
2\Phi^{+}_{1,K+1/2} &= 2\sum_{\mu_n<0} |\mu_n|\psi^b_n w_n \\
&= \sum_{n=1}^{N} \big(-\mu_n + |\mu_n| \big) \psi^{(\ell+1/2)}_{n,J+1/2} w_n \\
&= -\Phi^{(\ell+1/2)}_{1,K+1/2} + \left(\frac{\sum_{n=1}^{N} |\mu_n| \psi^{(\ell+1/2)}_{n,J+1/2} w_n}{\sum_{n=1}^{N} \Psi^{(\ell+1/2)}_{n,K} w_n} \right) \Phi^{(\ell+1/2)}_{0,K} \\
&= -\Phi^{(\ell+1/2)}_{1,K+1/2} + \left(B^{(\ell+1/2)}_{K+1/2} \right) \Phi^{(\ell+1/2)}_{0,K} \ . \qquad (2.15b)
\end{aligned}
$$

At the conclusion of the transport sweep, (i) the $\psi^{(\ell+1/2)}$ quantities have been determined, (ii) Eqs. (2.13) are satisfied for each coarse cell k, (iii) Eq. (2.14) defines $\hat{D}^{(\ell+1/2)}_{k+1/2}$ at interior coarse cell edge, and (iv) Eqs. (2.15) define $B^{(\ell+1/2)}_{1/2}$ and $B^{(\ell+1/2)}_{K+1/2}$ at the left and right edges of the system. It is now possible to define, in terms of these equations, *acceleration* equations for the coarse cell-averaged scalar fluxes and the coarse cell-edge currents.

In the CMFD method, $\Phi^{(\ell+1)}_{0,k}$ and $\Phi^{(\ell+1)}_{1,k+1/2}$ are defined to be the solution of the following altered versions of Eqs. (2.13)-(2.15):

$$
\Phi^{(\ell+1)}_{1,k+1/2} - \Phi^{(\ell+1)}_{1,k-1/2} + \Sigma^{(\ell+1/2)}_{t,k} \Phi^{(\ell+1)}_{0,k} \Delta_k = \Sigma^{(\ell+1/2)}_{s,k} \Phi^{(\ell+1)}_{0,k} \Delta_k + Q_k \Delta_k \ , \qquad (2.16a)
$$

$$
\Phi^{(\ell+1)}_{1,k+1/2} = -\frac{2}{3} \left(\frac{\Phi^{(\ell+1)}_{0,k+1} - \Phi^{(\ell+1)}_{0,k}}{\Sigma^{(\ell+1/2)}_{t,k+1} \Delta_{k+1} + \Sigma^{(\ell+1/2)}_{t,k} \Delta_k} \right) + \hat{D}^{(\ell+1/2)}_{k+1/2} \left(\Phi^{(\ell+1)}_{0,k+1} + \Phi^{(\ell+1)}_{0,k} \right) \ , \qquad (2.16b)
$$

$$
2\Phi^{+}_{1,1/2} = \Phi^{(\ell+1)}_{1,1/2} + \big(B^{(\ell+1/2)}_{1/2} \big) \Phi^{(\ell+1)}_{0,1} \ , \qquad (2.16c)
$$

$$
2\Phi^{+}_{1,K+1/2} = -\Phi^{(\ell+1)}_{1,K+1/2} + \big(B^{(\ell+1/2)}_{K+1/2} \big) \Phi^{(\ell+1)}_{0,J} \ . \qquad (2.16d)
$$

The coarse cell-edge currents in these equations, $\Phi^{(\ell+1)}_{1,k+1/2}$, can be algebraically eliminated, yielding a tri-diagonal system of K equations for the coarse cell-averaged scalar fluxes $\Phi^{(\ell+1)}_{0,k}$, $1 \le k \le K$. After these quantities are obtained, the accelerated fine-cell scalar fluxes are defined as

$$
\phi^{(\ell+1)}_{0,j} = \phi^{(\ell+1/2)}_{0,j} \left(\frac{\Phi^{(\ell+1)}_{0,k}}{\Phi^{(\ell+1/2)}_{0,k}} \right) \ , \quad j \in k \ , \quad 1 \le k \le K \ . \qquad (2.17)
$$

This completes the description of the CMFD method. The logic underlying this method is that if the transport corrections to diffusion $\hat{D}^{(\ell+1/2)}_{k+1/2}$ are small, then these quantities can be lagged in Eq. (2.16b), and the resulting iterative method will converge rapidly. For problems in which the coarse cells are not optically thick, this logic is valid, as we show below.

2.1 Coarse Mesh Diffusion Synthetic Acceleration (CMDSA)

To derive the CMDSA method, we define the exact fine-mesh iteration errors after the ℓ^{th} transport sweep:

$$f_{1,j+1/2} = \phi_{1,j+1/2} - \phi_{1,j+1/2}^{(\ell+1/2)} \,, \tag{2.18a}$$

$$f_{0,j} = \phi_{0,j} - \phi_{0,j}^{(\ell+1/2)} \,. \tag{2.18b}$$

These can easily be shown, using Eq. (2.5a), to satisfy:

$$\frac{1}{h_j}\big(f_{1,j+1/2} - f_{1,j-1/2}\big) + \sigma_{a,j} f_{0,j} = \sigma_{s,j}\left(\phi_{0,j}^{(\ell+1/2)} - \phi_{0,j}^{(\ell)}\right) \;,\quad 1 \le k \le K \,.$$

Equivalently,

$$\frac{1}{h_j}\big(f_{1,j+1/2} - f_{1,j-1/2}\big) + \Sigma_{a,k} f_{0,j} = \sigma_{s,j}\left(\phi_{0,j}^{(\ell+1/2)} - \phi_{0,j}^{(\ell)}\right) + \big(\Sigma_{a,k} - \sigma_{a,j}\big) f_{0,j} \,. \tag{2.19}$$

Operating on this result by $\sum_{j\in k}(\cdot)h_j$ and defining the coarse cell quantities

$$F_{0,k} = \frac{1}{\Delta_k}\sum_{j\in k} f_{0,j} h_j \,, \tag{2.20a}$$

$$F_{1,k+1/2} = f_{1,P_k+1/2} \,, \tag{2.20b}$$

we get:

$$\begin{aligned} F_{1,k+1/2} - F_{1,k-1/2} + \Sigma_{a,k} F_{0,k} \Delta_k = & \sum_{j\in k} \sigma_{s,j}\left(\phi_{0,j}^{(\ell+1/2)} - \phi_{0,j}^{(\ell)}\right) h_j \\ & + \sum_{j\in k} \big(\Sigma_{a,k} - \sigma_{a,j}\big) f_{0,j} h_j \,. \end{aligned} \tag{2.21}$$

Eqs. (2.21) are J equations for the $2J+1$ quantities $F_{0,k}$ and $F_{1,k+1/2}$. (Also, the fine-mesh quantities $f_{0,j}$ on the right side of these equations are not known.)

In the CMDSA method, $F_{0,k}^{(\ell+1)}$ and $F_{1,k+1/2}^{(\ell+1)}$ are determined by the following version of Eq. (2.21):

$$\begin{aligned} F_{1,k+1/2}^{(\ell+1)} - F_{1,k-1/2}^{(\ell+1)} + \Sigma_{a,k} F_{0,k}^{(\ell+1)} \Delta_k = & \sum_{j\in k} \sigma_{s,j}\left(\phi_{0,j}^{(\ell+1/2)} - \phi_{0,j}^{(\ell)}\right) h_j \,, \\ & 1 \le k \le K \,, \end{aligned} \tag{2.22a}$$

together with the "diffusion" approximation:

$$F_{1,k+1/2}^{(\ell+1)} = -\frac{2}{3}\left(\frac{F_{0,k+1}^{(\ell+1)} + F_{0,k}^{(\ell+1)}}{\Sigma_{t,k+1}\Delta_{k+1} + \Sigma_{t,k}\Delta_k}\right) \quad,\quad 1 \le k \le K-1 \,, \tag{2.22b}$$

$$0 = F_{1,1/2}^{(\ell+1)} + \beta F_{0,1}^{(\ell+1)} \,, \tag{2.22c}$$

$$0 = -F_{1,K+1/2}^{(\ell+1)} + \beta F_{0,K}^{(\ell+1)} \,, \tag{2.22d}$$

where

$$\beta \equiv \frac{1}{2}\left(\sum_{n=1}^{N} |\mu_n| w_n\right) \approx \frac{1}{2} \; . \tag{2.23}$$

The cell-edge current corrections $F_{1,k+1/2}^{(\ell+1)}$ in Eqs. (2.22) can be algebraically eliminated, yielding a tridiagonal system of K equations for $F_{0,k}^{(\ell+1)}$, $1 \le k \le K$. After these quantities are calculated, the accelerated fine-cell scalar fluxes are defined as

$$\phi_{0,j}^{(\ell+1)} = \phi_{0,j}^{(\ell+1/2)} + F_{0,k}^{(\ell+1)} \; , \quad j \in k \; , \quad 1 \le k \le K \; . \tag{2.24}$$

This completes the description of the CMDSA method. The logic underlying this method is that if (i) the second term on the right side of Eq. (2.21) is sufficiently small that it can be neglected, and (ii) the discrete Fick's Law in Eq. (2.22b) is sufficiently accurate, then the solution of Eqs. (2.22) should yield a sufficiently accurate coarse-grid correction to the fine-grid scalar fluxes that the resulting iteration scheme will converge rapidly. For problems in which the coarse cells are not optically thick, this logic is valid, as we show below.

III. THE LINEARIZED COARSE MESH FINITE DIFFERENCE (LCMFD) METHOD

To describe the linearization procedure, we consider the transport problem defined by Eqs. (2.2), with

$$q_j = \sigma_{a,j}\Lambda + \varepsilon \tilde{q}_j \; , \tag{3.1a}$$

$$\psi_n^b = \frac{\Lambda}{2} + \varepsilon \tilde{\psi}_n^b \; , \tag{3.1b}$$

where Λ is an arbitrary constant and $\varepsilon \ll 1$. For $\varepsilon = 0$, the resulting problem has the exact "flat" solution

$$\psi_{n,j} = \psi_{n,j+1/2} = \frac{\Lambda}{2} \; .$$

If we set

$$\psi_{n,j} = \frac{\Lambda}{2} + \varepsilon \tilde{\psi}_{n,j} \; , \tag{3.2a}$$

$$\psi_{n,j+1/2} = \frac{\Lambda}{2} + \varepsilon \tilde{\psi}_{n,j+1/2} \; , \tag{3.2b}$$

then Eqs. (2.2) for $\psi_{n,j}$ and $\psi_{n,j+1/2}$ easily become

$$\frac{\mu_n}{h_j}\left(\tilde{\psi}_{n,j+1/2} - \tilde{\psi}_{n,j+1/2}\right) + \sigma_{t,j}\tilde{\psi}_{n,j} = \frac{\sigma_{s,j}}{2}\sum_{m=1}^{N} \tilde{\psi}_{m,j} w_m + \frac{\tilde{q}_j}{2} \; , \tag{3.3a}$$

$$\tilde{\psi}_{n,j} = \left(\frac{1+\alpha_{n,j}}{2}\right)\tilde{\psi}_{n,j+1/2} + \left(\frac{1-\alpha_{n,j}}{2}\right)\tilde{\psi}_{n,j-1/2} \; , \tag{3.3b}$$

$$\tilde{\psi}_{n,1/2} = \tilde{\psi}^b_n \ , \quad \mu_n > 0 \ , \tag{3.3c}$$

$$\tilde{\psi}_{n,J+1/2} = \tilde{\psi}^b_n \ , \quad \mu_n < 0 \ . \tag{3.3d}$$

These equations are identical to (2.2), except that ψ and q have been replaced by $\tilde{\psi}$ and $\tilde{q}$. (Of course, this happens because Eqs. (2.2) are linear.)

Because the CMDSA method is linear, the CMDSA equations obtained by introducing Eqs. (3.1) and (3.2) are also the same as the original equations, but with ψ's, ϕ's, and q's replaced by $\tilde{\psi}$'s, $\tilde{\phi}$'s, and $\tilde{q}$'s. Explicitly, the fine-mesh transport sweep (2.5) becomes

$$\frac{\mu_n}{h_j}\left(\tilde{\psi}^{(\ell+1/2)}_{n,j+1/2} - \tilde{\psi}^{(\ell+1/2)}_{n,j-1/2}\right) + \sigma_{t,j}\tilde{\psi}^{(\ell+1/2)}_{n,j} = \frac{\sigma_{s,j}}{2}\tilde{\phi}^{(\ell)}_{0,j} + \frac{\tilde{q}_j}{2} \ , \tag{3.4a}$$

$$\tilde{\psi}^{(\ell+1/2)}_{n,j} = \left(\frac{1+\alpha_{n,j}}{2}\right)\tilde{\psi}^{(\ell+1/2)}_{n,j+1/2} + \left(\frac{1-\alpha_{n,j}}{2}\right)\tilde{\psi}^{(\ell+1/2)}_{n,j-1/2} \ , \tag{3.4b}$$

$$\tilde{\psi}^{(\ell+1/2)}_{n,1/2} = \tilde{\psi}^b_n \ , \quad \mu_n > 0 \ , \tag{3.4c}$$

$$\tilde{\psi}^{(\ell+1/2)}_{n,J+1/2} = \tilde{\psi}^b_n \ , \quad \mu_n < 0 \ , \tag{3.4d}$$

the "updated" scalar fluxes are

$$\tilde{\phi}^{(\ell+1/2)}_{0,j} = \sum_{n=1}^{N} \tilde{\psi}^{(\ell+1/2)}_{n,j} w_n \ , \tag{3.5}$$

the low-order coarse-grid "diffusion" Eqs. (2.22) (with $\tilde{F} = \varepsilon F$) become

$$\tilde{F}^{(\ell+1)}_{1,k+1/2} - \tilde{F}^{(\ell+1)}_{1,k-1/2} + \Sigma_{a,k}\tilde{F}^{(\ell+1)}_{0,k}\Delta_k = \sum_{j\in k}\sigma_{s,j}\left(\tilde{\phi}^{(\ell+1/2)}_{0,j} - \tilde{\phi}^{(\ell)}_{0,j}\right)h_j \ , \quad 1 \le k \le K \ , \tag{3.6a}$$

$$\tilde{F}^{(\ell+1)}_{1,k+1/2} = -\frac{2}{3}\left(\frac{\tilde{F}^{(\ell+1)}_{0,k+1} - \tilde{F}^{(\ell+1)}_{0,k}}{\Sigma_{t,k+1}\Delta_{k+1} + \Sigma_{t,k}\Delta_k}\right) \ , \quad 1 \le k \le K-1 \ , \tag{3.6b}$$

$$0 = \tilde{F}^{(\ell+1)}_{1,1/2} + \beta\tilde{F}^{(\ell+1)}_{0.1} \ , \tag{3.6c}$$

$$0 = -\tilde{F}^{(\ell+1)}_{1,K+1/2} + \beta\tilde{F}^{(\ell+1)}_{0,K} \ , \tag{3.6d}$$

and the fine-grid, accelerated scalar flux equation (2.24) becomes

$$\tilde{\phi}^{(\ell+1)}_{0,j} = \tilde{\phi}^{(\ell+1/2)}_{0,j} + \tilde{F}^{(\ell+1)}_{0,k} \ , \quad j \in k \ , \quad 1 \le k \le K \ . \tag{3.7}$$

To repeat, these equations are identical to the original equations, except that all quantities scaled by ε now have a tilde. This occurs because, like the original transport problem, the CMDSA equations are linear.

The CMFD method however is nonlinear – this method is altered when Eqs. (3.1) and (3.2) are introduced and the resulting equations are expanded in powers of ε. For the CMFD method, the fine-mesh transport sweep and the resulting updated scalar flux equations are the same as with CMDSA, and are described by Eqs. (3.4) and (3.5).

However, introducing Eqs. (3.1) and (3.2) into (2.16) and expanding in ε, we obtain a different set of low-order diffusion equations for $\tilde{\Phi}_{0,k}^{(\ell+1)}$. A key identity is:

$$\begin{aligned}
\Sigma_{a,k}^{(\ell+1/2)}\Phi_{0,k}^{(\ell+1)} &= \frac{\sum_{j\in k}\sigma_{a,j}\left(\Lambda+\varepsilon\tilde{\phi}_{0,j}^{(\ell+1/2)}\right)h_j}{\sum_{j\in k}\left(\Lambda+\varepsilon\tilde{\phi}_{0,j}^{(\ell+1/2)}\right)h_j}\left[\Lambda+\varepsilon\tilde{\Phi}_{0,k}^{(\ell+1)}\right] \\
&= \frac{\Lambda\Sigma_{a,k}\Delta_k+\varepsilon\sum_{j\in k}\sigma_{a,j}\tilde{\phi}_{0,j}^{(\ell+1/2)}h_j}{\Lambda\Delta_k+\varepsilon\sum_{j\in k}\tilde{\phi}_{0,j}^{(\ell+1/2)}h_j}\left[\Lambda+\varepsilon\tilde{\Phi}_{0,k}^{(\ell+1)}\right] \\
&= \cdots \\
&= \Sigma_{a,k}\Lambda+\varepsilon\left[\frac{1}{\Delta_k}\sum_{j\in k}(\sigma_{a,j}-\Sigma_{a,k})\tilde{\phi}_{0,j}^{(\ell+1/2)}h_j+\Sigma_{a,k}\tilde{\Phi}_{0,k}^{(\ell+1)}\right] . \qquad (3.8)
\end{aligned}$$

Thus, Eq. (2.16a) becomes:

$$\begin{aligned}
&\varepsilon\tilde{\Phi}_{1,k+1/2}^{(\ell+1)}-\varepsilon\tilde{\Phi}_{1,k-1/2}^{(\ell+1)}+\Sigma_{a,k}\Lambda\Delta_k+\varepsilon\left[\sum_{j\in k}\big(\sigma_{a,j}-\Sigma_{a,k}\big)\tilde{\phi}_{0,j}^{(\ell+1/2)}h_j+\Sigma_{a,k}\tilde{\Phi}_{0,k}^{(\ell+1)}\Delta_k\right] \\
&\qquad = \sum_{j\in k}\big(\sigma_{a,j}\Lambda+\varepsilon\tilde{q}_j\big)h_j \\
&\qquad = \big(\Sigma_{a,k}\Lambda+\varepsilon\tilde{Q}_k\big)\Delta_k ,
\end{aligned}$$

or:

$$\begin{aligned}
&\tilde{\Phi}_{1,k+1/2}^{(\ell+1)}-\tilde{\Phi}_{1,k-1/2}^{(\ell+1)}+\Sigma_{a,k}\tilde{\Phi}_{0,k}^{(\ell+1)}\Delta_k \\
&\qquad = \tilde{Q}_k\Delta_k+\sum_{j\in k}\big(\Sigma_{a,k}-\sigma_{a,j}\big)\tilde{\phi}_{0,j}^{(\ell+1/2)}h_j . \qquad (3.9)
\end{aligned}$$

Next, Eq. (2.14) for $\hat{D}_{k+1/2}^{(\ell+1/2)}$ yields

$$\varepsilon\tilde{\Phi}_{1,k+1/2}^{(\ell+1/2)} = -\frac{2}{3}\left(\frac{\varepsilon\big(\tilde{\Phi}_{0,k+1}^{(\ell+1/2)}-\tilde{\Phi}_{0,k}^{(\ell+1/2)}\big)}{\Sigma_{t,k+1}\Delta_{k+1}+\Sigma_{t,k}\Delta_k+O(\varepsilon)}\right)+\hat{D}_{k+1/2}^{(\ell+1/2)}\big(2\Lambda+O(\varepsilon)\big)$$

or:

$$\hat{D}_{k+1/2}^{(\ell+1/2)} = \frac{\varepsilon}{2\Lambda}\left[\tilde{\Phi}_{1,k+1/2}^{(\ell+1/2)}+\frac{2}{3}\left(\frac{\tilde{\Phi}_{0,k+1}^{(\ell+1/2)}-\tilde{\Phi}_{0,k}^{(\ell+1/2)}}{\Sigma_{t,k+1}\Delta_{k+1}+\Sigma_{t,k}\Delta_k}\right)\right]+O(\varepsilon^2) . \qquad (3.10)$$

Using this result in Eq. (2.16b), we obtain for $1\le k\le K-1$:

$$\begin{aligned}
\tilde{\Phi}_{1,k+1/2}^{(\ell+1)} &= -\frac{2}{3}\left(\frac{\tilde{\Phi}_{0,k+1}^{(\ell+1)}-\tilde{\Phi}_{0,k}^{(\ell+1)}}{\Sigma_{t,k+1}\Delta_{k+1}+\Sigma_{t,k}\Delta_k}\right) \\
&\quad +\tilde{\Phi}_{1,k+1/2}^{(\ell+1/2)}+\frac{2}{3}\left(\frac{\tilde{\Phi}_{0,k+1}^{(\ell+1/2)}-\tilde{\Phi}_{0,k}^{(\ell+1/2)}}{\Sigma_{t,k+1}\Delta_{k+1}+\Sigma_{t,k}\Delta_k}\right) . \qquad (3.11)
\end{aligned}$$

Next, introducing Eqs. (3.1) and (3.2) into Eq. (2.16c), we get

$$2\sum_{\mu_n>0}\mu_n\left(\frac{\Lambda}{2}+\varepsilon\tilde{\psi}_n^b\right)w_n=\varepsilon\tilde{\Phi}_{1,1/2}^{(\ell+1)} + \frac{\sum_{n=1}^{N}|\mu_n|\left(\frac{\Lambda}{2}+\varepsilon\tilde{\psi}_{n,1/2}^{(\ell+1/2)}\right)w_n}{\Lambda+\varepsilon\tilde{\Phi}_{0,1}^{(\ell+1/2)}}\left(\Lambda+\varepsilon\tilde{\Phi}_{0,1}^{(\ell+1)}\right) .$$

Expanding this equation in ε and discarding the $O(\varepsilon^2)$ terms, we obtain

$$\tilde{\Phi}_{1,1/2}^{(\ell+1)}+\beta\tilde{\Phi}_{0,1}^{(\ell+1)}=\tilde{\Phi}_{1,1/2}^{(\ell+1/2)}+\beta\tilde{\Phi}_{0,1}^{(\ell+1/2)} . \tag{3.12a}$$

At the right edge of the system, a similar result holds:

$$-\tilde{\Phi}_{1,K+1/2}^{(\ell+1)}+\beta\tilde{\Phi}_{0,J}^{(\ell+1)}=-\tilde{\Phi}_{1,K+1/2}^{(\ell+1/2)}+\beta\tilde{\Phi}_{0,K}^{(\ell+1/2)} . \tag{3.12b}$$

Finally, the fine-grid acceleration Eq. (2.17) becomes, for $j\in k$:

$$\Lambda+\varepsilon\tilde{\phi}_{0,j}^{(\ell+1)}=\left(\Lambda+\varepsilon\tilde{\phi}_{0,j}^{(\ell+1/2)}\right)\left(\frac{\Lambda+\varepsilon\tilde{\Phi}_{0,k}^{(\ell+1)}}{\Lambda+\varepsilon\tilde{\Phi}_{0,k}^{(\ell+1/2)}}\right) . \tag{3.13}$$

Expanding in powers of ε and dropping terms of $O(\varepsilon^2)$, we get

$$\tilde{\phi}_{0,j}^{(\ell+1)}=\tilde{\phi}_{0,j}^{(\ell+1/2)}+\left(\tilde{\Phi}_{0,k}^{(\ell+1)}-\tilde{\Phi}_{0,k}^{(\ell+1/2)}\right) , \quad j\in k , \quad 1\le k\le K . \tag{3.14}$$

Thus, the linearized CMFD method is defined by:

1. Transport sweep: Eqs. (3.4)
2. Updated scalar flux: Eq. (3.5)
3. Low-order coarse-grid diffusion equation: Eqs. (3.9), (3.11), (3.12)
4. Accelerated fine-grid scalar fluxes: Eq. (3.14)

The first two (transport sweep) steps [Eqs. (3.4) and (3.5)] are identical for the CMDSA and LCMFD methods. To establish the connection between the acceleration steps of the two methods, we shall show that:

$$\tilde{F}_{0,k}^{(\ell+1)}=\tilde{\Phi}_{0,k}^{(\ell+1)}-\tilde{\Phi}_{0,k}^{(\ell+1/2)} , \tag{3.15a}$$

$$\tilde{F}_{1,k+1/2}^{(\ell+1)}=\tilde{\Phi}_{1,k+1/2}^{(\ell+1)}-\tilde{\Phi}_{1,k+1/2}^{(\ell+1/2)} . \tag{3.15b}$$

More precisely, the low-order CMDSA Eqs. (2.22) and (2.24) are defined for $\tilde{F}_{0,k}^{(\ell+1)}$ and $\tilde{F}_{1,k+1/2}^{(\ell+1)}$, while the low-order LCMFD Eqs. (3.9), (3.11), (3.12), and (3.14) are defined for $\tilde{\Phi}_{0,k}^{(\ell+1)}$ and $\tilde{\Phi}_{1,k+1/2}^{(\ell+1)}$. We use Eqs. (3.15) to show that the LCMFD low-order acceleration equations are algebraically equivalent to the CMDSA low-order acceleration equations.

At the end of a transport sweep, Eq. (3.4a) holds, so

$$\frac{1}{h_j}\left(\tilde{\phi}^{(\ell+1/2)}_{1,j+1/2}-\tilde{\phi}^{(\ell+1/2)}_{1,j-1/2}\right)+\sigma_{t,j}\tilde{\phi}^{(\ell+1/2)}_{0,j}=\sigma_{s,j}\tilde{\phi}^{(\ell)}_{0,j}+\tilde{q}_j\ .$$

Equivalently,

$$\begin{aligned}\frac{1}{h_j}\left(\tilde{\phi}^{(\ell+1/2)}_{1,j+1/2}-\tilde{\phi}^{(\ell+1/2)}_{1,j-1/2}\right)+\Sigma_{a,k}\tilde{\phi}^{(\ell+1/2)}_{0,j}&=\sigma_{s,j}\left(\tilde{\phi}^{(\ell)}_{0,j}-\tilde{\phi}^{(\ell+1/2)}_{0,j}\right)+\tilde{q}_j\\&\quad+\left(\Sigma_{a,k}-\sigma_{a,j}\right)\tilde{\phi}^{(\ell+1/2)}_{0,j}\ .\end{aligned}\tag{3.16}$$

Operating by $\sum_{j\in k}(\cdot)h_j$, we obtain

$$\begin{aligned}\tilde{\Phi}^{(\ell+1/2)}_{1,k+1/2}-\tilde{\Phi}^{(\ell+1/2)}_{1,k-1/2}+\Sigma_{a,k}\tilde{\Phi}^{(\ell+1/2)}_{0,k}\Delta_k&=\sum_{j\in k}\sigma_{s,j}\left(\tilde{\phi}^{(\ell)}_{0,j}-\tilde{\phi}^{(\ell+1/2)}_{0,j}\right)h_j+\tilde{Q}_k\Delta_k\\&\quad+\sum_{j\in k}\left(\Sigma_{a,k}-\sigma_{a,j}\right)\tilde{\phi}^{(\ell+1/2)}_{0,j}h_j\ .\end{aligned}\tag{3.17}$$

Subtracting this result from the LCMFD balance Eq. (3.9) and using the definitions (3.15), we get

$$\tilde{F}^{(\ell+1)}_{1,k+1/2}-\tilde{F}^{(\ell+1)}_{1,k-1/2}+\Sigma_{a,k}\tilde{F}^{(\ell+1)}_{0,k}\Delta_k=\sum_{j\in k}\sigma_{s,j}\left(\tilde{\phi}^{(\ell+1/2)}_{0,j}-\tilde{\phi}^{(\ell)}_{0,j}\right)h_j\ .\tag{3.18}$$

This is the CMDSA balance Eq. (3.6a).

Next, Eqs. (3.11) and (3.15) immediately give

$$\tilde{F}^{(\ell+1)}_{1,k+1/2}=-\frac{2}{3}\left(\frac{\tilde{F}^{(\ell+1)}_{0,k+1/2}-\tilde{F}^{(\ell+1)}_{0,k}}{\Sigma_{t,k+1}\Delta_{k+1}+\Sigma_{t,k}\Delta_k}\right)\ .\tag{3.19}$$

This is the CMDSA Fick's Law, Eq. (3.6b).

Next, Eqs. (3.12) and (3.15) immediately give

$$0=\tilde{F}^{(\ell+1)}_{1,1/2}+\beta\tilde{F}^{(\ell+1)}_{0,1}\ ,\tag{3.20a}$$

$$0=-\tilde{F}^{(\ell+1)}_{1,K+1/2}+\beta\tilde{F}^{(\ell+1)}_{0,K}\ .\tag{3.20b}$$

These are the CMDSA boundary conditions, Eqs. (3.6c) and (3.6d).

Finally, Eqs. (3.14) and (3.15) become

$$\tilde{\phi}^{(\ell+1)}_{0,j}=\tilde{\phi}^{(\ell+1/2)}_{0,j}+\tilde{F}^{(\ell+1)}_{0,k}\ ,\quad j\in k\ ,\quad 1\le k\le K\ .\tag{3.21}$$

This is the CMDSA acceleration Eq. (3.7).

These results show that *the CMDSA and LCMFD methods are algebraically equivalent.*

Remarks: 1. In previous publications, linearizations of nonlinear transport acceleration methods were derived only for homogeneous systems with flat sources and uniform grids [8, 11–14]. In the more general linearization performed in this paper, the physical system

does not need to be homogeneous, the sources do not need to be flat, and the spatial grid does not need to be uniform. Thus, the linearization in this paper establishes a much broader theoretical link between the nonlinear CMFD and the linear CMDSA methods – these methods are essentially equivalent over a larger class of problems. (However, the restriction to a homogeneous system with a uniform spatial grid is necessary for the Fourier analysis presented in Section IV.)

2. The details of the CMDSA discretization method discussed in this paper were chosen to exactly match the linearized CMFD discretization method. However, there are choices in how these discretizations can be done (particularly in the choice of boundary conditions), and these choices determine whether there is exact algebraic equivalence between the LCMFD and CMDSA methods. A main result of this paper is that for any specific choice of a CMFD method, the linearization of this method (in the manner shown in this paper) is algebraically equivalent to a specific CMDSA method.

IV. FOURIER ANALYSIS

To proceed with the Fourier analysis, the equations of CMDSA/LCMFD are simplified by assuming an infinite homogeneous medium with a uniform spatial grid and a specified number p of fine cells per coarse cell:

$$\mu_n \left(\psi_{n,j+1/2}^{(\ell+1/2)} - \psi_{n,j-1/2}^{(\ell+1/2)}\right) + \sigma_t h \psi_{n,j}^{(\ell+1/2)} = \frac{c\sigma_t h}{2}\phi_{0,j}^{(\ell)} + \frac{q_j}{2} \,, \tag{4.1a}$$

$$\psi_{n,j}^{(\ell+1/2)} = \frac{1+\alpha_n}{2}\,\psi_{n,j+1/2}^{(\ell+1/2)} + \frac{1-\alpha_n}{2}\,\psi_{n,j-1/2}^{(\ell+1/2)} \,, \tag{4.1b}$$

$$\begin{aligned} -\frac{1}{3p\sigma_t h}\left(F_{0,k+1}^{(\ell+1)} - 2F_{0,k}^{(\ell+1)} + F_{0,k-1}^{(\ell+1)}\right) + (1-c)\,p\sigma_t h F_{0,k}^{(\ell+1)} \\ = c\sigma_t h \sum_{j\in k}\left(\phi_{0,j}^{(\ell+1/2)} - \phi_{0,j}^{(\ell)}\right) \,, \end{aligned} \tag{4.1c}$$

$$\phi_{0,j}^{(\ell+1)} = \phi_{0,j}^{(\ell+1/2)} + F_{0,k}^{(\ell+1/2)}, \qquad j \in k \,. \tag{4.1d}$$

We choose the following ansatz, which eliminates aliasing between the fine cell and coarse cell modes and results in a system of equations with substantially fewer exponential terms. Let j' denote the (integer) label for any cell in the infinite system; $-\infty < j' < \infty$. Also, let j be a positive integer satisfying $1 \le j \le p$ and let k be an integer such that

$$j' = (k-1)p + j \,.$$

Then for each j', (i) j and k are unique, (ii) k labels the coarse cell within which cell j' resides, and (iii) j labels the position within coarse cell k at which fine cell j' resides. The Fourier ansatz can now be stated as:

$$q_j = 0 \,,$$

$$
\begin{aligned}
\psi_{n,j'-1/2}^{(\ell+1/2)} &= \omega^\ell d_{n,j} e^{i\lambda\sigma_t x_k} \ , \\
\psi_{n,j'}^{(\ell+1/2)} &= \omega^\ell a_{n,j} e^{i\lambda\sigma_t x_k} \ , \\
\phi_{0,j'}^{(\ell)} &= \omega^\ell g_j e^{i\lambda\sigma_t x_k} \ , \\
F_{0,k}^{(\ell+1)} &= \omega^\ell F e^{i\lambda\sigma_t x_k} \ .
\end{aligned}
$$

Inserting this ansatz into Eqs. (4.1), we obtain:

$$
\begin{aligned}
\mu_n \left(d_{n,j+1} - d_{n,j}\right) + \sigma_t h a_{n,j} &= \frac{c\sigma_t h}{2} g_j \qquad 1 \le j \le p-1 \ , \\
\mu_n \left(d_{n,1} e^{i\lambda P \sigma_t h} - d_{n,j}\right) + \sigma_t h a_{n,j} &= \frac{c\sigma_t h}{2} g_j \qquad j = p \ ,
\end{aligned}
\tag{4.2a}
$$

$$
\begin{aligned}
a_{n,j} &= \frac{1+\alpha_n}{2} d_{n,j+1} + \frac{1-\alpha_n}{2} d_{n,j} \qquad 1 \le j \le p-1 \ , \\
a_{n,j} &= \frac{1+\alpha_n}{2} d_{n,1} e^{i\lambda p \sigma_t h} + \frac{1-\alpha_n}{2} d_{n,j} \qquad j = p \ ,
\end{aligned}
\tag{4.2b}
$$

$$
\begin{aligned}
-\frac{F}{3p\sigma_t h}\left(e^{i\lambda p\sigma_t h} - 2 + e^{-i\lambda p\sigma_t h}\right) + (1-c)\, p\sigma_t h F & \\
= c\sigma_t h \sum_{j=1}^{p} \left(\sum_{n=1}^{N} w_n a_{n,j} - g_j \right) \ , &
\end{aligned}
\tag{4.2c}
$$

$$
\omega g_j = \sum_{n=1}^{N} w_n a_{n,j} + F \ . \tag{4.2d}
$$

Eqs. (4.2c) and (4.2d) can be combined, yielding:

$$
\begin{aligned}
a_{n,j} + \frac{\mu_n}{\sigma_t h} d_{n,j+1} - \frac{\mu_n}{\sigma_t h} d_{n,j} - \frac{c}{2} g_j = 0 \ , \qquad 1 \le j \le p-1 \ , \\
a_{n,j} + \left(\frac{\mu_n}{\sigma_t h} e^{i\lambda p\sigma_t h}\right) d_{n,1} - \frac{\mu_n}{\sigma_t h} d_{n,j} - \frac{c}{2} g_j = 0 \ , \qquad j = p \ ,
\end{aligned}
\tag{4.3a}
$$

$$
\begin{aligned}
a_{n,j} - \frac{1+\alpha_n}{2} d_{n,j+1} - \frac{1-\alpha_n}{2} d_{n,j} = 0 \ , \qquad 1 \le j \le p-1 \ , \\
a_{n,j} - \left(\frac{1+\alpha_n}{2} e^{i\lambda p\sigma_t h}\right) d_{n,1} - \frac{1-\alpha_n}{2} d_{n,j} = 0 \ , \qquad j = p \ ,
\end{aligned}
\tag{4.3b}
$$

$$
\sum_{n=1}^{N} w_n \left(a_{n,j} + \hat{F} \sum_{j'=1}^{p} a_{n,j'} \right) - \hat{F} \sum_{j'=1}^{p} g_{j'} - \omega g_j = 0 \ , \tag{4.3c}
$$

$$
\hat{F} = \frac{c\sigma_t h}{\frac{2}{3p\sigma_t h}\left[1 - \cos(\lambda p \sigma_t h)\right] + (1-c)\, p\sigma_t h} \ .
$$

Representing this system of equations (4.3) in block matrix form, we obtain:

$$
\begin{bmatrix} \mathbf{A} & \mathbf{B} \\ \mathbf{C} & \mathbf{D} - \omega \mathbf{I} \end{bmatrix} \begin{bmatrix} \mathbf{f} \\ \mathbf{g} \end{bmatrix} = \begin{bmatrix} \mathbf{0} \\ \mathbf{0} \end{bmatrix} \ . \tag{4.4}
$$

Here the entries of the $2Np \times 2Np$ matrix $\mathbf{A}$ are the coefficients of $a_{n,j}$ and $d_{n,j}$ in Eqs. (4.3a) and (4.3b). The entries of the $2Np \times p$ matrix $\mathbf{B}$ are the coefficients of g_j in Eqs. (4.3a) and (4.3b). The entries of the $p \times 2Np$ matrix $\mathbf{C}$ are the coefficients of $a_{n,j}$ in Eq.

(4.3c). The entries of the $p \times p$ matrix $\mathbf{D}$ are the coefficients of g_j in Eq. (4.3c). The entries of the $2Np$ column vector $\mathbf{f}$ are the terms $a_{n,j}$ and $d_{n,j}$. The entres of the p column vector $\mathbf{g}$ are the terms g_j.

The block matrix can be decomposed as follows:

$$\begin{bmatrix} \mathbf{A} & \mathbf{B} \\ \mathbf{C} & \mathbf{D} - \omega\mathbf{I} \end{bmatrix} = \begin{bmatrix} \mathbf{A} & \mathbf{0} \\ \mathbf{C} & \mathbf{I} \end{bmatrix} \begin{bmatrix} \mathbf{I} & \mathbf{A}^{-1}\mathbf{B} \\ \mathbf{0} & \mathbf{D} - \mathbf{C}\mathbf{A}^{-1}\mathbf{B} - \omega\mathbf{I} \end{bmatrix} . \tag{4.5}$$

The determinant of the original matrix can then be found via:

$$\begin{aligned} \begin{vmatrix} \mathbf{A} & \mathbf{B} \\ \mathbf{C} & \mathbf{D} - \omega I \end{vmatrix} &= \begin{vmatrix} \mathbf{A} & \mathbf{0} \\ \mathbf{C} & \mathbf{I} \end{vmatrix} \begin{vmatrix} \mathbf{I} & \mathbf{A}^{-1}\mathbf{B} \\ \mathbf{0} & \mathbf{D} - \mathbf{C}\mathbf{A}^{-1}\mathbf{B} - \omega\mathbf{I} \end{vmatrix} \\ &= |\mathbf{A}| \left|\mathbf{D} - \mathbf{C}\mathbf{A}^{-1}\mathbf{B} - \omega\mathbf{I}\right| . \end{aligned} \tag{4.6}$$

From Eq. (4.4), we know that $\begin{vmatrix} \mathbf{A} & \mathbf{B} \\ \mathbf{C} & \mathbf{D} - \omega\mathbf{I} \end{vmatrix} = 0$. Also, from inspection of Eqs. (4.3a) and (4.3b), we know that the rows of matrix $\mathbf{A}$ are linearly independent, implying $|\mathbf{A}| \neq 0$. Therefore

$$|\mathbf{D} - \mathbf{C}\mathbf{A}^{-1}\mathbf{B} - \omega\mathbf{I}| = 0 , \tag{4.7}$$

and thus $\omega_j,\ 1 \leq j \leq p$ are the eigenvalues of the $p \times p$ matrix $\mathbf{D} - \mathbf{C}\mathbf{A}^{-1}\mathbf{B}$. We compute these eigenvalues numerically as functions of λ, and then we calculate the spectral radius

$$\rho = \sup_{\lambda} \sup_{1 \leq j \leq p} |\omega_j(\lambda)| . \tag{4.8}$$

V. NUMERICAL RESULTS

The spectral radius is predicted theoretically by the Fourier analysis described above. To confirm that the behavior of CMFD and CMDSA matches this analysis, we estimate the spectral radii of these methods experimentally. The problem used to estimate the spectral radius of the CMDSA method consists of a system with a vacuum boundary on the left side of the slab and a reflecting boundary on the right side with no interior source. The solution of this problem is zero throughout the system, and we initialize the iterative CMDSA method with a step function and observe its convergence to the zero solution. (By choosing a step function as our initial guess, we seed the system with all Fourier modes.) For this problem, the spectral radius can be measured as:

$$\rho = \frac{\left|\left|\phi^{(\ell+1)}\right|\right|}{\left|\left|\phi^{(\ell)}\right|\right|} . \tag{5.1}$$

This problem cannot be used to estimate the spectral radius of CMFD, because the lack of an interior and boundary source causes the low-order problem to produce the exact zero solution in a single iteration. Instead, we choose the same boundary conditions but

with a step function source within the system. The CMFD spectral radius can then be estimated as:

$$\rho = \frac{\left|\left|\phi^{(\ell+1)} - \phi^{(\ell)}\right|\right|}{\left|\left|\phi^{(\ell)} - \phi^{(\ell-1)}\right|\right|} \,. \tag{5.2}$$

The following figures show comparison between the experimental results of these two methods for various coarse cell optical thicknesses, scattering ratios, and numbers of fine cells per coarse cell.

First, Figures 2-5 describe *fine mesh acceleration* (each coarse spatial cell contains $p = 1$ fine spatial cell). In this case, the CMDSA method is the same as the standard fine-mesh DSA method. For small scattering ratios c, the CMDSA and CMFD methods are seen to be stable for all coarse spatial cells and efficient for most coarse spatial cells. However, as c increases, the methods are stable and efficient for coarse cells less than about one mean free path thick, but become unstable for coarse spatial cells greater than about one mean free path thick. The CMDSA and CMFD methods have almost identical spectral radii, and the agreement between theory (Fourier analysis) and experiment (numerical simulation) is seen to be excellent.

Insert Figures 2 through 5 about here.

Next, Figures 6-9 describe *coarse mesh acceleration* in which each coarse spatial cell contains $p = 2$ fine mesh cells. Qualitatively, the results are similar to fine mesh acceleration: the CMDSA and CMFD methods are stable and efficient for coarse spatial cells less than about one mean free path thick, but for scattering ratios near unity, the methods become unstable for coarse spatial cells greater than about one mean free path. The $p = 2$ spectral radii are higher than the $p = 1$ spectral radii, as should be expected because the same coarse mesh calculation is now being asked to accelerate twice as many fine mesh unknowns. As before, the CMDSA and CMFD methods have almost the same spectral radii, and the agreement between theory and experiment is excellent.

Insert Figures 6 through 9 about here.

Figures 10-13 describe coarse mesh acceleration with $p = 3$ fine cells per coarse cell. The results here are qualitatively similar to the $p = 2$ results. The $p = 3$ spectral radii are higher than the $p = 2$ spectral radii, as expected from the reasons noted previously. Also, as in the previous simulations, the agreement between theory and experiment is excellent.

Insert Figures 10 through 13 about here.

Finally, Figures 14-17 describe coarse mesh acceleration with $p = 4$ fine cells per coarse spatial cell. All the trends noted previously are continued in these figures, including the excellent agreement between theory and experiment.

Insert Figures 14 through 17 about here.

In all these figures, the Fourier analysis yields an upper bound to the spectral radius. This is because the experimental neutron systems are finite, and neutron leakage from these systems reduces the theoretical (infinite medium) spectral radius slightly. Also, the spectral radius describes the asymptotic trend of the method after many iterations. Thus, small spectral radii ρ can be difficult to measure experimentally, as the solution converges so rapidly that round-off error can present itself before a good estimate of ρ is achieved. (This issue is most significant with our estimates of the CMFD ρ using Eq. (5.2), which is more sensitive to roundoff errors than Eq. (5.1). In particular, for small ρ the measured CMFD ρ are often slightly lower than the Fourier analysis predictions. The likely reason for this is that the CMFD numerical experiments could not be run to a sufficiently large number of iterations.)

Finally, we note that the numerical results shown above are consistent with the CMFD results obtained previously by Cho and Park [8].

VI. CONCLUSIONS

We have derived – and demonstrated numerically – a close theoretical relationship between the DSA and CMFD methods for accelerating the iterative convergence of particle transport calculations. These two methods were developed independently and have been used for many years in production neutron transport codes.

To the reader who is familiar with the history of DSA and the long (and only partly successful) effort to derive unconditionally stable versions of this method for specified transport discretization schemes, a natural question is: if CMFD is stable only for spatial cells less than about one mean free path thick, then how could this method be used successfully in practical problems? The answer seems to have two parts:

1. In practical multigroup reactor core simulations, CMFD is observed to be somewhat more stable than for one-group problems; the "practical" borderline of instability becomes 2-3 mean free paths [15].
2. In the same simulations, CMFD is commonly used with a coarse spatial cell defined to be a *single pin cell* – which is roughly 1-2 mean free paths across, and hence within

multigroup CMFD's "practical" range of stability. The fine spatial cells (within a coarse cell) are used to resolve the fuel, cladding, and moderator components inside a pin cell. Although CMFD has been successful for reactor physics problems in which a coarse cell is a *single* pin cell, it is not commonly understood that if the coarse grid is enlarged to include *multiple* pin cells, the method can become divergent.

The results in this paper make possible the following prediction: if an inconsistent coarse-mesh version of DSA were implemented to solve the same reactor core problems as CMFD, it would have the same convergence properties as CMFD. Such a code would have advantages and disadvantages compared to a CMFD code. The DSA-based code would be linear, and thus would be insensitive to the appearance of negative angular fluxes in the numerical solution (or in iterates leading to the converged solution); the CMFD method, being nonlinear, could fail if negative angular fluxes ever occur. Conversely, the nonlinearities in CMFD make this method more attractive than CMDSA for the outer iterations in eigenvalue calculations; the additive residual terms in DSA act like an inhomogeneous source, which is not permitted in outer iterations.

Thus, for reactor core k-eigenvalue calculations, the CMDSA method could be used to accelerate the convergence of inner iterations (since these are essentially fixed-source problems with a "known" fission source), while the CMFD method could be used to accelerate the convergence of the outer iterations (since these are not driven by a fixed source). The resulting method would have essentially the same convergence properties as a CMFD code for problems in which CMFD converges. However, because the CMFD/CMDSA method would be insensitive to the occurrence of negative fluxes during inner iterations, it would also be more likely to converge for such problems than a code using CMFD for both outer and inner iterations.

In conclusion, the authors wish to express the hope that the contents of this paper will improve the theoretical understanding of the DSA and CMFD methods for reactor physics problems, and that this will lead to practical improvements in the methods.

ACKNOWLEDGEMENTS

We gratefully acknowledge support of this research through the U.S. Department of Energy NEUP grant DE-AC07-05ID14517.

REFERENCES

[1] M.L. Adams and E.W. Larsen, "Fast Iterative Methods for Discrete-Ordinates Particle Transport Calculations," *Prog. Nucl. Energy,* **40**, 3 (2002).

[2] H.J. Kopp, "Synthetic Method Solution of the Transport Equation," *Nucl. Sci. Eng.,* **17**, 65 (1963).

[3] R. Alcouffe, "Diffusion Synthetic Acceleration Methods for the Diamond-Differenced Discrete-Ordinates Equations," *Nucl. Sci. Eng.,* **64**, 344 (1977).

[4] E.W. Larsen, "Unconditionally Stable Diffusion-Synthetic Acceleration Methods for the Slab Geometry Discrete-Ordinates Equations. Part I: Theory," *Nucl. Sci. Eng.,* **82**, 47 (1982).

[5] D.R. McCoy and E.W. Larsen, "Unconditionally Stable Diffusion-Synthetic Acceleration Methods for the Slab Geometry Discrete-Ordinates Equations. Part II: Numerical Results," *Nucl. Sci. Eng.,* **82**, 64 (1982).

[6] K. Smith, "Nodal Method Storage Reduction by Nonlinear Iteration," *Trans. Am. Nucl. Soc.,* **44**, 265 (1983).

[7] K. Smith, "Assembly Homogenization Techniques for Light Water Reactor Analysis," *Prog. Nucl. Energy,* **17**, 303 (1986).

[8] N.Z. Cho and C.J. Park, "A Comparison of Coarse Mesh Rebalance and Coarse Mesh Finite Difference Accelerations for the Neutron Transport Calculations," *Proc. Conf. Nuclear, Mathematical, and Computational Sciences: a Century in Review, a Century Anew*, Gatlinburg, Tennessee, April 6-11, 2003, American Nuclear Society (2003). [CD-ROM]

[9] Z. Zhong, T.J. Downar, Y. Xu, M.D. DeHart, and K.T. Clarno, "Implementation of Two-Level Coarse-Mesh Finite Difference Acceleration in an Arbitrary Geometry, Two-Dimensional Discrete Ordinates Transport Method," *Nucl. Sci. Eng.,* **158**, 289 (2008).

[10] E.W. Larsen and K.W. Kelley, "CMFD and Coarse-Mesh DSA," *Proc. PHYSOR 2012, Advances in Reactor Physics Linking Research, Industry, and Education*, Knoxville, Tennessee, April 15-20, 2012, on CD-ROM, American Nuclear Society, LaGrange Park, IL (2012).

[11] G.R. Cefus and E.W. Larsen, "Stability Analysis of Coarse Mesh Rebalance," *Nucl. Sci. Eng.,* **105**, 31 (1990).

[12] G.R. Cefus and E.W. Larsen, "Stability Analysis of the Quasidiffusion and Second Moment Methods for Iteratively Solving Discrete-Ordinates Problems," *Transport Theory Statist. Phys.,* **18**, 493 (1990).

[13] Y.R. Park and N.Z. Cho, "Coarse-Mesh Angular Dependent Rebalance Acceleration of the Discrete Ordinates Transport Calculations," *Nucl. Sci. Eng.,* **148**, 355 (2004).

[14] Y.R. Park and N.Z. Cho, "Coarse-Mesh Angular Dependent Rebalance Acceleration of the Method of Characteristics in x-y Geometry," *Nucl. Sci. Eng.,* **158**, 154 (2008).

[15] K. Smith, personal communication.

FIGURE TITLES

Figure 1: Fine and Coarse Spatial Grids

Figure 2: Spectral Radius for $p = 1$ and $c = 0.8$

Figure 3: Spectral Radius for $p = 1$ and $c = 0.9$

Figure 4: Spectral Radius for $p = 1$ and $c = 0.99$

Figure 5: Spectral Radius for $p = 1$ and $c = 0.9999$

Figure 6: Spectral Radius for $p = 2$ and $c = 0.8$

Figure 7: Spectral Radius for $p = 2$ and $c = 0.9$

Figure 8: Spectral Radius for $p = 2$ and $c = 0.99$

Figure 9: Spectral Radius for $p = 2$ and $c = 0.9999$

Figure 10: Spectral Radius for $p = 3$ and $c = 0.8$

Figure 11: Spectral Radius for $p = 3$ and $c = 0.9$

Figure 12: Spectral Radius for $p = 3$ and $c = 0.99$

Figure 13: Spectral Radius for $p = 3$ and $c = 0.9999$

Figure 14: Spectral Radius for $p = 4$ and $c = 0.8$

Figure 15: Spectral Radius for $p = 4$ and $c = 0.9$

Figure 16: Spectral Radius for $p = 4$ and $c = 0.99$

Figure 17: Spectral Radius for $p = 4$ and $c = 0.9999$

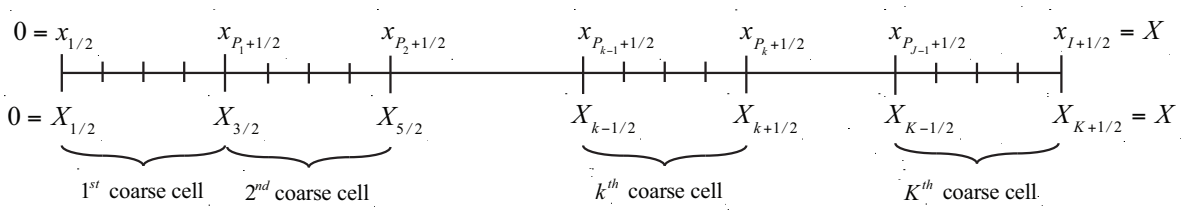

Figure 1: Fine and Coarse Spatial Grids

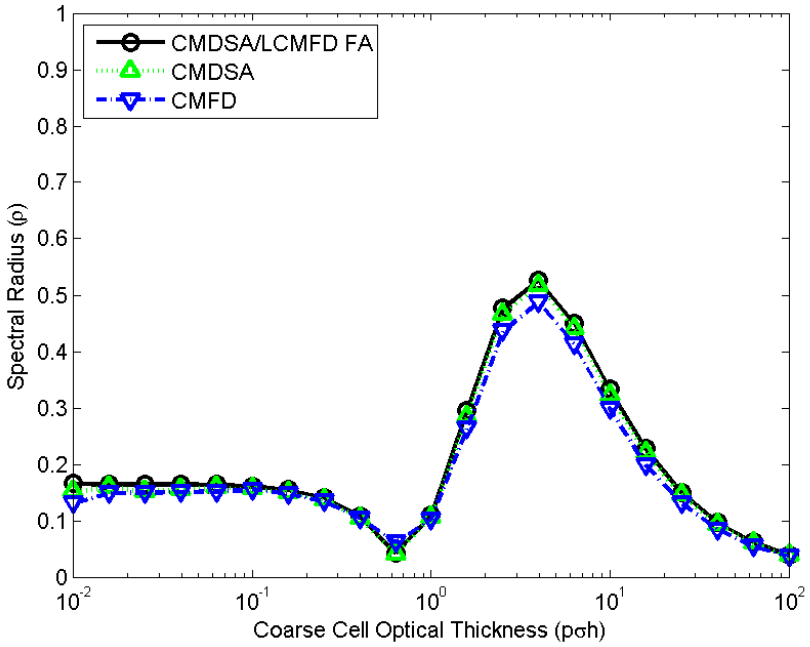

Figure 2: Spectral Radius for $p = 1$ and $c = 0.8$

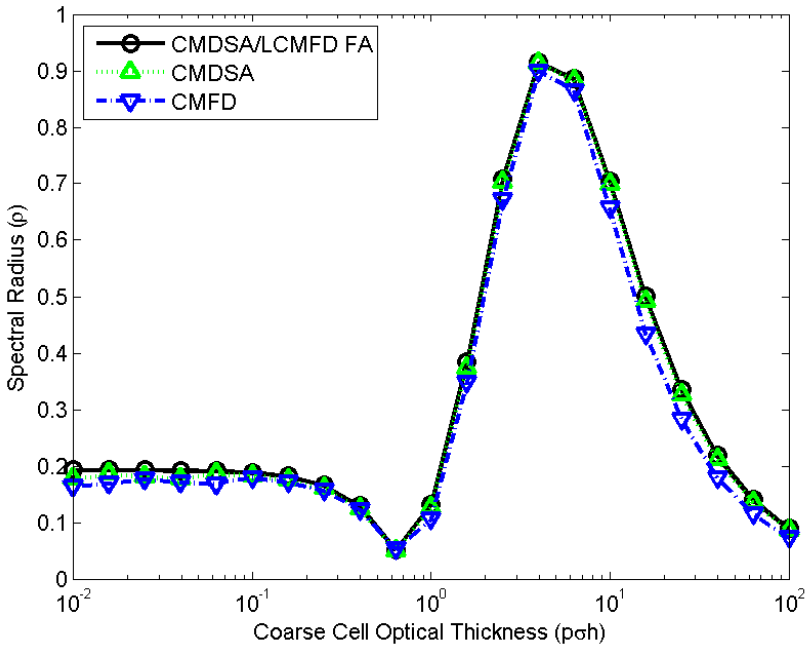

Figure 3: Spectral Radius for $p = 1$ and $c = 0.9$

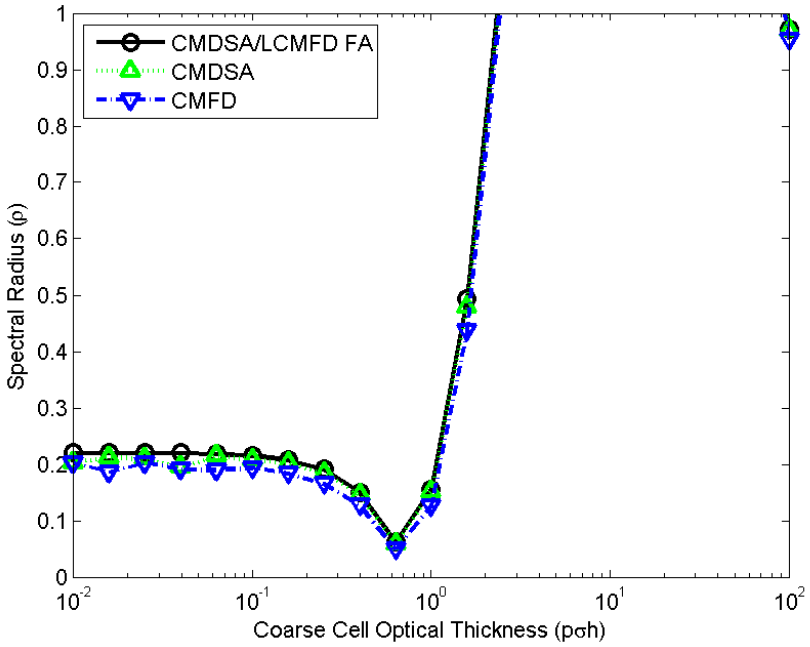

Figure 4: Spectral Radius for $p = 1$ and $c = 0.99$

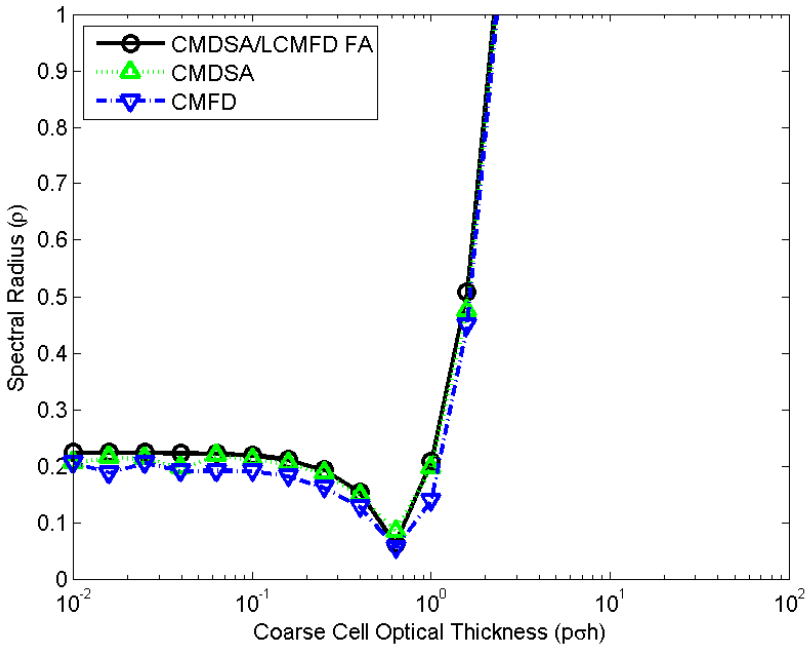

Figure 5: Spectral Radius for $p = 1$ and $c = 0.9999$

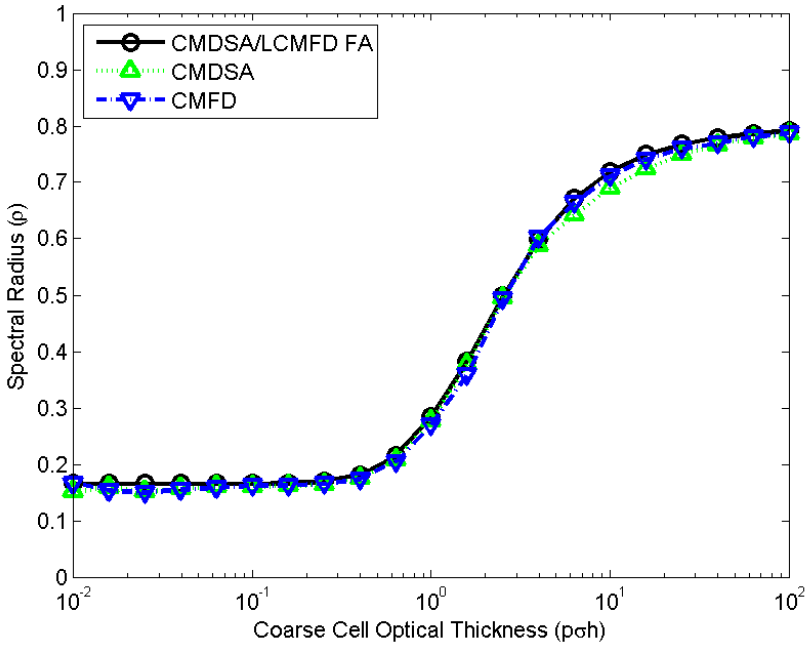

Figure 6: Spectral Radius for $p = 2$ and $c = 0.8$

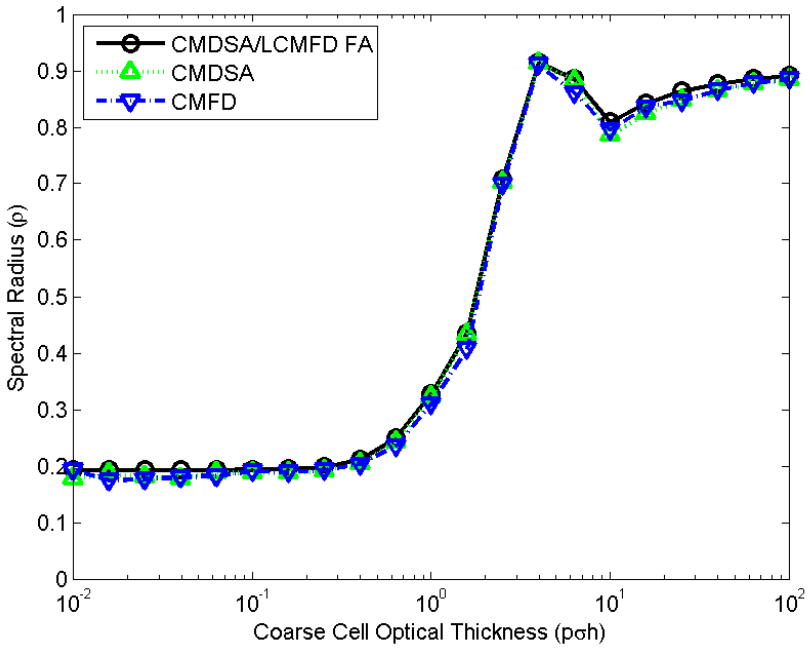

Figure 7: Spectral Radius for $p = 2$ and $c = 0.9$

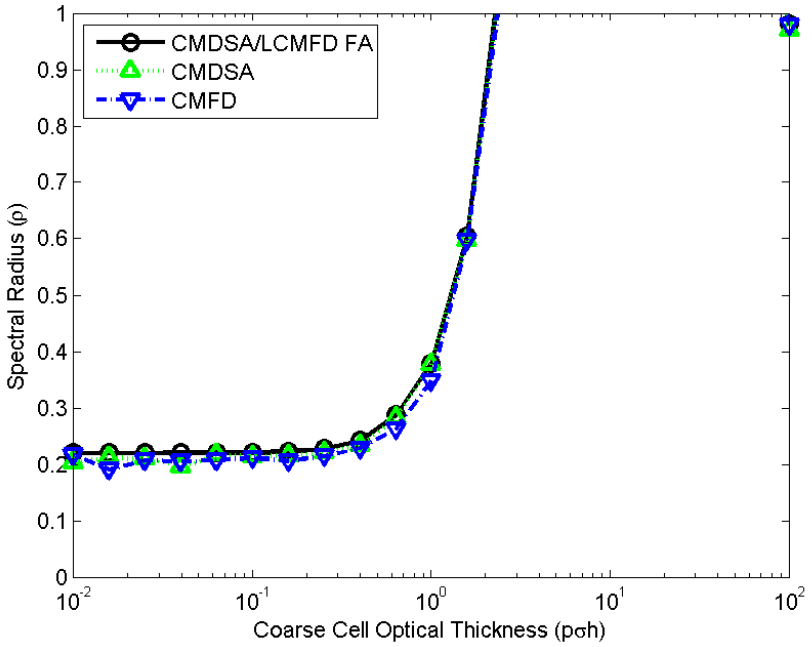

Figure 8: Spectral Radius for $p = 2$ and $c = 0.99$

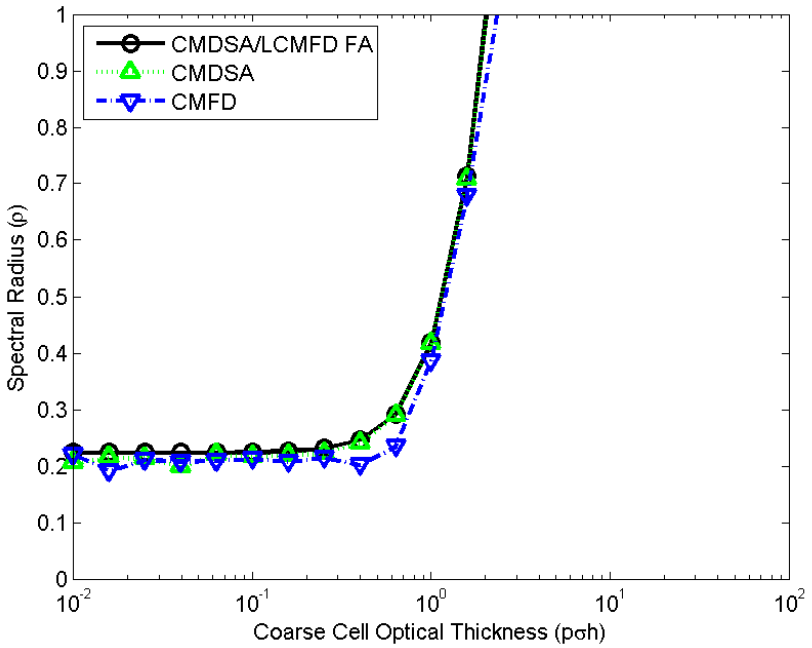

Figure 9: Spectral Radius for $p = 2$ and $c = 0.9999$

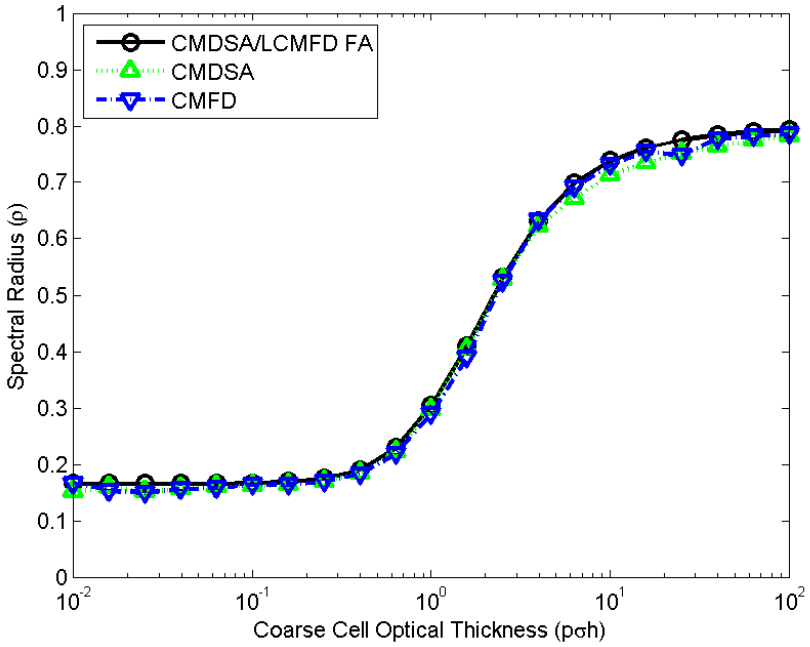

Figure 10: Spectral Radius for $p = 3$ and $c = 0.8$

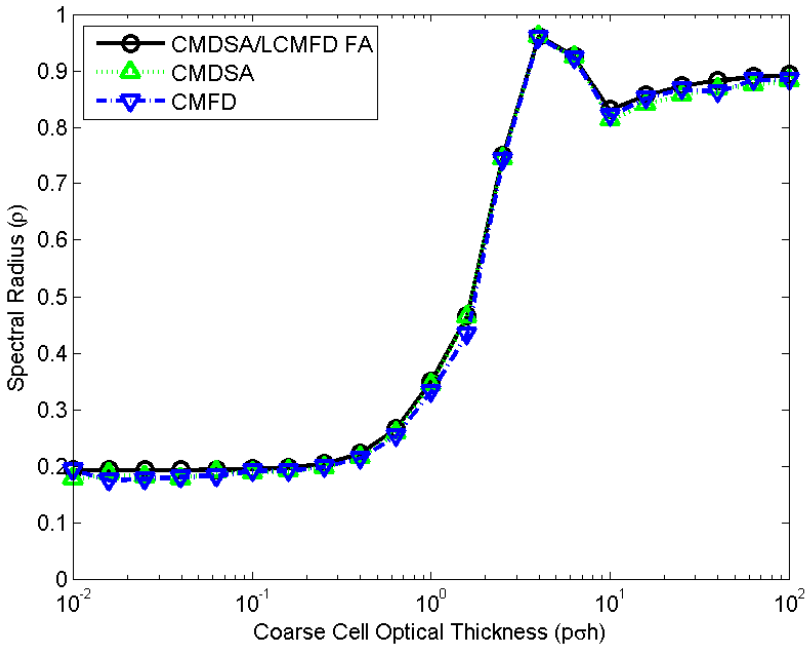

Figure 11: Spectral Radius for $p = 3$ and $c = 0.9$

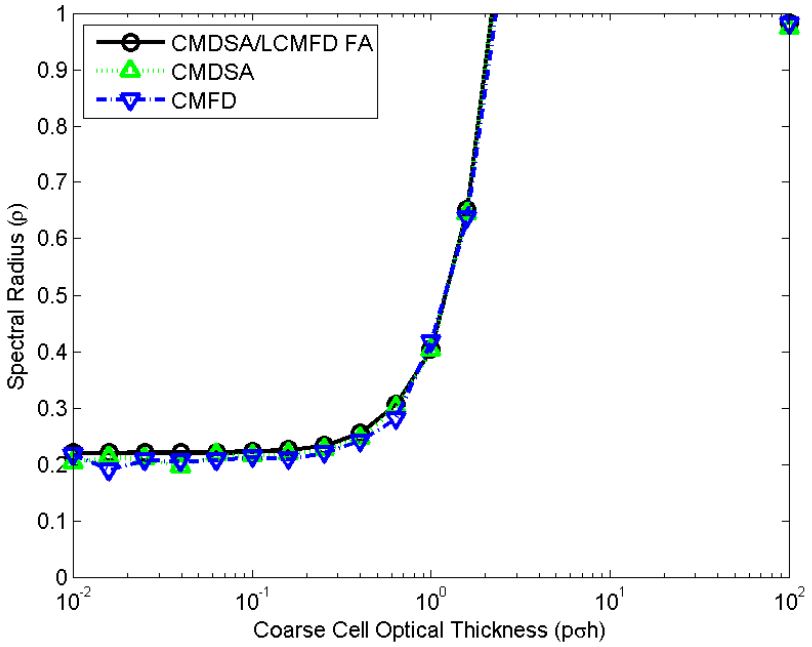

Figure 12: Spectral Radius for $p = 3$ and $c = 0.99$

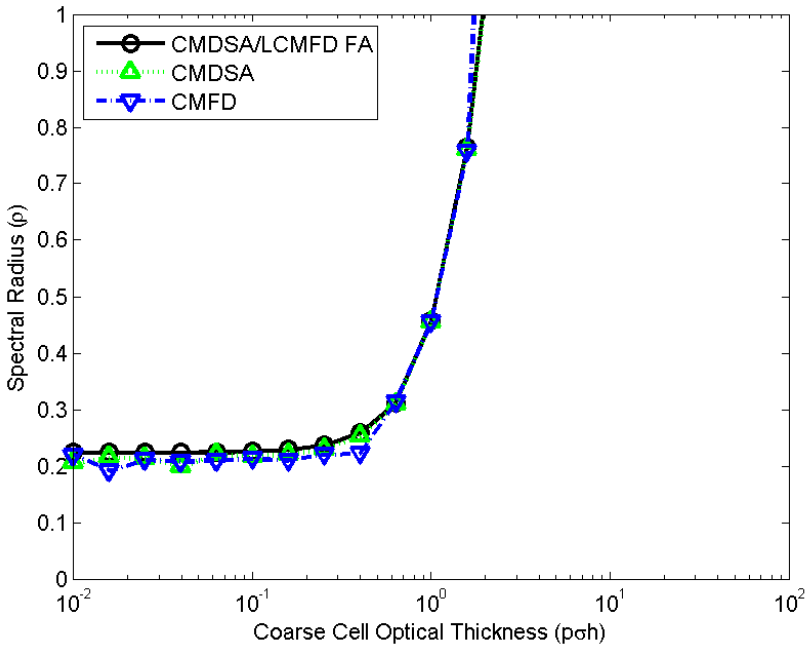

Figure 13: Spectral Radius for $p = 3$ and $c = 0.9999$

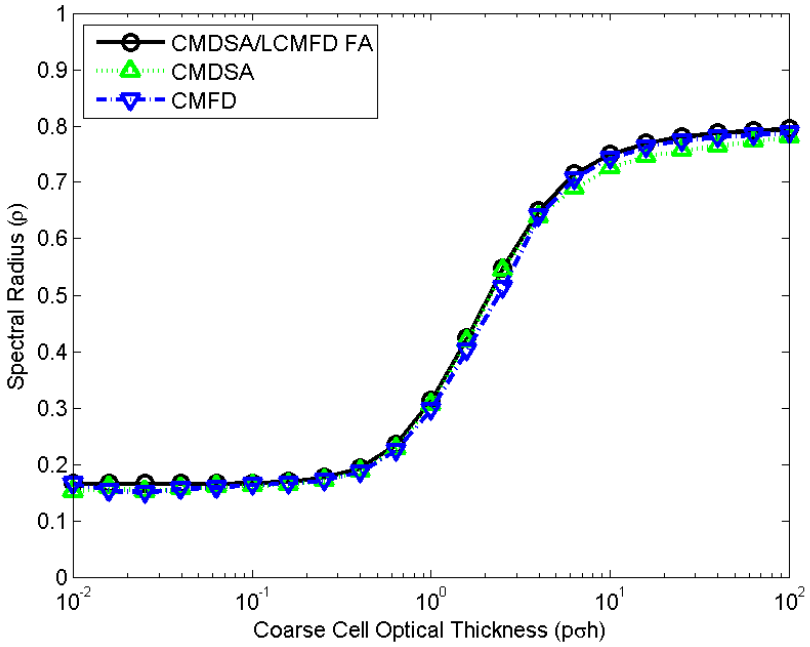

Figure 14: Spectral Radius for $p = 4$ and $c = 0.8$

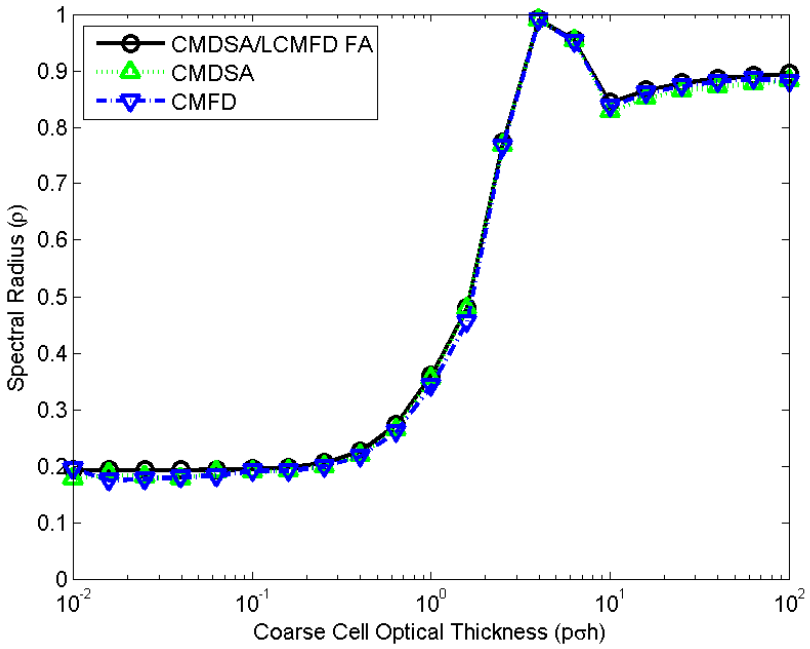

Figure 15: Spectral Radius for $p = 4$ and $c = 0.9$

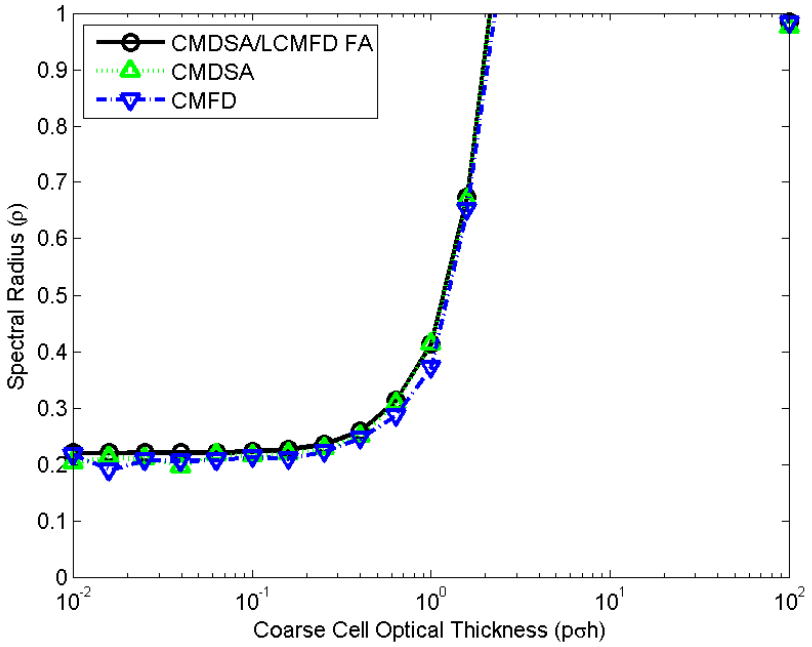

Figure 16: Spectral Radius for $p = 4$ and $c = 0.99$

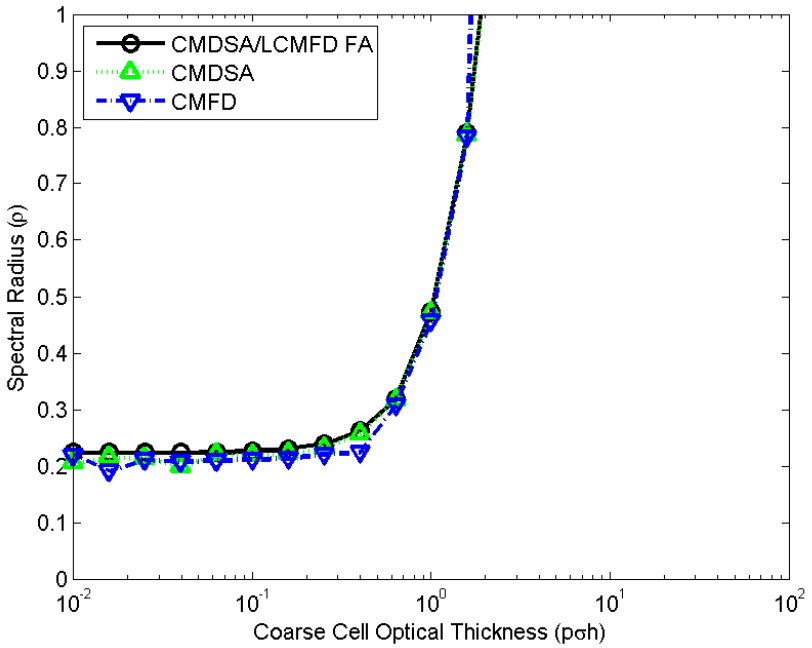

Figure 17: Spectral Radius for $p = 4$ and $c = 0.9999$